Control of Acoustics and Store Separation in a Cavity in Supersonic Flow

by

Debashis Sahoo

B.Tech.(Hons.) in Aerospace Engineering, Indian Institute of Technology, Kharagpur, India (1998)
S.M. in Aeronautics and Astronautics, Massachusetts Institute of Technology (2000)

Submitted to the Department of Aeronautics and Astronautics
in partial fulfillment of the requirements for the degree of

DOCTOR OF PHILOSOPHY

at the

MASSACHUSETTS INSTITUTE OF TECHNOLOGY

February 2005

Author_____
Department of Aeronautics and Astronautics
January 26, 2005

Certified by_____
Dr Anuradha M. Annaswamy
Senior Research Scientist of Mechanical Engineering

Certified by_____
Dr Ahmed F. Ghoniem
Professor of Mechanical Engineering

Certified by_____
Dr James D. Paduano
Principal Research Engineer of Aeronautics and Astronautics

Certified by_____
Dr Karen E. Willcox
Assistant Professor of Aeronautics and Astronautics

Accepted by_____
Dr Jaime Peraire
Professor of Aeronautics and Astronautics
Chairman, Committee on Graduate Students

Control of Acoustics and Store Separation in a Cavity in Supersonic Flow

by

Debashis Sahoo

Submitted to the Department of Aeronautics and Astronautics
on January 26, 2005, in partial fulfillment of the
requirements for the degree of
Doctor of Philosophy

Abstract

The supersonic flight community is currently faced with two cavity-under-cross-flow related problems, one being the high noise levels inside the cavity and the other being the return of a store into the cavity after being released from inside. This thesis provides a systematic framework to understand the dominant physics in both problems and to provide solutions for ameliorating the problems. For the first problem, an innovative cavity acoustics model is developed that rigorously explains the role of leading edge microjets in cavity noise suppression and predicts the magnitude of noise reduction for a given control input (that is the steady pressure at which the microjets are fired). The model is validated through comparison of its noise reduction predictions with experiments done using the Florida State University cavity and wind tunnel for different microjet pressures and under Mach 2.0 and Reynolds number 3 million flow, with the microjets being of diameter 400 microns. Based on the cavity acoustics model, optimization of the control input is performed for microjet-based noise suppression of a general cavity under external cross-flow. The resulting control strategy for the FSU cavity is that of an open loop steady microjet firing with the pressure being uniform along the leading edge. This corresponds to a noise reduction of 9 dB OASPL and 20 dB SPL at the dominant tone. The cavity also exhibits saturation in noise reduction for microjet pressures higher than 30 psig.

The second problem that the thesis is concerned with, is that of unsuccessful store drops from an external bay of an aircraft in flight. A group of researchers under the DARPA-funded HIFEX Program is currently developing an effective control mechanism to ensure safe release of a slender axi-symmetric store from a rectangular cavity under supersonic external cross-flow. The actuator being tested under this program is based on a tandem array of microjet flow injectors distributed in the spanwise direction near the leading edge of the cavity, and the control input is the steady pressure levels at which the microjets are fired. In order to optimize the control input to ensure safe store departure, a low order model that reliably predicts the trend in the store drop trajectory in the presence of microjets becomes necessary. In this thesis, a suitable low-order model is developed with separate components to predict the pitch and plunge motion of the store when it is inside the cavity, when it is passing through the shear layer at the mouth of the cavity and when it is completely outside the cavity. The model is based on slender axi-symmetric body aerodynamics, thin shear layer at the cavity mouth, high Reynolds number external cross-flow, plane shock waves associated with the microjet actuators, no-flow condition inside the cavity and inconsideration of the cavity acoustic field. The model is validated by comparing with the results of store drop experiments performed under the HIFEX Program at Mach 2.0 and 2.46 using a generic sub-scale weapons bay for different control inputs. The

store drop was observed experimentally and predicted by the model to fail when microjets were switched off and successful with microjets on. However, with an increase in microjet pressure, the store drop became unsuccessful. Finally, an optimization of the control input to ensure clean store departure for a host of drop conditions is performed using the low-order model.

Although the underlying time scales of the cavity noise and store release problems are different with the result that the two problems have distinct governing equations and solutions, a notable common thread for both the problems is the microjet-dependent control parameter (that is the microjet-cross-flow momentum flux ratio). Microjets introduce momentum flux into the cavity noise dynamics, that damps out noise inside the cavity. The magnitude of noise reduction is saturated at higher momentum ratio (or higher microjet pressure) because of nonlinear damping effects. The addition of momentum flux also creates a virtual obstruction to the external flow which gets decelerated, compressed and turns away from the cavity, thereby affecting the forces on the store and in turn its separation trajectory. Lower microjet momentum ratio causes the store to drop successfully while higher ratio results in its return towards the cavity because of the nonlinear interaction between the normal force and moment on the store, and store velocity and angle of attack together with the external flow turning angle.

Thesis Committee Member: Dr Anuradha M. Annaswamy
Title: Senior Research Scientist of Mechanical Engineering

Thesis Committee Member: Dr Ahmed F. Ghoniem
Title: Professor of Mechanical Engineering

Thesis Committee Member: Dr James D. Paduano
Title: Principal Research Engineer of Aeronautics and Astronautics

Thesis Committee Member: Dr Karen E. Willcox
Title: Assistant Professor of Aeronautics and Astronautics

Thesis Committee Member: Dr Jaime Peraire
Title: Professor of Aeronautics and Astronautics

Acknowledgments

I would like to express my gratitude to my advisor, Dr Anuradha Annaswamy, for introducing the problem to me and for giving me unstinting guidance, advice and support throughout the execution of the thesis work and especially during the difficult times. Many thanks to my other thesis committee members (Professors Ahmed Ghoniem, Karen Willcox, Jaime Peraire and Jim Paduano) and Prof. Edward Greitzer whose inputs during the critical stages of the thesis work were invaluable. The patience of my thesis committee, particularly while I was traversing the learning curve, is indeed commendable.

A special mention must be made of the folks at the Florida State University Fluid Mechanics Research Laboratory. Among the faculty members are Drs. Farrukh Alvi, Anjaneyulu Krothapalli and Luiz Lourenco. Among the students are Ning Zhuang, Bahadir Alkislar, Brent Greska, Joe Allard, Richard Trotta, Huadong Lou and Charney Davy. Finally among the staff members are Bobby Depriest and Robert Avant. They provided timely help and allowed me to use the necessary laboratory facilities for my experimental work. The warm Florida weather and the enthusiastic support of the Florida State folks also enabled me to undertake non-thesis-related activities which are not possible in the relatively colder Boston area. Because of all this, my trips to Florida State during summers of 2002 and 2003 will always be cherished.

In addition, I am grateful to the following graduate students at the Active Adaptive Control Laboratory and Reactive Gas Dynamics Laboratory of MIT who provided valuable inputs during various stages of the project - Jae Jeen Choi, Sungbae Park, Daehyun Wee and Youssef Marzouk. I must also thank Marie Stuppard, the Academic Program Administrator of Aeronautics and Astronautics for making my graduate life a little smoother despite me facing funding problems on a regular basis during my graduate life.

The unflinching support and encouragement of my family also helped me a great deal to grow as an individual and a researcher during my tenure at MIT.

This work was performed through a subcontract from The Boeing Company under the DARPA program "High-Frequency Excitation Active Flow Control for Supersonic Weapons Release" (Cooperative Agreement F49620-00-2-0384) and their cooperation is highly appreciated.

Contents

List of Figures

List of Tables

Chapter 1

Introduction

This thesis discusses two problems related to a cavity when it is exposed to a supersonic cross-flow. Problem (I) is the high noise levels observed inside the cavity, and problem (II) is the return of a store into the cavity after being released from inside. The thesis provides a systematic framework to understand the dominant physics in (I) and (II), and to provide solutions for ameliorating the problems, based on a microjet-based actuator array near the cavity leading edge. In particular, this document quantifies the extent of disruption of the dominant mechanism behind (I) because of the introduction of microjets, and the influence of the actuator on forces and moments on the store and on its drop trajectory in (II). The thesis also identifies the most relevant microjet-dependent control parameter that characterizes both (I) and (II), and provides a strategy for optimization of the control input to alleviate the two problems. The problem statement, background and the thesis contributions for (I) are outlined in Section 1.1 and for (II) in Section 1.2 in the current chapter. A brief comparison and the connection between (I) and (II) are made in Section 1.3, and the scope of this thesis is enumerated in the concluding section of this chapter.

1.1 Problem (I): Cavity Noise Under Supersonic Flow

The first problem that the thesis deals with is that of high noise levels produced when a cavity, such as the open internal bay of an aircraft, is exposed to an external cross-flow. Noise levels of around 170 dB noise have been observed in a cavity under Mach 2.0 flow [1], as illustrated in Figure 1-1. Such noise levels can potentially be harmful to the structural life of weapon systems inside a weapon bay and to landing gear deployment. The problem

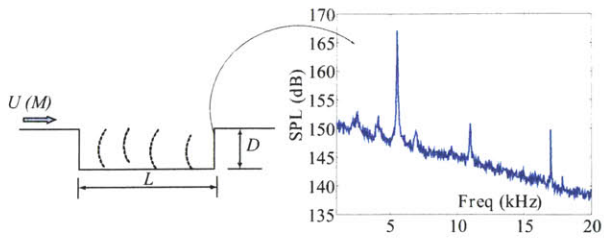

Figure 1-1: High acoustic noise inside a cavity exposed to external cross-flow with $M = 2.0$, Re $= 3$ million (based on cavity length) and $L/D = 5.1$.

statement related to (I) is outlined in Section 1.1.1, its background explained in Section 1.1.2, and the contributions of this thesis towards solving (I) is given in Section 1.1.3.

1.1.1 Problem Statement

A group of researchers under the DARPA-funded HIFEX Program [1, 2, 3, 4] has, through an extensive set of experimental investigations, zeroed in on the leading edge microjets as the most effective actuator for problem (I), that uses the smallest flow rate. This thesis develops a model-based optimal closed-loop control strategy for this problem. This strategy is depicted in Figure 1-2. The pressure sensors on the cavity walls measure noise based on which the control input, which in this case is the steady pressure at which the microjets can be fired at the leading edge, is given.

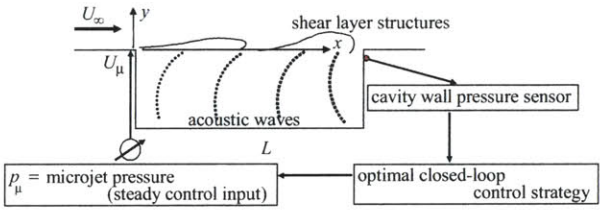

Figure 1-2: Illustration of optimal closed-loop control strategy to be employed in this thesis for cavity noise reduction.

The model to be employed for control should necessarily be reduced-order and parametric (say, in p_μ), thus allowing for closed-loop optimization. The model should also reliably capture the correct trend in the change in OASPL (Overall Sound Pressure Level) of pressure sensors with variation in control input. Along with these features, the model developed in this thesis also identifies the most relevant microjet-dependent control parameter that characterizes the extent of disruption of the dominant mechanism behind problem (I) because of the introduction of the actuator.

From what follows, it is expected that for an uncontrolled cavity and for a cavity with uniform spanwise microjet firing, the flow dynamics inside is two-dimensional, while the flow dynamics due to non-uniform firing is three-dimensional. Hence, the thesis first discusses a two-dimensional model valid for the no-control and uniform firing cases, and then a three-dimensional model valid for non-uniform firing. The three cases are depicted in Figure 1-3. The three-dimensional model is subsequently used for developing the appropriate closed-

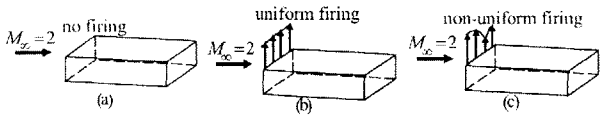

Figure 1-3: Classification of models used for various types of cavity-under-external-cross-flow problems in this thesis.

loop optimal pressure profile. The study is limited to obtaining a steady optimal pressure profile for firing microjets.

To validate the predictions of the model, suitable tests were conducted on a cavity at the Florida State University (FSU) wind-tunnel experimental facility. These tests include flow visualization and noise measurements from pressure sensors on the cavity walls. More details of the facility are available in Zhuang et. al. [1]

1.1.2 Background

Cavity flow under the influence of an external cross-stream can exhibit the following kinds of dynamics – bulk mode (Helmholtz mode), acoustic mode (longitudinal and transverse), Rossiter mode and wake mode [5]. In general, the nature of cavity flow depends on the external flow Mach number and L/D ratio, where L is the cavity length and D is the cavity depth. It also depends on L/W (where W is the cavity width), the level of turbulence and thickness of the boundary layer in the incoming stream. However, it is more useful to look at the cavity flow in the $L/D - M$ plane which contains the dominant factors. Such a scheme is shown in Figure 1-4. As the figure illustrates, low speed ($M <\sim 0.1$) cavities typically exhibit fluid-resonant (acoustic) mode oscillations if they are either very shallow ($L/D >\sim 13$) or deep ($L/D <\sim 0.5$); otherwise they exhibit bulk mode oscillations. Higher speed cavities exhibit Rossiter and wake modes.

Rossiter and wake modes are the most dominant types of dynamics in the typical regions of operation of the internal bay. Rossiter mode [6] has been one of the most extensively

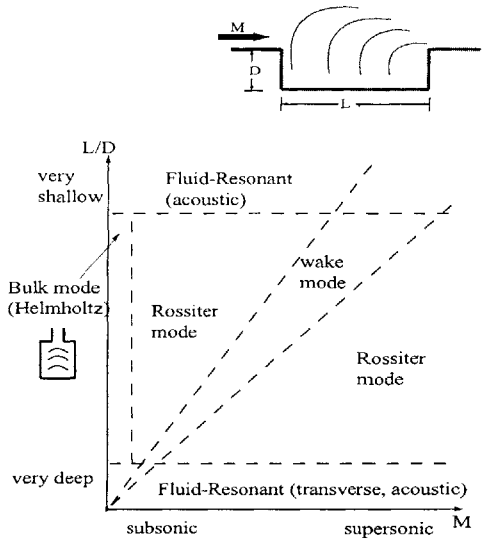

Figure 1-4: Different flow regimes seen by a cavity under external cross-stream.

studied cavity modes for both subsonic and supersonic flows and is a result of an edge-tone phenomenon. It arises when a jet (in this case, the downstream propagating shear layer disturbances) hits an edge and tones are produced. The tones propagate upstream and further excite vortical disturbances at the leading edge, which propagate downstream in the shear layer and complete a feedback loop. Figure 1-5 illustrates the feedback loop characterizing this phenomenon.

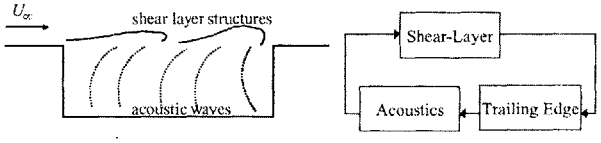

Figure 1-5: Rossiter mode feedback loop and its components.

The frequencies of these cavity tones depend on the cavity geometry and flow conditions and is given by Rossiter's [6] modified formula [7]:

$$f_N = \frac{U}{L} \frac{N - \mu}{\frac{M}{\sqrt{1+\frac{\gamma-1}{2}M^2}} + \frac{1}{k}} \tag{1.1}$$

where f_N is the frequency (Hz) of the Nth mode, $N = 1, 2, \cdots$, μ is a phase constant between the downstream propagating vortical disturbances and the upstream propagating acoustic waves, $1/k$ is a vorticity parameter, γ is the specific heat ratio. μ and k are

typically obtained empirically. The Rossiter's modified formula is obtained by matching of time scales of the shear layer oscillations and acoustic waves, where 'time scales' refers to the frequency and phase of oscillation.

There are currently two interpretations for the driving mechanism for cavity tones under Rossiter mode and are delineated in Figure 1-6. The mechanism, given by Rossiter [6], is the momentary flow separation at the leading edge that results in periodic shedding of localized vortices. A literature survey, however, indicates that vortical shedding has not been observed at all Mach numbers (only between $0.4-1.2$) using current experimental techniques. The alternative mechanism, given by Tam and Block [8], and Bilanin and Covert [9] among others, is the Kelvin-Helmholtz instability of the free shear layer formed at the cavity lip. The flow separation in the first interpretation and Kelvin-Helmholtz instability in the second one are initiated by disturbances in the boundary layer at the upstream end and sustained by excitation due to acoustic waves at the leading edge inside the cavity. We can, however, treat the two explanations as equivalent in the sense that vortical disturbances mentioned in the first interpretation arise due to Kelvin-Helmholtz instabilities.

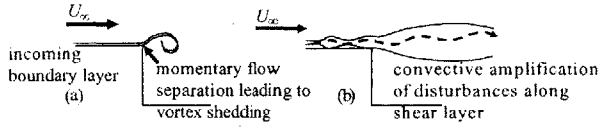

Figure 1-6: Two interpretations of the driving mechanism for cavity tones under external cross-flow.

The noise generation mechanism at the trailing edge can be attributed to the streamwise impingement of shear layer on the trailing edge, as outlined in Figure 1-7. The impingement results in creation of a high-pressure center at the trailing edge. The transient nature of the impingement results in acoustic waves being produced. As explained in Tam and Block [8], these acoustic waves can be accounted for by introducing a periodic line source of monopoles at the trailing edge. The streamwise pressure gradient due to impingement of the shear layer on the trailing edge is: $\nabla_x p' \cong \rho_\infty U_\infty^2$ and thus, the strength of the equivalent monopoles is proportional to $\rho_\infty U_\infty^2$.

In contrast to the Rossiter mode, the wake mode [10] frequency is independent of Mach and Reynolds number. The wake mode is accompanied by coalescence of vortices shed at the leading edge into large scale structures, violent ejection of the vortices at the trailing edge

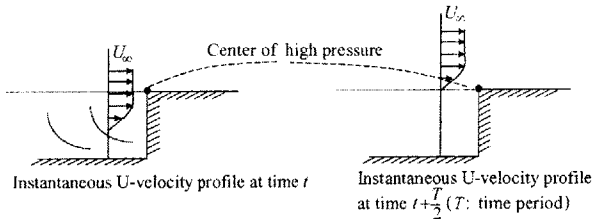

Figure 1-7: Possible mechanism for generation of acoustic waves inside the cavity under external cross-flow.

and flow separation at the leading and trailing edges. It has not been frequently observed in practice and would not be discussed further in this document.

1.1.3 Contributions of Thesis

This thesis uses the framework of Tam and Block [8] and Bilanin and Covert [9] to develop a low order parametric model for the Rossiter tones. An order-of-magnitude analysis performed on the Navier-Stokes equations determines the simplified governing equation for the cavity acoustics, which is the wave equation, similar to Refs. [8, 9]. The solution of this equation is determined by the techniques of Green's function, method of images and proper orthogonal decomposition. The first two solution techniques are similar to Refs. [8, 9] and the last method is a contribution of this thesis. This document also proposes an original technique of incorporating the effect of microjets as an actuator in suppressing the cavity tones. The most relevant microjet-dependent control parameter for the cavity noise reduction problem, identified by this thesis, is the microjet-external-flow momentum flux ratio. The thesis also identifies the underlying mechanism, based on microjet injection, by which noise is suppressed inside the cavity. Using the model, this thesis predicts the magnitude of noise reduction inside the cavity for a given microjet pressure distribution that is validated by experiments performed at the Florida State University wind tunnel [1]. In addition, the thesis develops a strategy for optimizing the microjet-based control input for noise reduction inside the cavity.

1.2 Problem (II): Store Separation From Bay Under Supersonic Flow

In addition to high noise inside a cavity under external cross-flow, the aircraft industry is faced with problem (II), i.e. it has been observed that a store, when released from an internal aircraft bay, can return back under suitable flight conditions. Instances of unsuccessful store drops under subsonic [30] and transonic [31] flows have been found in the literature. In addition, recent experiments under the DARPA-funded HIFEX Program [2, 3, 4] have illustrated the problem under supersonic flow conditions. It should be noted that unsafe store separation is a dangerous problem for an aircraft while it drops weapons from its internal bay. To ameliorate this problem, a group of researchers under the HIFEX Program is currently developing an appropriate control strategy to ensure safe release of a slender axi-symmetric store from a rectangular cavity (bay) with an external supersonic flow. The effectiveness of various flow-disrupting actuators has been studied by the group, and the most promising one is based on an array of microjet flow injectors distributed in the spanwise direction near the leading edge of the cavity. The associated control input is the steady pressure levels at which the microjets are activated. The same actuator has been shown experimentally in [2] and through a low-order model (Chapters 2-3 of this thesis) to be effective in quietening the shear layer at the cavity opening and reduction of the cavity tones. In addition, this actuator introduces shocks which in turn induce additional corrective forces and moments on the store when it is external to the bay, thereby enabling control of its trajectory for ensuring safe separation. As in section 1.1, we discuss in sections 1.2.1, 1.2.2, and 1.2.3, the problem statement for (II), its background, and the contributions of this thesis in solving (II), respectively.

1.2.1 Problem Statement

The development of an effectual control strategy for safe store separation from a cavity under cross-flow necessitates a low order model that accurately predicts the trend in the store trajectory, i.e. whether the store is ejected from the cavity safely or returns back into the cavity, under given initial drop conditions and a given control input. This trend is potentially influenced by a host of factors (Figure 1-8), including the inhomogeneous flow field generated by the wavy shear layer structures at the cavity opening, the potential

induced by the store motion, the shock waves introduced by the microjets and at the store nose, and noise inside the cavity, all of which should be incorporated in the model. What is examined in this thesis is an investigation of the forces and moments on the store due to these factors, a low-order model that captures the dominant mechanisms, and an optimization scheme for the control input to ensure safe store separation.

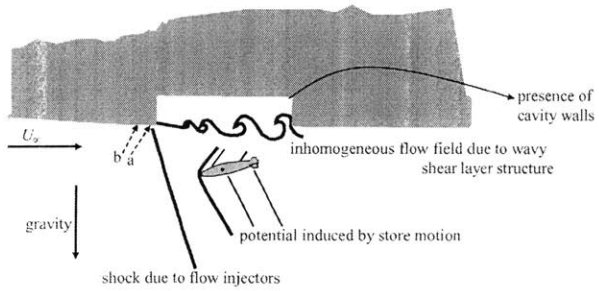

Figure 1-8: Different factors affecting the store release trajectory under supersonic cross-flow and in the presence of microjet-based actuators. Labels 'a' and 'b' indicate different rows of microjets located near the cavity leading edge.

1.2.2 Background

The dynamics of a slender body separating from a rectangular cavity under a cross-flow is difficult to analyze, expensive to experiment upon and is mostly used for military applications. As such, limited models are available in literature and the pertinent ones are outlined here. The problem of store release from a cavity under subsonic flow has been extensively analyzed by Shalaev, et. al. in Ref. [30]. In this paper, a low-order model of the store dynamics is derived, based on slender body potential flow theory, and results in a set of ordinary differential equations for the store motion which is analytically solvable under suitable conditions. This model is shown to predict the store trajectories observed in subsonic wind tunnel experiments. However, in the paper, neither a detailed discussion of the underlying mechanisms nor a qualitative analysis of the conditions for unsafe departure is carried out. In Ref. [31], the store separation from a cavity under transonic flow has been studied by the same authors. A similar model as in [30] is developed here too, but results in a set of nonlinear differential equations for the store trajectory that cannot be solved analytically. This model is then used to show conditions under which unsafe store departure occurs. However, no experimental confirmation is carried out. Also as in [30], the mechanism for unsuccessful store drop is not investigated in detail. Finally in [33], the same

problem is considered in supersonic flow, with the treatment being similar to [31]. Ref. [33] predicts the conditions for unsafe store ejection and also discusses the store interaction with shock waves due to the parent body from which the store is separated. However, as before, no detailed insight into the mechanism for failure in store drop is found and no experimental validation is carried out.

An alternative approach for external store separation found in the literature [34] is based on grid testing. In this method, the store aerodynamic load at any position in the grid is assumed to be a function of only its free stream aerodynamics and the parent aircraft induced aerodynamics at that flow field position. The free stream aerodynamics is a property of the store alone while the aircraft induced aerodynamics is determined by the aircraft flow field, with the mutual interference between the aircraft and the store being considered a secondary effect. The aerodynamic loads are then fed into a six degrees-of-freedom (6 DOF) program based on Newton's laws to compute the external store release trajectory from an aircraft. An improvement over this approach is tried in a store separation problem for the SH-2G helicopter [35] in which a linear interference effect between the store and the helicopter is incorporated in the 6 DOF program. To reduce the cost of testing, a judicious combination of wind tunnel testing and CFD analysis is used. This method is validated by comparing with experimentally available store release trajectory data. However, the limitations of this approach are lack of available free stream data for all store shapes for all possible pitch angles, lack of physical insight into the problem and expensive experiments required.

1.2.3 Contributions of Thesis

The model followed in this thesis is based on the store separation work carried out for supersonic flows in Ref. [33]. By using a careful investigation of the force and moment expressions on the store obtained from the reference, we obtain a set of parametric nonlinear ordinary differential equations that enables us to identify the mechanism and, therefore, the criteria for unsafe store release from a cavity. We believe that the mechanism governing the trajectory of a store released from a cavity onto a supersonic cross-flow has not been identified before, and is therefore an important contribution of the thesis. A more important contribution is the extension of the model to include the effect of microjets on the store trajectory. The model identifies the most relevant microjet-dependent control parameter

(that is the microjet-cross-flow momentum flux ratio) and the underlying process by which the store trajectory is influenced, thereby predicting the microjet pressures for realizing a successful store departure. The model is also used to determine the optimal microjet pressure distribution for a clean weapon release and this control strategy is shown to agree with experimental observations made by the HIFEX group [2, 3, 4] for different supersonic Mach numbers. Finally, the model suggests better choices for the actuator parameters at some of the operating conditions.

1.3 Comparison of Cavity Noise and Store Release Problems

As the above discussions indicate, this thesis contains two distinct contributions which were presented in sections 1.1 and 1.2. Here, a brief comparison and connection between the two contributions are made. The underlying time scales of the cavity noise and store release problems are different, with the dominant frequencies being in the MHz and KHz ranges respectively. As such, the governing equations and solution tools for both problems are different. The cavity acoustics problem is governed by the damped wave equation, while the store release trajectory is governed by the Laplace Equation in the store cross-section plane. The wave equation is solved using the techniques of Green's function, method of images and proper orthogonal decomposition; the Laplace Equation by multipole expansion and conformal transformation. Further, the wave equation gives the pressure perturbation inside the cavity, which is then summed over all frequencies to give the overall sound pressure level. On the other hand, the Laplace Equation gives the velocity potential of the store which is converted to pressure using the Bernoulli's equation and then integrated over the store surface to give the normal force and moment on the store which in turn determine the store release trajectory.

A notable common thread for both the problems is the microjet-based actuation system. Microjets introduce momentum flux into the cavity noise dynamics, that manifests itself as an active damper which suppresses noise inside the cavity. The magnitude of noise reduction is saturated at higher momentum ratio because of nonlinear damping effects. Interestingly enough, the same momentum flux introduction also creates a virtual obstruction to the external flow because of which leading edge shock waves are created along with external flow deceleration, compression, and flow turning. These effects affect the normal force and

pitching moment on the store and therefore influence whether the store drops safely from the cavity or not. Both the extent of noise damping and the strength of the shock waves are determined by the shape of the micro-shock structure at the exit of the microjet nozzle. These dependencies are accurately quantified in the current document, and the strategies to optimize the control input for both the noise reduction and safe store separation problems are derived.

1.4 Scope of Thesis

This thesis outlines the development of a reduced order model for optimal control of noise inside a cavity under supersonic cross-flow, and a low order model for optimization of the control input of the drop trajectory of a store released inside a bay under supersonic flow. The actuator used in both problems is microjet-based fluid injection system placed at the cavity leading edge, with the injection being transverse to the external flow direction.

Chapter 2 discusses the development of a reduced-order model to describe the tones in the absence and presence of microjets at the leading edge. Further, two microjets-on cases are tackled: (i) microjets are fired with uniform pressure along the leading edge (referred to as uniform control), and (ii) microjets are fired with pressure that varies in a pre-defined manner along the leading edge (referred to as non-uniform control). This chapter also describes the experimental arrangement used in Florida State University (FSU) for demonstrating microjet-based cavity noise reduction phenomenon.

Chapter 3 uses the three-dimensional acoustics model developed in Chapter 2 to optimize the control input for noise suppression inside a cavity under supersonic cross-flow, using microjets at the leading edge. This study is limited to the control input being a steady spanwise microjet pressure distribution. The strategy is also derived based on the proper orthogonal decomposition technique and implemented using the FSU experimental setup.

Chapter 4 deals with the second problem that the thesis is concerned with: the problem of safe store separation from a cavity under supersonic cross-flow using microjet-based actuator. This chapter outlines the development of an appropriate low order model that predicts the correct trend in the store drop trajectory. It also analyzes the low-order in terms of the store drop behavior for two cases: (I) when microjets are off, and (II) when the microjets are switched on. It then compares the low order model predictions with results

from experiments performed by the HIFEX group. Finally, it describes an optimization process to find the best control input (in terms of microjet-free-stream momentum ratio) that would ensure a successful store drop from a cavity under supersonic cross-flow.

Chapter 5 summarizes the work done and conclusions made therein. It also gives an outline for the extensions that can be made to the reduced-order models related to cavity acoustics and store release trajectory under supersonic cross-flows and their limitations.

Chapter 2

The Cavity Acoustics Problem

In this chapter, we derive a reduced-order model to describe the tones in a cavity under supersonic cross-flow. Section 2.1 describes the microjets-off case and outlines the assumptions involved in developing the reduced-order governing equations and the derivation of the same from the Navier-Stokes equations. Section 2.2 explains the process of suppression of tones inside a cavity under supersonic cross-flow using microjets at the leading edge. It also describes the experimental arrangement used in Florida State University (FSU) for demonstrating microjet-based cavity noise reduction phenomenon. Finally, section 2.3 outlines the derivation of the governing equations for the cavity acoustics problem with microjets-on.

2.1 Cavity Tones in the Absence of Microjets

This section discusses the development of a reduced-order model to describe the tones in a cavity under supersonic cross-flow in the absence of microjets.

2.1.1 Cavity Acoustics Model

The motivation behind the proposed reduced-order model (to be used for cavity tones control) lies in two independent pioneering works by Tam and Block [8], and Bilanin and Covert [9]. During the decade of 1970, these authors developed models predicting the frequencies of the tones in a two-dimensional rectangular cavity under external flow. The acoustic presence of the trailing edge and cavity walls was modelled by a periodic line source at the trailing edge and suitably placed images of the line sources respectively. The model agreed well with experimental results for speeds ranging from low subsonic to low supersonic

flows ($M = 0.4-1.2$). These studies are used as a starting point for constructing the desired reduced-order model.

Since the cavity tones are essentially a two-dimensional phenomenon, we consider a two-dimensional reduced-order model for the same. The model domain is restricted to the internal cavity volume bounded by the cavity walls and the shear layer which is at the cavity lip, as illustrated in Figure 2-1.

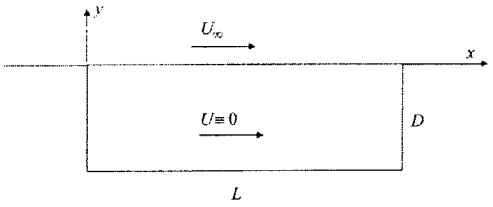

Figure 2-1: Configuration of supersonic cavity flow used in the model.

Based on shadowgraph and PIV visualization studies [1], the following assumptions are made with regards to the internal cavity flow field:

(1) The shear layer separates the cavity flow field from the external supersonic stream. The supersonic flow does not expand into the cavity and there is no Prandtl-Meyer expansion fan inside the cavity.

(2) The mean convective flow inside the cavity is ignored. In practice, a reverse flow with speeds up to 40% of the external flow stream has been observed. This is neglected in the first-order proposed model.

(3) The mean static pressure is assumed to be uniform inside the cavity. In practice, the mean static pressure varies by about 15% along the streamwise direction.

(4) Static temperature and mean density is assumed to be uniform all over the cavity.

(5) Effects of gravity and viscosity are ignored.

These assumptions are outlined in Figure 2-2. Based on the assumptions, the flow inside the cavity can be considered as isentropic. Then we can apply the isentropic flow, mass and momentum conservation equations respectively to the inner cavity volume as follows:

$$p' = \bar{c}^2 \rho' \tag{2.1}$$

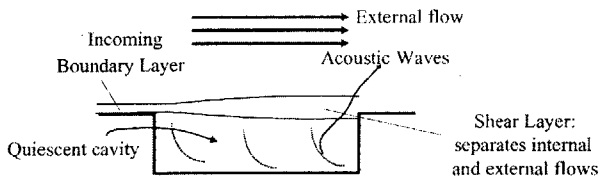

Figure 2-2: Illustration of the assumptions behind the reduced-order cavity acoustics model.

$$\frac{\partial \rho}{\partial t} + \nabla \cdot \rho \vec{u} = 0 \tag{2.2}$$

$$\rho \frac{D\vec{u}}{\partial t} = -\nabla p \tag{2.3}$$

Here '$\cdot'$' indicates (zero-mean) perturbation quantities and '$\bar{\cdot}$' indicates the mean component.

We use Eqns. (2.1)-(2.3) to obtain the governing equation as follows:

$$\underbrace{\frac{\partial^2 p'}{\partial^2 t}}_{\text{Inertia}} - \underbrace{\bar{c}^2 \nabla^2 p'}_{\text{Stiffness1}} = \underbrace{-\nabla \cdot \left(\frac{\partial p'}{\partial t} \vec{u}' \right)}_{\text{Damping}} + \underbrace{(\nabla p') \cdot (\vec{u}' \cdot \nabla \vec{u}') + p' \nabla \cdot (\vec{u}' \cdot \nabla \vec{u}')}_{\text{Stiffness2}} + \underbrace{\bar{c}^2 \bar{\rho} \nabla \cdot (\vec{u}' \cdot \nabla \vec{u}')}_{\text{Inhomogeneous}} \tag{2.4}$$

We then use an order-of-magnitude analysis to identify the dominant groups (details given in Appendix A). The governing equation obtained on keeping the dominant terms is given by:

$$\frac{\partial^2 p'}{\partial^2 t} - \bar{c}^2 \nabla^2 p' = 0 \tag{2.5}$$

with the equation valid for $0 < \frac{u'}{U_\infty}\Big|_a < 0.2$, $0 < \frac{v'}{U_\infty}\Big|_a < 0.1$, $4 < \frac{L}{D} < 6$ and $0.3 < M_\infty < 5$. Here, the subscript 'a' refers to the amplitude of the quantity.

Eqn. (2.5) can be solved using Green's function technique and method of images, similar to Tam [8] and Covert's [9] work. Green's function method is used to derive the pressure field in an infinitely long two-dimensional quiescent medium while the method of images is used to account for reflection of waves at the cavity walls, as illustrated in Figure 2-3.

The governing equation for obtaining the Green's function is as follows:

$$\frac{d^2 P}{dt^2} + \omega^2 P = 0 \tag{2.6}$$

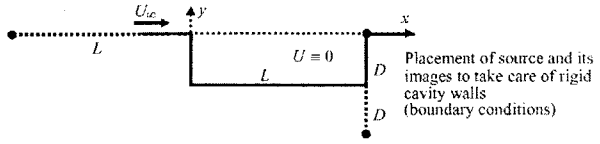

Figure 2-3: Illustration of the method of images for solving the pressure perturbation field inside the cavity under external cross-flow.

This equation is same as (B.3) in Appendix B where the solution procedure is detailed. Then the solution inside the uncontrolled cavity based on Green's function and method of images is given by:

$$p'(x,y,t;\omega) \approx \frac{Q}{2\pi}\left[H_0^{(1)}\left(\frac{\omega}{\bar{c}}\sqrt{(L-x)^2+y^2}\right)+H_0^{(1)}\left(\frac{\omega}{\bar{c}}\sqrt{(L+x)^2+y^2}\right)+ H_0^{(1)}\left(\frac{\omega}{\bar{c}}\sqrt{(L-x)^2+(y+2D)^2}\right)\right]\exp(i\omega t)+(\cdot)^* \qquad (2.7)$$

Here ω is the frequency of a cavity tone in radians per second and is given from Eqn. (1.1). It may be noted that $N = 4$ corresponds to the most dominant tone in the FSU cavity and our region of interest is between $N = 1$ to 8 that corresponds to frequencies less than 12000 Hz. This limitation arises from the sampling frequency of the instrumentation used in the cavity experiments. Also $H_0^{(1)}(\cdot)$ is the first order first kind Hankel function [11].

The other unknown in Eqn. (2.7) is Q which is the strength of the source introduced in the problem and can be determined by matching the experimentally obtained spectrum with the spectrum predicted from this model. The latter is obtained by summing the pressure given by Eqn. (2.7) over all major Rossiter frequencies from $N = 1$ to 8 as follows:

$$p'(x,y,t) \approx \sum_{N=1}^{8} p'(x,y,t;\omega_N) \qquad (2.8)$$

The matching between the model and experimental spectra is done so as to equalize the SPLs (Sound Pressure Levels) at the different tones and is illustrated in Figure 2-4. Apart from the peak matching, it is clear from the figure that there is a discrepancy in frequencies of about 10% between the values predicted by Eqn. (1.1) and the experimentally obtained ones. The reason is that the values of μ and k used in Eqn. (1.1) (that are, respectively, 0 and 0.6 for the FSU cavity) are commonly accepted values used in literature. It was further observed that in order to match the frequencies exactly, the values of μ and k need to be changed for each tone. So no attempt was subsequently made to refine the frequencies used

in the model and the 10% difference was considered to be acceptable.

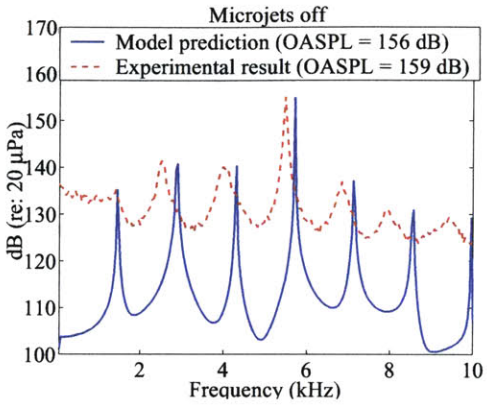

Figure 2-4: Matching of experimental and model-predicted SPLs at the cavity leading edge. The experiment was conducted with external flow having $M = 2.0$, Re = 3 million (based on cavity length) and cavity having $L/D = 5.1$. Uncertainty in experimental SPL was $\pm 0.5dB$ and uncertainty in frequency $\pm 40Hz$ which is 0.8% of the dominant tone.

Now we consider the effect of assumptions (2) and (3) on the pressure field inside the cavity. The governing equation in the presence of a uniform reverse flow U_r due to pressure gradient inside the cavity is:

$$\left(\frac{\partial}{\partial t} - U_r \frac{\partial}{\partial x}\right)^2 p' - \bar{c}_r^2 \nabla^2 p' = 0 \tag{2.9}$$

We have:

$$O\left(\frac{\frac{\partial}{\partial t}}{U_r \frac{\partial}{\partial x}}\right) = \frac{\omega}{U_r L} = \frac{2\pi(N-\mu)}{\frac{M_\infty}{\sqrt{1+\frac{\gamma-1}{2}M_\infty^2}} + \frac{1}{k}} \frac{U_\infty}{U_r} \tag{2.10}$$

This ratio is 3.2 at the dominant frequency, and so the inverse term $U_r \frac{\partial}{\partial x}$ is not negligible. The presence of the term $U_r \frac{\partial}{\partial x}$ would change the Hankel function in Eqn. (2.7) but the change can potentially be absorbed by the acoustic source strength Q. In this first order model, the reverse flow effect is ignored and the pressure field given by Eqns. (2.7) and (2.8) is considered to describe the uncontrolled cavity.

2.2 Effect of Microjets on Cavity Tones

In this section, we explain the process of suppression of tones inside a cavity under supersonic cross-flow using microjets at the leading edge.

2.2.1 Noise Suppression Using Microjets

There are several ways of suppressing the cavity tones. One option is to disrupt the feedback loop that causes the tones, thereby reducing the acoustic noise level. This can be realized by passive and active devices located at the leading or trailing edge (depicted in Figure 2-5). Several noise control devices in literature have also been observed at the upstream end or inside the cavity, all fulfilling the objective of breaking the feedback loop. Spoilers, ramps and vortex rods are examples of the passive devices [5] that have been used for noise suppression while active devices include piezoelectric flaps [12], pulsed air injectors [13], powered resonance tubes [14], jet screens (currently being tested at Boeing) and microjets [1]. In general, passive devices tend to exhibit undesirable performance at off-design con-

Figure 2-5: Various passive devices used for cavity tone suppression in literature and device location relative to the cavity.

ditions. As for the active devices, all the air injection systems, except for microjets, need a significant mass flow (1-10% or higher) to be effective. In contrast, microjets require less than 1% [1]. The reference mass flow here is the amount of free flow through an area equal to the cavity side wall. Microjets have the additional advantage of high momentum flux when compared to other air injection systems. Piezoelectric devices have been shown to work at low subsonic flows but their effectiveness in high speed flows remains to be seen. A detailed review of noise suppression techniques is given in Cattafesta, et. al. [15]

The arrangement for realizing microjet-based control for noise reduction in the FSU cavity is shown in Figure 2-6. In this configuration, there are three microjet banks connected to a pressure-regulated nitrogen supply chamber. Each bank feeds four microjets; the three banks thus take care of the entire set of 12 microjets (of diameter 400 μm each). The pressure regulation of microjets is done manually and hence only steady-input control can be implemented.

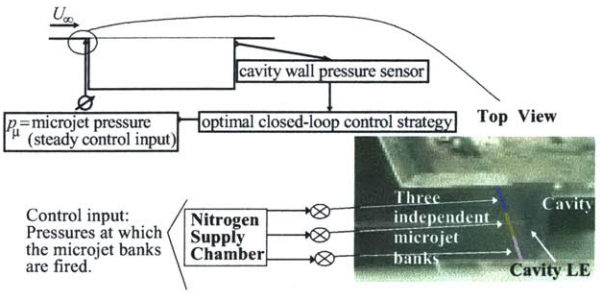

Figure 2-6: Experimental arrangement for realizing control in the FSU cavity. The control input is given in terms of the three microjet pressure banks, from bottom to top.

2.2.2 Observations After Using Microjets

The following changes were observed from flow visualization and noise measurement studies in the FSU cavity after introduction of microjets:

- Damped pressure perturbation field inside the cavity.
- Decrease in frequency of the dominant cavity tone and similar behavior in the other tones.
- Weak shock observed at the cavity leading edge.
- Deceleration and turning of external flow behind the shock.

A simple explanation for the decrease in frequency of the dominant cavity tone is as follows. Because of decelerated flow behind the shock, the modified Rossiter frequency expression becomes:

$$f'_N = \frac{U_{2x}}{L} \frac{N - \mu}{\frac{M_{2x}}{\sqrt{1+\frac{\gamma-1}{2}M_{2x}^2}} + \frac{1}{k}} \tag{2.11}$$

where the notations follow from Figure 2-7. Since U_{2x} in the numerator has the dominant effect on the frequency, it is clear that the latter would decrease with decrease in flow velocity, in other words, with increase in microjet pressure input. This is because the shock strength increases with microjet pressure input and flow speed behind the shock decreases with increase in shock strength. The dominant frequency for different microjet pressures is shown in Table 2.1 (taken from Zhuang, et. al. [1]) and illustrates this phenomenon.

The free stream speed, used for computing the dominant frequency from Eqn. (2.11) in Table 2.1, was derived from oblique plane shock relationship. The reason for using plane

Table 2.1: Dominant cavity frequency predicted by model and obtained from experiments done on FSU cavity (under $M = 2.0$ and Re = 3 million flow). Re is based on cavity length.

p_μ, psig	No control	30	100	200
Experiment (KHz)	5.55	5.35	5.31	5.16
Model (KHz)	5.66	5.36	5.33	5.12

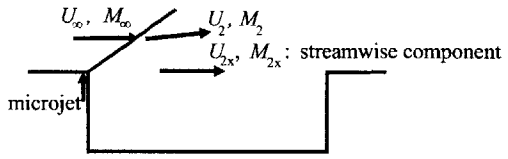

Figure 2-7: Effect of leading edge shock on the external cross-flow over the cavity.

shock relationship is that the characteristic wavelength of the acoustic waves is typically negligibly smaller than the shock radius of curvature for most of the shock region. Now the shock properties (orientation and strength), used for the calculations in Table 2.1, were obtained from flow visualization experiments. It would be useful at this stage to develop a model that can predict the shock properties (orientation and strength) given the microjet pressure. Appendix C gives the details of such a model. The model in Appendix C was validated by comparing its predictions with the flow visualization experiments. Such a model can be used in applications that require resulting shock properties given a jet-in-cross-flow, e. g. the present problem.

Another consequence of the presence of leading edge shock is the apparent change in the acoustic source strength which in the presence of the microjets is given as: $Q' \propto \rho_2 U_2^2$. Now from the shock relationship, $\frac{\rho_2}{\rho_\infty} > 1$ and $\frac{U_2}{U_\infty} < 1$, with the inequalities being not very far from unity. So we have $O\left(\frac{\rho_2 U_2^2}{\rho_\infty U_\infty^2}\right) = 1$. That is, the change in acoustic source strength is not expected to be significant due to the presence of shock.

2.3 Cavity Acoustics Model in the Presence of Microjets

This section describes a reduced order model for the cavity tones phenomenon under supersonic cross-flow and in the presence of leading edge microjets. Two cases are tackled: (i) microjets fired with uniform pressure along the leading edge (referred to as uniform control), and (ii) microjets fired with pressure that varies in a pre-defined manner along the leading edge (referred to as non-uniform control).

2.3.1 Uniform Control Case

Keeping the observations of Chapter 2.2 in mind, the reduced-order model in the presence of uniform microjets is derived as follows. Microjets are introduced in the cavity acoustics model through a forcing term addition to the momentum conservation equation while the mass conservation equation is left untouched. The reason, as mentioned before, is that the mass injection ratio $\left(\frac{\rho_{jet}U_{jet}A_{jet}}{\rho_\infty U_\infty L_{cavity}W_{cavity}}\right) < 1\%$ while the momentum injection ratio $\left(\frac{\rho_{jet}U_{jet}^2}{\rho_\infty U_\infty^2}\right) > 1$ for typical microjet pressure profiles. So the mass addition effect of the microjets is neglected. It may be noted here that the subscript '*jet*' refers to the mean flow conditions at the microjet nozzle exit.

Having neglected the mass contribution of microjets, the governing equations for this problem are given by Eqns. (2.1), (2.2) and the following momentum conservation equation:

$$\rho\frac{D\vec{u}}{\partial t} = -\nabla p + \vec{f}_\mu \tag{2.12}$$

Following the procedure adopted in obtaining Eqn. (2.5), we get:

$$\frac{\partial^2 p'}{\partial^2 t} - \bar{c}^2\nabla^2 p' = -\bar{c}^2\nabla\cdot\vec{f}_\mu \tag{2.13}$$

Now the forcing term on the right hand side of this equation can be obtained from the isentropic flow relationship applied at the microjet nozzle exit, with the mean nozzle flow assumed to be isentropic and sonic. The microjet flow structure at the nozzle exit is illustrated in Figure 2-8 and the detailed derivation of the forcing term is shown in Appendix D.

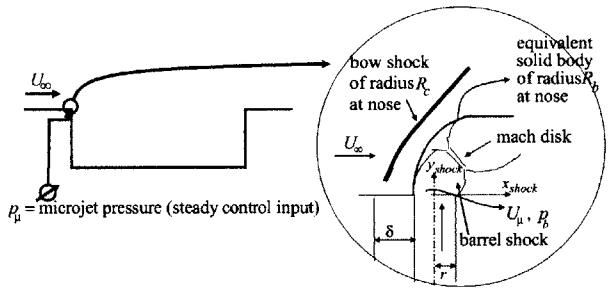

Figure 2-8: Close-up of flow structure near the exit of microjet nozzle in the presence of external cross-flow. Adapted from Papamoschou and Hubbard [16].

After deriving the forcing function, Green's function and method of images can be used

to get the pressure field inside the controlled cavity, as before. Using the separation of variables $p' \sim F(x,y)P(t)$, the governing equation for Green's function is given by (details given in Appendix D):

$$\frac{d^2P}{dt^2} + \frac{\partial U_\mu}{\partial y}(t)\frac{dP}{dt} + \omega'^2 P = 0 \tag{2.14}$$

which is the same as Eqn. (D.12) in Appendix D. Here, $\frac{\partial U_\mu}{\partial y}(t)$ is the transverse microjet velocity gradient at the jet exit and acts as the damping factor for the two-dimensional model, resulting in noise reduction.

Having obtained the governing equation for the Green's function, we proceed as follows. Eqn. (2.14) is simulated to find the forcing term, inertia term and the pressure perturbation response for a given microjet pressure input. The following ratio is then calculated:

$$\frac{\text{Forcing Term}}{\text{Inertia Term}} = \frac{\sum_{\omega'} F(x,y)\frac{\partial U_\mu}{\partial y}(t)\frac{dP}{dt}}{\sum_{\omega'} F(x,y)\frac{d^2P}{dt^2}} \tag{2.15}$$

where the summation is done over all Rossiter frequencies. On plotting this term versus the non-dimensional pressure perturbation term $\frac{p'}{\overline{p}}$ measured at the leading edge, it was found for all control inputs that the ratio $\frac{\text{Forcing Term}}{\text{Inertia Term}} \rightarrow 0.1$ (i.e., becomes negligible) after some time $t = t_s$. This is illustrated in Figures 2-9 and 2-10. So the forcing term is

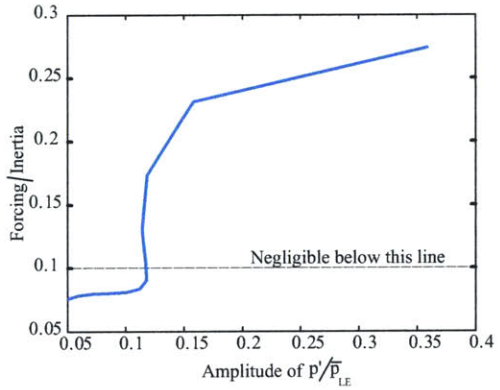

Figure 2-9: $\frac{\text{Forcing Term}}{\text{Inertia Term}}$ versus $\frac{p'}{\overline{p}}$ measured at the leading edge for 30 psig microjet pressure. External flow conditions: $M = 2.0$ and Re = 3 million (based on cavity length). Cavity dimension: $L/D = 5.1$.

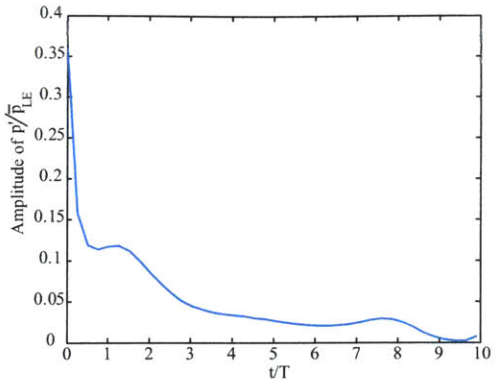

Figure 2-10: Response of $\frac{p'}{\overline{p}}$ measured at the leading edge (LE) for 30 psig microjet pressure. The initial conditions (at $t = 0$) correspond to uncontrolled cavity condition and were: $\frac{p'}{\overline{p}} = 0.36$ and $\frac{\partial p'}{\partial t} = 0$ (arbitrary). Also, T refers to the time period corresponding to the dominant cavity tone. External flow conditions: $M = 2.0$ and Re = 3 million (based on cavity length). Cavity dimension: $L/D = 5.1$.

switched off after time $t = t_s$ and the damping factor due to microjet introduction is then:

$$d_\mu = \frac{P(t_s)}{P(0)} \tag{2.16}$$

where $P(0)$ is the no-control value. After the forcing term is switched off, the pressure field resembles the uncontrolled field, except that the 'virtual' acoustic source strength is now reduced. So the damped solution is given by:

$$p'(x,y,t;\omega') \approx \frac{Q'}{2\pi}\left[H_0^{(1)}\left(\frac{\omega'}{\overline{c}}\sqrt{(L-x)^2+y^2}\right) + H_0^{(1)}\left(\frac{\omega'}{\overline{c}}\sqrt{(L+x)^2+y^2}\right) + H_0^{(1)}\left(\frac{\omega'}{\overline{c}}\sqrt{(L-x)^2+(y+2D)^2}\right)\right]\exp(i\omega' t) + (\cdot)^* \tag{2.17}$$

where the acoustic source strength in the presence of control is:

$$\frac{Q'}{Q} = d_\mu\left(\frac{\rho_2 U_2^2}{\rho_\infty U_\infty^2}\right) \approx d_\mu \tag{2.18}$$

The total pressure field is obtained by summing the pressure given by Eqn. (2.17) over all major Rossiter frequencies from $N = 1$ to 8 as follows:

$$p'(x,y,t) \approx \sum_{N=1}^{8} p'(x,y,t;\omega'_N) \tag{2.19}$$

The model predictions and the experimental results for the FSU cavity are compared in

Figures 2-11 and 2-12. The model and experimental results both show similar saturation

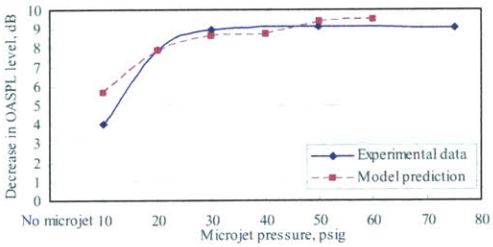

Figure 2-11: Model prediction versus experimentally observed OASPL reduction corresponding to the pressure transducer location at the middle of the leading edge. External flow conditions: $M = 2.0$ and Re $= 3$ million (based on cavity length). Cavity dimension: $L/D = 5.1$. Uncertainty in experimental OASPL: $\pm 1.0dB$.

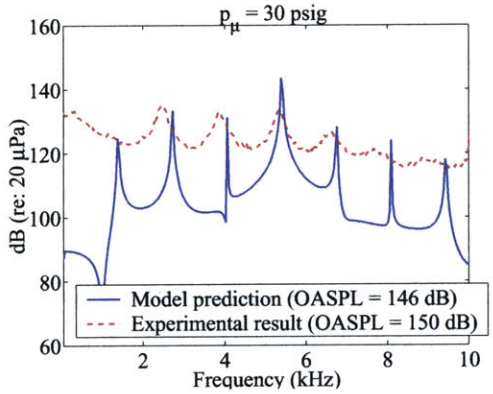

Figure 2-12: Model prediction versus experimentally observed SPL spectrum corresponding to the pressure transducer location at the middle of the leading edge and 30 psig microjet pressure. External flow conditions: $M = 2.0$ and Re $= 3$ million (based on cavity length). Cavity dimension: $L/D = 5.1$. Uncertainty in experimental SPL: $\pm 0.5dB$. Uncertainty in frequency: $\pm 40Hz$.

behavior in the noise reduction ability of microjets with increase in microjet pressure. Both suggest that for the FSU cavity, OASPL reduction at the leading edge is saturated for microjet pressure 30 psig and above. This validates the model ability to predict the correct trend in noise reduction with change in the control input. However, the prediction of the frequency spectrum for both the control-off (Figure 2-4) and control-on (Figure 2-12) situations is not good compared to the experiments. This can be attributed to a first order simplified model being used for this problem. Figure 2-13 shows the spectrum for control-off and control-on situations obtained from the FSU experiments. The figure illustrates the shift in frequency of the dominant tone that was mentioned earlier. Also, the FSU cavity shows a maximum SPL reduction of 20 dB and OASPL reduction of 9 dB at the leading

edge.

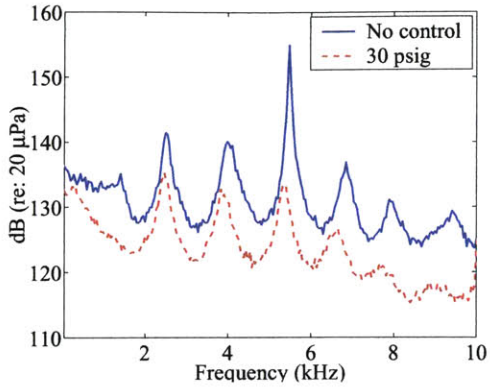

Figure 2-13: Experimentally observed SPL spectra corresponding to the pressure transducer location at the middle of the leading edge. The two spectra are for the microjets-off and 30 psig microjet pressure respectively. External flow conditions: $M = 2.0$ and Re = 3 million (based on cavity length). Cavity dimension: $L/D = 5.1$. Uncertainty in experimental SPL: $\pm 0.5dB$. Uncertainty in frequency: $\pm 40Hz$.

The following is an explanation for the observed saturation behavior. The reduction in OASPL is an increasing function of the magnitude of the damping factor. The latter, in turn, is an increasing function of the mean transverse microjet velocity gradient. The microjet velocity gradient varies with increasing microjet pressure as shown in Figure D-1 (Appendix D). Clearly the saturation in the microjet velocity gradient results in saturation in noise reduction inside the cavity. The reason for the saturation in microjet velocity gradient is not clear at this stage but Eqn. (D.15) in Appendix D provides some insight. It is evident that the barrel shock shape at the exit of the microjet nozzle must change increasingly slowly with increasing microjet pressure and converge to a particular shape at high microjet pressure in order for Figure D-1 to hold true. The validation for this hypothesis of the shock structure behavior requires the development of a relationship between the shock structure and microjet pressure. This in turn could be found using in-depth gas dynamic analysis (possibly two- or three-dimensional flow analysis) or using detailed flow visualization experiments done near the microjet nozzle exit but is not possible using current knowledge bank. This relationship, if developed in future, would shed light on the aforementioned behavior.

It is to be noted that the parameter, microjet-cross-flow momentum ratio as defined in Eqn. (C.2), is directly proportional to microjet pressure. Therefore, Figure 2-11 also shows saturation of the magnitude of noise reduction with increasing momentum ratio.

2.3.2 Non-Uniform Control Case

For the non-uniform control case, we need to consider the flow dynamics in the spanwise direction in addition to the details considered till now. But first, we discuss every conceivable flow dynamic mode that can be realized in a three-dimensional cavity. Table 2.2 shows all possible acoustic tones in the three-dimensional FSU cavity. However, the only observed

Table 2.2: All possible acoustic tones in the 3-D FSU cavity under $M = 2.0$ and Re = 3 million flow. Re is based on cavity length.

Type of tone	N = 1 (Hz)	N = 2 (Hz)	N = 3 (Hz)	N = 4 (Hz)
Rossiter tone, f_N	1417	2834	4250	5667
Streamwise tone, $f_L = \frac{\bar{c}}{2L}$	1506	3011	4518	6023
Spanwise tone, $f_W = \frac{\bar{c}}{2W}$	8748	17496	–	–
Streamwise tone, $f_D = \frac{\bar{c}}{4D}$	3822	11468	–	–

frequencies in the experiments were of the Rossiter tones because of their self-sustaining nature and this phenomenon is two-dimensional (i.e., is restricted to the streamwise and transverse plane). So the governing equations for the uncontrolled and controlled three-dimensional cases are Eqns. (2.5) and (2.13) respectively, i.e. same as in the two-dimensional model, except that separation of variables for the pressure perturbation field in the three-dimensional case is given by:

$$p' \sim P(t) F(x,y) \Phi(z) \equiv P(t) R(r) \Gamma(\phi) \Phi(z) \tag{2.20}$$

Here $\Phi(z)$ is a spanwise mode shape to be determined in chapter 3 and z is in the spanwise direction.

The solution process is development of Green's function and application of the method-of-images, same as in the two-dimensional case. The governing equation for Green's function is (details in Appendix E):

$$\frac{d^2P}{dt^2} + f_1(t) \frac{dP}{dt} + \omega'^2 P = 0 \tag{2.21}$$

where $f_1(t)$ is the three-dimensional damping factor that is obtained by integrating the

transverse microjet velocity gradient along the leading edge and is given by Eqn. (E.7) in Appendix E and repeated here for convenience.

$$f_1(t) = \frac{1}{\int_0^1 \Phi^2(z)\, d\left(\frac{z}{W}\right)} \left(\int_0^1 \Phi^2(z) \left[\sqrt{\frac{7RT_o}{30}} \frac{\xi}{\theta} \left\{ -p_{sq} + \left(\frac{5}{6}\right)^{\frac{7}{2}} \frac{p_r^{\frac{9}{7}}}{p_{sq}} \right\} - \sqrt{\frac{5RT_o}{42}} \frac{p_r^{\frac{2}{7}}}{p_{sq}} \frac{1}{p_b} \frac{\partial p_b'}{\partial y} \right] d\left(\frac{z}{W}\right) \right) \tag{2.22}$$

where the individual terms are defined in Appendix E. It follows that $f_1(t)$ consists of two components: (i) ξ which is the mean transverse microjet velocity gradient at the cavity leading edge and is independent of time, and (ii) the rest of the expression which are dependent on the ambient noise and thus on time. It also follows that an increase in ξ results in a larger value of $f_1(t)$ and thus causes a greater reduction in the cavity noise level. We now seek to find the relationship between the control input, p_μ and the damping factor, $f_1(t)$. From the results of flow visualization experiments shown in Figure D-1 of Appendix D, it follows that ξ and p_μ are increasing functions of each other. Moreover, if we replace ξ by p_μ in Eqn. (2.22) and remove the time-dependent term altogether, we get the following parameter:

$$\langle \Phi, \Phi \otimes p_\mu \rangle \triangleq \frac{\int_0^1 \Phi^2(z)\, p_\mu(z)\, d\left(\frac{z}{W}\right)}{\int_0^1 \Phi^2(z)\, d\left(\frac{z}{W}\right)} \tag{2.23}$$

where $\otimes$ represents the element-by-element multiplication of two vectors. It follows from the aforementioned argument that $f_1(t)$ is an increasing function of the parameter $\langle \Phi, \Phi \otimes p_\mu \rangle$ that, in turn, explicitly depends on p_μ. This relationship is exploited in the next chapter to optimize the control input for microjet-based cavity noise suppression.

It is noted that to account for the discrete number of microjets, the contribution of microjet velocity gradient in the integration done in Eqn. (2.22) was taken only at the points where the microjets are present. Also the pressure field inside the cavity for the

microjet-off and microjet-on cases, respectively, are as follows:

$$p'(x,y,t;\omega) \approx \frac{Q}{2\pi}\left[H_0^{(1)}\left(\frac{\omega}{\overline{c}}\sqrt{(L-x)^2+y^2}\right)+H_0^{(1)}\left(\frac{\omega}{\overline{c}}\sqrt{(L+x)^2+y^2}\right)+ H_0^{(1)}\left(\frac{\omega}{\overline{c}}\sqrt{(L-x)^2+(y+2D)^2}\right)\right]\Phi(z)\exp(i\omega t)+(\cdot)^* \quad (2.24)$$

$$p'(x,y,t;\omega') \approx \frac{Q'}{2\pi}\left[H_0^{(1)}\left(\frac{\omega'}{\overline{c}}\sqrt{(L-x)^2+y^2}\right)+H_0^{(1)}\left(\frac{\omega'}{\overline{c}}\sqrt{(L+x)^2+y^2}\right)+ H_0^{(1)}\left(\frac{\omega'}{\overline{c}}\sqrt{(L-x)^2+(y+2D)^2}\right)\right]\Phi(z)\exp(i\omega' t)+(\cdot)^* \quad (2.25)$$

where the acoustic source strength in the presence of control is given by Eqn. (2.18).

2.4 Summary

In this chapter, we developed a reduced-order model to describe the cavity tones under supersonic cross-flow, in the absence and presence of microjets. Further, two microjets-on cases were tackled: (i) microjets fired with uniform pressure along the leading edge (referred to as uniform control), and (ii) microjets fired with pressure that varies in a pre-defined manner along the leading edge (referred to as non-uniform control). The framework developed for the uncontrolled cavity tones model was based on the Navier-Stokes equation and order-of-magnitude analysis. The presence of microjets was treated by introducing an equivalent momentum flux to the cavity dynamics such that an active damper term was added to the governing equations. This chapter also describes the experimental arrangement used in Florida State University (FSU) for demonstrating the microjet-based cavity noise reduction phenomenon.

Chapter 3

Optimization of Control Input for Microjet-Based Cavity Noise Suppression

The three-dimensional acoustics model from Chapter 2 is used in this chapter to optimize the control input for noise suppression inside a cavity under supersonic cross-flow, while applying microjets at the leading edge. This study is limited to the control input being a steady spanwise microjet pressure distribution. In section 3.1, we give the problem formulation for optimizing the control input. Standard solution techniques for an optimal control problem are discussed in section 3.2. Section 3.3 gives an outline of the proper orthogonal decomposition and recursive proper orthogonal decomposition based techniques that are adopted here to optimize the control input for cavity noise suppression. In addition, section 3.4 discusses the experimental results of the optimization process and their implications, and section 3.5 summarizes the results of optimization of the control input for the cavity acoustics problem under supersonic cross-flow.

3.1 Problem Formulation

Since the aim is to maximize the amount of noise reduction inside the cavity by using microjets under a pre-specified mass flow constraint, the relevant optimization problem can

be defined as follows:

$$\begin{aligned} &\text{Maximize } f_1(t) \\ &\text{subject to mass flow constraint} \end{aligned} \tag{3.1}$$

where $f_1(t)$ is the damping factor defined in Eqn. (2.22). This follows the rationale that maximizing the damping factor would result in maximum noise reduction. Also from section 2.3.2, we know that $f_1(t)$ is an increasing function of the parameter $\langle \Phi, \Phi \otimes p_\mu \rangle$. Therefore, the optimization problem (3.1) can be reformulated as:

$$\begin{aligned} &\text{Maximize } \langle \Phi, \Phi \otimes p_\mu \rangle \\ &\text{subject to mass flow constraint} \end{aligned} \tag{3.2}$$

3.2 Standard Optimal Control Solution Methods

When optimal control formulations for a linear process involve a quadratic performance criterion, the Liapunov equation technique found in standard control textbooks such as [18] guarantees the existence of the optimal control input. In this case, a linear control law suffices. However, the determination of the optimal control law for non-quadratic performance criterion, and possibly for nonlinear processes, must be approached by the methods of the calculus of variations or dynamic programming. The general methods of obtaining the optimal control law using the variational approach are obtained from a standard textbook on optimal control theory, such as [19] or [20]. Also, Ref. [21] outlines the theory and application of optimal control theory specifically for nonlinear processes. In Ref. [22], the technique of dynamic programming is used to derive the optimal control law for both linear and nonlinear processes.

3.3 New Approach for Optimizing Control Input

In the optimization problem for cavity noise suppression given in Eqn. (3.2), the performance criterion is expressed in terms of Φ and the control input p_μ, where Φ is as yet not determined. Hence, the standard tools mentioned in section 3.2 for determining the optimal control strategy is not useful here. Instead, we adopt proper orthogonal decomposition

(POD) and recursive proper orthogonal decomposition (RePOD) based techniques here to obtain an estimate of the optimal control strategy. The rest of this section is organized as follows. Sections 3.3.1 and 3.3.2 outline the POD algorithm and the POD-based technique for obtaining an estimate of the optimal control strategy, respectively. Lastly, section 3.3.3 describes the RePOD-based technique for obtaining an estimate of the optimal control strategy.

3.3.1 Proper Orthogonal Decomposition

In order to solve the optimization problem given by Eqn. (3.2), the spanwise mode shape $\Phi(z)$ is required and the analysis done so far does not provide a procedure for obtaining $\Phi(z)$. However, it is desired to have $\Phi(z)$ such that the error between the pressure perturbation signal and the expression used in its place in Eqn. (2.20), i.e. $\|p' - P(t) F(x,y) \Phi(z)\|$, is minimized for given x and y (z and t being the variables of interest here). This is equivalent to performing a proper orthogonal decomposition (POD) on p' in z and t. The algorithm for performing POD is given below.

Expressing p' as a function of only z and t, and noting that $p'(z,t)$ is a zero-mean flow variable, the POD method seeks to generate an approximation for p' by using separation of variables as

$$p'(z,t) = \sum_{i=1}^{l} a_i(t)\phi_i(z) \tag{3.3}$$

where $a_i(t)$ is the ith temporal amplitude, $\phi_i(z)$ is the ith spatial basis function, l is the number of modes chosen, and t and z are the temporal and spatial variables respectively.

The set of realizations from a plant required for the POD basis calculation is typically obtained experimentally or computationally and as such is discrete in nature. So, what follows in this section refers to discrete nature of the variables concerned.

Let m be the number of temporal points in the flow data ensemble, and n be the number of spatial points (depending upon the number of sensors). The POD method consists of finding $\phi_i(z)$ such that the projection error $p'(x,t) - p'(z,t)$ is minimized. This optimization problem can be stated as follows. Denote $\{\phi_i(z)\}_{z=z_1,\ldots,z_n} = \phi_i \in \Re^n, i = 1, \cdots, l$. The

optimization problem is then given by:

$$\begin{aligned} &\text{Min } J_m(\phi_1, \cdots, \phi_l) = \sum_{j=1}^{m} \|Y_j - \sum_{k=1}^{l} (Y_j^T \phi_k)\phi_k\|^2 \\ &\phi \\ &\text{subject to : } \phi_i^T \phi_j = \delta_{ij}, 1 \leq i, j \leq l, \phi = [\phi_1, ..., \phi_l] \end{aligned} \tag{3.4}$$

where $Y_j \in \Re^n$ is the vector of flow data p' at time $t = t_j$, i.e. $Y_j = \{p'(z_1, t_j), \cdots, p'(z_n, t_j)\}$. Also, $(Y_j^T \phi_k)$ in the cost function is the kth temporal amplitude a_k at time t_j. So the expression within the first summation sign is $\|Y_j - \sum_{k=1}^{l} a_k \phi_k\|^2$ which refers to the projection error for the data Y_j. The constraints imply that $\{\phi_i | i = 1, \cdots, l\}$ satisfy the conditions of orthonormality.

From Volkwein [17], ϕ from Eqn. (3.3) is a POD modal set if it is a solution to the optimization problem (3.4) for any value of $l < m$. The POD modal set can be obtained using the method of snapshots [23, 24] as follows.

Denote $Y_j(z_k) = p'(z_k, t_j)$. Also, let the matrix Y be formed as follows: $Y = [Y_1^T, \cdots, Y_m^T]$. Then, a singular value decomposition of the matrix Y gives: $Y = B\Sigma A^T$, where A and B are unitary matrices, and

$$\Sigma = \begin{bmatrix} \sigma_1 & & & \\ & \sigma_2 & & \\ & & \ddots & \\ & & & \sigma_l \end{bmatrix}, \sigma_1 \geq \sigma_2 \geq \cdots \geq \sigma_l.$$

Then

$$\phi_i(z_k) = \sum_{j=1}^{m} \frac{A(j,i) Y_j(z_k)}{\sigma_i}, i = 1, ..., l; k = 1, ..., n. \tag{3.5}$$

The eigenvalues corresponding to the POD modes are the squares of the singular values $\{\sigma_1^2, \sigma_2^2, \cdots, \sigma_l^2\}$, and represent the 'energy content' of the modes.

3.3.2 POD-Based Optimization Procedure

The POD-based optimization procedure is as follows.

1. Measure pressure data from sensors distributed at a particular x, y with varying z and

t, for the case of flow without microjets.

2. Perform a proper orthogonal decomposition on the data snapshots collected in step 1 by the method shown in section 3.3.1.

3. Determine the dominant spanwise mode shape and denote it as $\Phi(z)$ as used in Eqn. (3.2).

4. Perform steps 1-3 for various microjet pressure distributions and obtain the corresponding OASPL reduction magnitude in each case.

5. Plot the OASPL reduction versus $\langle \Phi, \Phi \otimes p_\mu \rangle$.

6. Identify the best microjet pressure profile from this plot.

Steps 4 and 6 need further explanations. From Figure 2-11 and from the similar governing equations of the uniform and non-uniform control problems given by Eqns. (2.14) and (2.21), respectively, we expect the cavity to exhibit a similar saturation behavior in the noise reduction ability of microjets with increase in $\langle \Phi, \Phi \otimes p_\mu \rangle$ for the non-uniform control problem. Therefore, the microjet pressure distributions used in step 4 are varied so as to obtain $\langle \Phi, \Phi \otimes p_\mu \rangle_1 < \langle \Phi, \Phi \otimes p_\mu \rangle_2 < \langle \Phi, \Phi \otimes p_\mu \rangle_3 < \cdots$ until saturation is observed. This can be realized by gradually increasing the mean microjet pressure profile. In step 6, the best microjet profile corresponds to the minimum $\langle \Phi, \Phi \otimes p_\mu \rangle$ that satisfies the mass flow constraint and provides maximum noise reduction. This solution, based on the aforementioned physical insight, is thought to provide a good estimate of the optimal solution to Eqn. (3.2).

3.3.3 RePOD-Based Optimization Procedure

The approximate optimal control strategy derived so far is a particular case of the general real-time control theory that requires the implementation of an on-line proper orthogonal decomposition of the data snapshots collected from the cavity pressure sensors and on-line variation of microjet pressure. The latter is based on solving Eqn. (3.2) in a real-time environment. Now, the theory and procedure of realizing on-line proper orthogonal decomposition is given in Ref. [25]. A summary of the technique of recursive proper orthogonal decomposition (RePOD) is given here.

Suppose we begin at time t_m, with the flow data set $[Y_1^T, ..., Y_m^T]$, where the notations are given in section 3.3.1. When a new measurement set Y_{m+1} at time t_{m+1} is given, then the updated basis function is given by:

$$\begin{aligned}\phi_i^{(m+1)} &= \phi_i^{(m)} - s\left.\frac{\partial \Delta J}{\partial \phi_i}\right|_{\phi_i=\phi_i^{(m)}} \qquad (s>0) \\ &= \phi_i^{(m)} + s\left(Y_{m+1} - \sum_{k=1}^{l}(Y_{m+1}^T\phi_k)\phi_k\right)\left(Y_{m+1}^T\phi_i\right)\Big|_{\phi_i=\phi_i^{(m)}} \qquad (3.6)\end{aligned}$$

where $i = 1, \cdots, l$, s is a step-size chosen suitably (typically, by inspection) and the superscripts '(m)' and '$(m+1)$' on the mode shape refer to the computation done at time t_m and t_{m+1} respectively.

Also, on-line variation of microjet pressure can be implemented by an appropriate choice of valves to modify the pressure such that the response time of the valves is significantly slower than the time scale associated with the dominant Rossiter tone. This requirement enables us to use the on-line proper orthogonal decomposition algorithm given in Eqn. (3.6). Finally, the optimization problem Eqn. (3.2) can be solved real-time using standard techniques[26].

3.4 Experimental Results

The POD-based approximate optimal control solution of Eqn. (3.2), as given in section 3.3.2, was experimentally implemented using the FSU cavity with four leading edge and three trailing edge pressure sensors, and one sensor in the middle of the leading edge face of the cavity. These sensors were used for computing $\Phi(z)$ in the optimization process. The results are outlined in Figure 3-1 for the leading edge.

Both model and experimental results (Figure 3-1(b)) show similar saturation behavior in the noise reduction ability of microjets at the leading edge with increase in microjet pressure. In fact, the point of saturation suggested by the model and experiments is around $\langle \Phi, \Phi \otimes p_\mu \rangle = 30$ psig. This validates the model ability to predict the correct trend in noise reduction with change in the control input, as in the two-dimensional case. Also the optimal control input can be chosen, based on the mass flow constraint. However, as expected, the prediction of the frequency spectrum for the control-on (Figure 3-1(a)) situation is not good compared to the experiments and is henceforth not discussed.

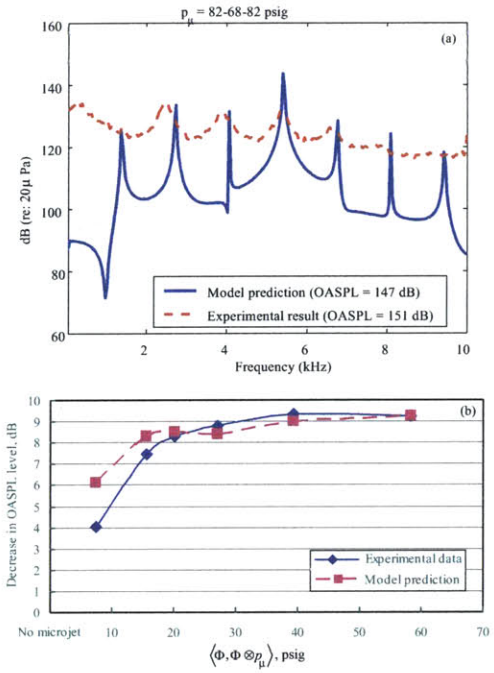

Figure 3-1: Model prediction versus experimentally observed SPL spectrum (a) and OASPL reduction (b) corresponding to the pressure transducer location at the middle of the leading edge. External flow conditions: $M = 2.0$ and Re $= 3$ million (based on cavity length). Cavity dimension: $L/D = 5.1$. Uncertainty in experimental SPL: $\pm 0.5dB$. Uncertainty in frequency: $\pm 40Hz$. The microjet pressure naming convention is based on Figure 2-6.

It may be noted that it was not possible to directly measure $\Phi(z)$ from the leading edge sensors in the presence of microjets because lack of space excluded the possibility of including both microjets and sensors at the leading edge. A multivariate ARX model (details in Appendix F) was used to predict the leading edge sensor readings from the trailing edge pressure sensors for various microjet pressure profiles. $\Phi(z)$ was computed using the predicted leading edge pressure data. It was found that the predicted normalized $\Phi(z)$ was very similar to the experimentally obtained one from the microjet-off case. Hence, $\Phi(z)$ used in Figure 3-1 was obtained from the experimental leading edge pressure data under the control-off condition.

Optimization results for the trailing edge are shown in Figure 3-2. The figure clearly illustrates the effect of saturation of the noise suppression ability of steady microjets although here the noise reduction after saturation is not as flat as in the leading edge case. While implementing the optimization process, the presence of trailing edge sensors made it possible to estimate $\Phi(z)$ for each case of microjet input. This proved fortuitous when com-

pared to the leading edge optimization process because the mode shape at the trailing edge varied with different microjet input. Also, it was observed[1] that there is a poor coherence between the leading and trailing edge sensor readings except at the Rossiter frequencies. Hence the cavity acoustics model is expected to predict the trailing edge noise not as well as at the leading edge. This is because the model relies on good coherence between the two. The relative poorer model performance is illustrated in the form of a gap between the model-predicted and experimentally obtained noise reduction at high microjet pressures in Figure 3-2. On the other hand, the gap between the two is close to the uncertainty in the trailing edge pressure sensor; hence we consider the model to be validated. Also based on the model and experimental data, we can take the point of saturation as $\langle \Phi, \Phi \otimes p_\mu \rangle = 30$ psig because increasing microjet pressures further does not result in drastic gain in resulting noise reduction.

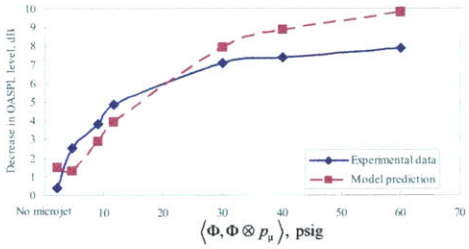

Figure 3-2: Model prediction versus experimentally observed OASPL reduction corresponding to the pressure transducer location at the middle of the trailing edge. External flow conditions: $M = 2.0$ and Re $= 3$ million (based on cavity length). Cavity dimension: $L/D = 5.1$. The uncertainty in the pressure sensor reading was $\pm 1.5dB$ and in frequency was $\pm 40Hz$. Also the initial conditions for determining d_μ were: $\frac{p'}{\bar{p}} = 1.98$ and $\frac{\partial p'}{\partial t} = 0$ (arbitrary).

It is to be noted that the parameter, microjet-cross-flow momentum ratio as defined in Eqn. (C.2), is directly proportional to the microjet pressure. The reason is that in the expression for momentum ratio given in Eqn. (C.2), the term jet density is proportional to the microjet pressure. Therefore, Figures 3-1(b) and 3-2 also show saturation of the magnitude of noise reduction at the leading and trailing edges, respectively, with increasing momentum ratio.

3.5 Summary

In this chapter, we derived an estimate for an optimal control strategy that guarantees noise suppression inside a cavity under supersonic cross-flow, while applying microjets with steady pressures at the leading edge. The derivation was based on the three-dimensional acoustics model from Chapter 2 and on proper orthogonal decomposition of the pressure perturbation data along the spanwise direction at the desired location inside the cavity. The strategy was implemented using the FSU experimental setup and illustrated saturation of the noise reduction ability of microjets above a certain pressure level. Because of the early saturation behavior of the cavity acoustics system, the RePOD-based optimal control strategy is not necessary for this problem. On the contrary, the best estimate for the optimal control strategy is to fire the microjets with a steady pressure profile that satisfies the mass flow constraint and corresponds to a value of $\langle \Phi, \Phi \otimes p_\mu \rangle$ which is as close to the saturation point as possible. Since a particular value of $\langle \Phi, \Phi \otimes p_\mu \rangle$ can result from several $p_\mu(z)$ profiles, it follows that the best estimate does not give a unique microjet pressure distribution for the cavity acoustics problem under supersonic cross-flow.

Chapter 4

Store Separation From Bay Under Supersonic Cross-Flow

In chapters 2 and 3, we developed and validated an approximate optimal control strategy for suppressing noise inside a cavity under supersonic cross-flow using leading edge microjets. The next problem is to use microjet-based actuator to control the trajectory of a store that is released from inside the cavity into external supersonic flow with the goal of achieving a safe drop. This can be done by deriving a low order model for predicting the correct trend in the store trajectory in the presence of microjets. This chapter outlines the development of an appropriate low order model in section 4.1. In section 4.2, we analyze the low-order in terms of the store drop behavior for two cases: (I) when microjets are off, and (II) when the microjets are switched on. We then compare the low order model predictions with results from experiments performed under the DARPA-funded HIFEX Program [2, 3, 4] in section 4.3. Finally in section 4.4, we describe an optimization process to find the best control input (in terms of microjet-free-stream momentum ratio) that would ensure a successful store drop from a cavity under supersonic cross-flow.

4.1 Store Release Model Development

The model, used to optimize the microjet-based control input for safe store ejection, is restricted to the pitch and plunge motion of the store. Additionally, it is assumed that the store release is an ejected drop from the middle of the cavity. The development of the store release model is further based on the following five major assumptions:

(M1) The store is thin and axi-symmetric, and the vertical store velocity and angle of attack are small. Then the following hold true:

$$\delta = \frac{\hat{a}_o}{\hat{l}_o} \ll 1, \frac{\hat{V}_r}{\delta U_\infty} = \epsilon \leq O(1), \alpha = \frac{\hat{\alpha}}{\delta} = O(1). \tag{4.1}$$

Here $\hat{}$ indicates dimensional quantities, l_o is the store length, a_o is the maximum store radius, V_r is the characteristic plunge speed, U_∞ is the undisturbed free stream velocity and δU_∞ is the scale of the vertical velocity perturbations in the external free stream. Also $\hat{\alpha}$ is the store angle of attack in radians and α is the appropriately scaled angle of attack. Eqn. (4.1) illustrates the slender body assumption that is later used to simplify the model governing equation. A related extension to this set of assumptions is flow attachment to the store surface at all stages in the store trajectory. These assumptions are not critical when the store successfully departs from the cavity. However, they become critical after the store starts to return towards the cavity because it tends to exhibit large angle of attack followed by flow separation. Now, since the objective of this model is to predict whether the store departs successfully or not, we are justified in applying this set of assumptions to predict the store vertical motion till the point where the store starts to turn back into the cavity or till the store makes a successful drop outside the cavity.

(M2) The shear layer geometry is governed by:

$$\frac{\hat{\delta}_s}{\hat{a}_o} \ll 1 \tag{4.2}$$

where $\hat{\delta}_s$ is the shear layer thickness. In other words, Eqn. (4.2) illustrates the thin shear layer assumption which implies that the shear layer can be treated as a flat free slip surface with a tangential velocity jump and continuous normal velocity, pressure and density across itself. A related extension to this assumption is that the wavy structures that form inside the thin shear layer have a small slope.

(M3) The external cross-flow is of high Reynolds number, i.e.

$$\delta^2 Re \gg 1, Re = \frac{\hat{\rho}_\infty U_\infty \hat{l}_o}{\hat{\mu}_\infty}. \tag{4.3}$$

Here Re is the Reynolds number based on the store length, $\hat{\rho}_\infty$ is the free stream density and $\hat{\mu}_\infty$ is the free stream viscosity coefficient. This assumption allows us to neglect viscous forces on the store.

(M4) Based on the slender body assumption (1), the shock waves associated with the store nose when it is facing the external supersonic cross-flow are expected to be considerably weak and consequently can be replaced by Mach waves. In addition, with the application of flow injectors at the leading edge and upstream end of the cavity, shock waves are introduced, as illustrated in Figure 4-1. It is reasonable to assume that the

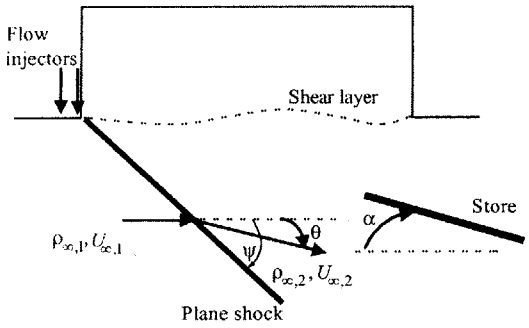

Figure 4-1: Shock geometry outside the cavity due to application of microjet-based flow injectors at the leading edge and upstream end.

associated shock wavefront radius is much greater than the store radius so that the incident shock can be treated as a plane shock for this problem. Plane shock theory together with assumptions (3) and (4) allow us to apply slender body potential flow theory to the store when it is outside the cavity. Moreover, if the store is released sufficiently away from the cavity leading edge, the store is not expected to intersect the microjet shock line and so the associated diffractive effects can be neglected.

(M5) The mean convective flow inside the cavity is ignored. In practice, a reverse flow with speeds up to 40% of the external flow stream has been observed. This is neglected in this low-order proposed model. Thus, the store drop model consists of the motion of a slender axi-symmetric body in a quiet medium inside the cavity. In addition, the acoustic field inside the cavity due to Rossiter tones [Chapter 2] is neglected. The reason is that the associated time fluctuations are short on the time scale of dropping of the store [31]. In fact, the Strouhal number of dominant Rossiter tones is $O(10)$ while that associated with store drop is negligibly less than 1.

The model also incorporates the factors that affect the store plunge and pitch motion given in Figure 1-8, out of which, the wavy structures, the store induced potential, the leading edge microjets and gravity can be treated as the primary factors and the cavity walls as boundary conditions. We limit the scope of the model to first order effects since we can introduce these factors separately.

The procedure employed for developing the first order model is as follows: Assumptions (M2)-(M5) allow the use of potential function in solving the velocity field associated with store motion. Using this method, it is first shown that because of the thin shear layer and the thin store diameter, the wavy structures provide negligible influence on aerodynamic forces and moments on the store. It is then shown that the velocity potential induced by the store motion as it drops from inside the cavity satisfies the Laplace Equation in the cross-section plane. Owing to the linearity of the problem, the Laplace Equation is solved separately for the cases when the store is inside the cavity, when it crosses the shear layer and when it is completely outside the cavity. The technique used for solving the Laplace Equation is a combination of multipole expansion and conformal transformation.

The resulting model predicts that when the store just exits the cavity in the no-control case, it experiences an aerodynamic force (in a direction normal to the external flow) and pitching moment such that the linear velocity of the store becomes positive and the store starts to return back to the cavity. When microjets are switched on, the external flow stream is changed so that the force and moment on the store are altered mainly when the store passes through the shear layer and when it is completely outside the cavity. These changes cause the store to drop successfully from the cavity. The model is also used to predict that when the microjet pressures are increased to higher values, the nonlinearities in the normal force and moment cause the store to return back towards the cavity. These predictions are then corroborated with experimental results [4]. Finally, the model is used to optimize the control input in order to ensure safe store drop under a variety of drop conditions.

4.1.1 General Governing Equation for Two Dimensional Model

Before deriving the two dimensional first order model, we consider the general problem of a slender axi-symmetric body falling through a cross-flow in the absence of viscosity and body forces. To derive the governing equation for this problem, we use the equation of

continuity:

$$\frac{1}{\hat{\rho}}\frac{D\hat{\rho}}{\partial \hat{t}} + \nabla \cdot \vec{Q} = 0, \tag{4.4}$$

Bernoulli's equation for irrotational flow:

$$\int_{\hat{p}_\infty}^{\hat{p}} \frac{d\hat{p}}{\hat{\rho}} = -\frac{\partial \Phi}{\partial \hat{t}} - \frac{1}{2}\left(Q^2 - U_\infty^2\right), \tag{4.5}$$

and the isentropic flow relationship:

$$c^2 = \frac{d\hat{p}}{d\hat{\rho}}, \tag{4.6}$$

where $\hat{p}$ is the local pressure, $\hat{\rho}$ the flow density, Q the velocity field and c the sound speed. Also $\hat{p}_\infty$ is the free stream pressure and U_∞ the free stream cross-flow velocity. By eliminating density and introducing the velocity potential Φ, we get the full unsteady potential equation [36] for the pitch and plunge store motion as follows:

$$\nabla^2 \Phi = \frac{1}{c^2}\left[\frac{\partial^2 \Phi}{\partial \hat{t}^2} + \frac{\partial Q^2}{\partial \hat{t}} + \vec{Q} \cdot \nabla\left(\frac{Q^2}{2}\right)\right] \tag{4.7}$$

Moreover the relation between local sound speed and sound speed under free stream conditions is given by:

$$c^2 = c_\infty^2 - (\gamma - 1)\left[\frac{\partial \Phi}{\partial \hat{t}} + \frac{1}{2}\left(Q^2 - U_\infty^2\right)\right]. \tag{4.8}$$

Here γ is the ratio of specific heats and c_∞ is the free stream sound speed. In the presence of plane shock near the cavity leading edge, these quantities refer to the region in front of the shock. Gravity does not influence the velocity potential as the associated Froude number $Fr = \frac{U_\infty^2}{\hat{g} l_o} \gg 1$, where g is the acceleration due to gravity. The reference frame for this particular problem is illustrated in Figure 4-2.

4.1.2 Contribution of Wavy Structures to Store Force and Moment

We now consider the effect of the wavy shear layer structures on the normal force and pitching moment on the store. A shear layer is typically formed between the no-mean-flow inside the cavity and the external uniform flow outside the cavity. Small vortical disturbances

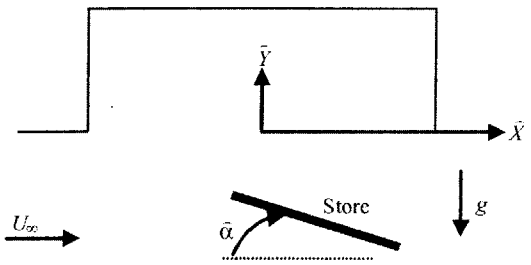

Figure 4-2: Reference frame for the general problem of a slender axi-symmetric store falling through a cross-flow in the absence of viscosity and body forces.

which originate at the upstream boundary layer and at the leading edge due to excitation by the Rossiter tones [Chapter 2], get amplified as they propagate downstream inside the shear layer. This gives rise to wavy shear layer structures that convect downstream. These wavy structures result in non-uniformity in the flow domain outside the cavity. Then the shear layer, according to assumption (M2), can be treated as a free slip surface with a tangential velocity jump and continuous normal velocity, pressure and density across itself, with the slip surface now consisting of wavy structures.

Because of assumption (M5), we can use the full potential equation given by Eqns. (4.7) and (4.8) to model the velocity potential induced by the wavy shear layer structures. To identify the expression for the loads, the technique of Ref. [33] is adopted in which a combination of non-dimensional analysis and the method of perturbations is used to identify the dominant terms in Eqns. (4.7) and (4.8). Then we perform an order of magnitude analysis on the force and moment expressions to quantify the effect of the wavy structures.

The non-dimensional scheme is given by:

$$X' = \frac{\hat{X}}{\hat{L}_o}, Y' = \frac{\hat{Y}}{\hat{L}_o}, Z' = \frac{\hat{Z}}{\hat{L}_o} \tag{4.9}$$

where $\hat{L}_o$ is the cavity length. Another useful parameter to consider is the Strouhal number $S = \frac{\hat{l}_o}{\hat{t}_o U_\infty}$ where $\hat{t}_o = \sqrt{\frac{\delta \hat{l}_o}{\hat{g}}}$ is the characteristic time scale for the store plunge motion. Now, since we are interested in finding the first order effect of the presence of the wavy structures, we neglect the presence of the store. In that case, the method of perturbations results in:

$$\Phi = U_{\infty,r}\left[\hat{X} + \hat{L}_o \delta_s \bar{\phi} + \cdots\right] \tag{4.10}$$

where $U_{\infty,r}$ is the external cross-flow velocity relative to the wavy shear layer structure and is typically $\frac{U_\infty}{2}$. Also $\bar{\phi}$ is the perturbation velocity potential induced by the wavy structures. Here it is assumed that the wavy structures are uniform along the cavity width. The explanation is that the cavity dynamics dominated by Rossiter tones [Chapter 2] can be treated as two-dimensional and microjets, whenever present, are fired uniformly along the spanwise direction. For a two-dimensional flow problem, the flow perturbation [37] is of the order δ_s, where $\delta_s = \frac{\hat{\delta}_s}{\hat{L}_o} \ll 1$.

Next, we substitute Eqn. (4.10) in (4.7) and (4.8), and use (4.9) to get:

$$\left[\frac{1}{M_{\infty,r}^2} - (\gamma-1)\,\delta_s\left(\frac{S}{\mu}\bar{\phi}_t + \frac{1}{2}\left(\delta_s\bar{\phi}_X^2 + \delta_s\bar{\phi}_Y^2 + 2\bar{\phi}_X\right)\right)\right]\left[\bar{\phi}_{XX} + \bar{\phi}_{YY}\right]\mu\delta_s = S^2\frac{\delta_s}{\mu}\bar{\phi}_{tt} + 2S\delta_s\left[\delta_s\bar{\phi}_X\bar{\phi}_{Xt} + \bar{\phi}_{Xt} + \delta_s\bar{\phi}_Y\bar{\phi}_{Yt}\right] + \mu\delta_s\left[\left(1+\delta_s\bar{\phi}_X\right)^2\bar{\phi}_{XX} + \delta_s\bar{\phi}_Y^2\bar{\phi}_{YY}\right] \tag{4.11}$$

where $\mu = \frac{\hat{l}_o}{\hat{L}_o} \leq O(1)$. Eliminating terms with $\delta_s, \delta_s^2, \delta_s^3, \cdots$ and assuming $S < \delta_s$, we get:

$$\beta^2\bar{\phi}_{XX} - \bar{\phi}_{YY} = 0 \tag{4.12}$$

where $\beta^2 = M_{\infty,r}^2 - 1$.

Assuming that the wavy structure has small slope, the associated boundary condition is given by [33]:

$$\left.\frac{\partial\bar{\phi}}{\partial Y'}\right|_{Y'=0} = \frac{dh(X')}{dX'} \tag{4.13}$$

where the non-dimensional wavy structure shape is given by:

$$Y_w' = \delta_s h(X'),\, h(\cdot) = O(1). \tag{4.14}$$

This boundary condition implies that the perturbation velocity normal to the wavy structure varies as the slope of the structure which is because the flow represented by $\bar{\phi}$ is tangential to the wavy structure, to a first order.

The problem is solved to give [33]:

$$\bar{\phi} = \frac{1}{\beta}h(X' + \beta Y'). \tag{4.15}$$

Next, we convert the velocity potential from Eqn. (4.15) to pressure as follows [33]:

$$\bar{p} = -\bar{\phi}_{X'} = -\frac{1}{\beta} h'\left(X' + \beta Y'\right) \tag{4.16}$$

where the prime on $h(\cdot)$ indicates differentiation, pressure is non-dimensionalized with respect to $\left(\hat{\rho}_\infty U_\infty^2\right)_r \delta_s$ and the other variables are non-dimensionalized using the scheme given in Eqn. (4.9).

Integrating this pressure along the store cross-section and axis gives the normal force and pitching moment on the store [33]:

$$\begin{aligned} F_w &= -\delta_s \int_{x_o}^{x_e} \int_0^{2\pi} \bar{p}\left(X_c' + \mu x + \beta Y_s'\right) a(x) \sin\theta \, d\theta dx \\ M_w &= -\delta_s \int_{x_o}^{x_e} \int_0^{2\pi} \bar{p}\left(X_c' + \mu x + \beta Y_s'\right) x a(x) \sin\theta \, d\theta dx \end{aligned} \tag{4.17}$$

where (X_c', Y_c') are the store c. g. coordinates in the $X' - Y'$ system, $X_c' + \mu x$ is the X'-coordinate of a point on the store surface, $Y_s' = Y_c' - \mu\delta\alpha x + \mu\delta a(x)\sin\theta$ is the Y'-coordinate of the point and θ is the angle formed between the point and the reference at the store axis, as illustrated later in Figure N-1. Also the force and moment expressions are non-dimensionalized by $\left(\hat{\rho}_\infty U_\infty^2\right)_r \delta_s \hat{l}_o^2$ and $\left(\hat{\rho}_\infty U_\infty^2\right)_r \delta_s \hat{l}_o^3$ respectively.

In this thesis, we further estimate the order of magnitude of F_w and M_w from these expressions. Without any loss of generality, we further assume that the wavy structures consist of piecewise cosine components, such as:

$$h(X') = W_i \cos\left(\lambda_i X' + \zeta_i\right) + R_i \tag{4.18}$$

where i is an integer, $W_i = O(1)$ and $\lambda_i = O(10)$. Then we have:

$$\begin{aligned} |F_w| &\leq \pi\mu\delta_s\delta \max_i \left(W_i\lambda_i^2\right) G_0 \\ |M_w| &\leq \pi\mu\delta_s\delta \max_i \left(W_i\lambda_i^2\right) G_1. \end{aligned} \tag{4.19}$$

where $G_0 = \int_{x_o}^{x_e} a^2(x)\, dx$, $G_1 = \int_{x_o}^{x_e} a^2(x)\, x\, dx$, $x = \frac{\hat{x}}{\hat{l}_o}$, $a = \frac{\hat{a}}{\delta \hat{l}_o}$ and (x_o, x_e) are the nose and tail coordinates of the store.

Since $G_0 \leq O(1)$, $G_1 \leq O(1)$, $\delta \ll 1$ and $\delta_s \ll 1$, we have $|F_w| \ll 1$ and $|M_w| \ll 1$. Thus because of slender body and small thickness of wavy structures, the effect of the wavy

structures on the normal force and moment on the store is negligible.

The remaining factors affecting the pitch and plunge motion of the store are the store-induced velocity potential as it drops from the cavity, the shock waves due to microjets and gravity. We consider the first factor below.

4.1.3 Store Motion Induced Velocity Potential

To derive the velocity potential associated with store motion inside and outside the cavity, we identify the dominant terms of the general governing equations given by Eqns. (4.7) and (4.8) by a combination of non-dimensional analysis and method of perturbations as before, following Ref. [33]. The non-dimensional scheme is:

$$X = \frac{\hat{X}}{\hat{l}_o}, Y = \frac{\hat{Y}}{\delta \hat{l}_o}, Z = \frac{\hat{Z}}{\delta \hat{l}_o}, t = \frac{\hat{t}}{\hat{t}_o} \tag{4.20}$$

Using the method of perturbations, we ignore the wavy structures (which do not produce appreciable force and moment on the store) and set [33]:

$$\Phi = U_\infty \hat{l}_o \left[X + \delta^2 \phi + \cdots \right] \tag{4.21}$$

keeping in mind that the dominant flow perturbation is of order δ^2 for a body of revolution [37]. Here ϕ is the perturbation velocity potential. Now, substituting Eqn. (4.21) in (4.7) and (4.8), and using (4.20), we get:

$$\begin{aligned}
&\left[\frac{1}{M_\infty^2} - (\gamma - 1)\, \delta^2 \left(S\phi_t + \frac{1}{2} \left(\delta^2 \phi_X^2 + \phi_Y^2 + \phi_Z^2 + 2\phi_X \right) \right) \right] \left[\delta^2 \phi_{XX} + \phi_{YY} + \phi_{ZZ} \right] = \\
&S^2 \delta^2 \phi_{tt} + 2S\delta^2 \left[\delta^2 \phi_X \phi_{Xt} + \phi_{Xt} + \phi_Y \phi_{Yt} + \phi_Z \phi_{Zt} \right] + \delta^2 \left(1 + \delta^2 \phi_X \right) \left[\delta^2 \phi_X \phi_{XX} + \right. \\
&\left. \phi_{XX} + \phi_Y \phi_{XY} + \phi_Z \phi_{XZ} \right] + \delta^2 \phi_Y \left[\delta^2 \phi_X \phi_{XY} + \phi_{XY} + \phi_Y \phi_{YY} + \phi_Z \phi_{YZ} \right] + \\
&\delta^2 \phi_Z \left[\delta^2 \phi_X \phi_{XZ} + \phi_{XZ} + \phi_Y \phi_{YZ} + \phi_Z \phi_{ZZ} \right] .
\end{aligned} \tag{4.22}$$

Eliminating terms with $\delta^2, \delta^3, \cdots$ and assuming $S < \delta$, we get [33]:

$$\phi_{YY} + \phi_{ZZ} = 0 \tag{4.23}$$

which represents the Laplace Equation in the transverse $(Y - Z)$ plane. Since the store angle of attack is small by assumption (M1), we can assume that the potential is governed

by two dimensional Laplace Equation in the cross-flow plane perpendicular to the store axis. Thus, the problem of a slender axi-symmetric body that falls through an inviscid cross-flow (while neglecting gravity) is reduced to solving the Laplace Equation of the perturbation velocity potential in the store cross-section plane.

After solving for the velocity potential, we use Bernoulli's equation to convert ϕ to pressure, then integrate the pressure along the store surface to get normal force and pitching moment on the store. The force and moment expressions are given in Ref. [33]. These expressions are further processed in the current paper to obtain a set of parametric non-linear ordinary differential equations for the store trajectory. We develop the appropriate parametric expressions for the force and moment in three stages: (I) when the store is completely inside the cavity, (II) when the store passes through the shear layer, and (III) when the store is completely outside the cavity.

4.1.4 Force and Moment for Store Inside Cavity

Let the store be released with the conditions $\left(\hat{Y}_0, \hat{\alpha}_0, \hat{V}_0, \hat{\omega}_0\right)$ from within the cavity. The problem of the store drop inside the cavity, which is assumed to be quiet, reduces to the fall of a circle towards the free slip surface in an immovable fluid. The presence of the cavity walls is ignored because the cavity is sufficiently wider and taller than the slender store diameter. In particular, the effect of the front and back wall on the store potential is of $O\left(\frac{4\delta^2\hat{l}_o^2}{\hat{D}_o^2}\right)$, where $\hat{D}_o$ is the width of the cavity, and the effect of the top wall is of $O\left(\frac{\delta^2\hat{l}_o^2}{\hat{H}_o^2}\right)$, where $\hat{H}_o$ is the depth of the cavity.

The problem of a circle falling in an quiescent fluid towards a free surface can be solved using the multipole expansion (Laurent series) technique [31]. The resulting potential function is given in Appendix H and the associated normal force and moment on the store, expressed in a parametric form, are given by:

$$\begin{aligned}
\hat{F} &= \pi\hat{\rho}_\infty\delta\hat{l}_o^3\left(g_0\frac{d\hat{V}_c}{d\hat{t}}\hat{l}_o + g_1\frac{d\hat{\omega}}{d\hat{t}}\hat{l}_o^2 + g_2\hat{\omega}^2\hat{l}_o^2 + g_4\hat{V}_c^2 + g_9\hat{\omega}\hat{l}_o\hat{V}_c\right) \\
\hat{M} &= \pi\hat{\rho}_\infty\delta\hat{l}_o^4\left(h_0\frac{d\hat{V}_c}{d\hat{t}}\hat{l}_o + h_1\frac{d\hat{\omega}}{d\hat{t}}\hat{l}_o^2 + h_2\hat{\omega}^2\hat{l}_o^2 + h_4\hat{V}_c^2 + h_9\hat{\omega}\hat{l}_o\hat{V}_c\right)
\end{aligned} \tag{4.24}$$

where $\hat{\rho}_\infty$ is the external free stream density, g_0, g_1, g_4, g_9 and h_0, h_1, h_4, h_9 are non-dimensional factors that depend on the store geometry, position and orientation relative to the shear

layer and are given in Appendix H. Also, V_c is the store linear velocity (positive upwards) and ω is the rotational velocity (positive nose-up). The most dominant term in the above equation is the store velocity (linear or angular velocity term). Assuming linear velocity term to be dominant, the vertical motion of the store inside the cavity is given by:

$$\hat{m}_s \frac{d\hat{V}_c}{d\hat{t}} = \pi \hat{\rho}_\infty \delta \hat{l}_o^3 g_4 \hat{V}_c^2 - \hat{m}_s \hat{g}, \frac{d\hat{Y}_c}{d\hat{t}} = \hat{V}_c,$$
$$\hat{I}_s \frac{d\hat{\omega}}{d\hat{t}} = \pi \hat{\rho}_\infty \delta \hat{l}_o^4 h_4 \hat{V}_c^2, \frac{d\hat{\alpha}}{d\hat{t}} = \hat{\omega}, \tag{4.25}$$

where $\hat{m}_s$ and $\hat{I}_s$ are the mass and moment of inertia of the store about its axis, $\hat{g}$ is gravity, Y_c is the store c.g. position relative to the shear layer line (positive upwards) and $\hat{\alpha}$ is the angle between the store axis and the external free stream direction (positive clockwise). The store state (position, orientation and velocity) is illustrated in Figure 4-2. Also the factor g_4 typically does not vary significantly when the store is inside the cavity.

The following velocity expression can be obtained from this equation:

$$\begin{aligned} \hat{V}_c &= -\sqrt{\frac{\hat{g}}{A}} \tanh\left(t\sqrt{\hat{g}A} + \frac{1}{2} \log \frac{\sqrt{\frac{\hat{g}}{A}} - \hat{V}_0}{\sqrt{\frac{\hat{g}}{A}} + \hat{V}_0} \right), g_4 > 0 \\ &= -\sqrt{\frac{\hat{g}}{A}} \tan\left(t\sqrt{\hat{g}A} - \arctan \frac{\hat{V}_0}{\sqrt{\frac{\hat{g}}{A}}} \right), g_4 < 0 \end{aligned}$$

where $A = \frac{\hat{\rho}_\infty \delta \hat{l}_o^3 g_4}{\hat{m}_s}$ and $\hat{V}_0$ is the store vertical velocity at drop point. Figure 4-3 illustrates the velocity of store while inside cavity for various drop cases.

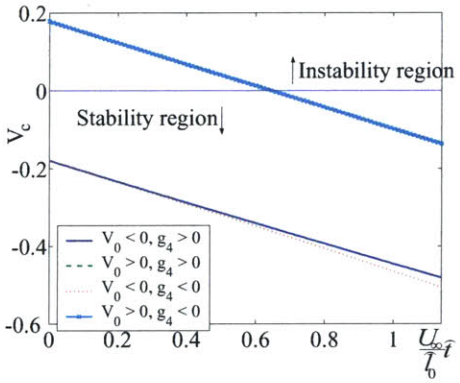

Figure 4-3: Velocity of store while inside cavity for various drop cases, with $V_c = \frac{\hat{V}_c}{\delta U_\infty}$. The values of parameters used: $\left|\hat{V}_0\right| = 0.18\delta U_\infty, |g_4| = 0.75$.

It is clear that irrespective of the signs of g_4 and V_0, V_c eventually becomes negative inside the cavity, although if $V_0 > 0$, then V_c remains positive for a certain time duration before turning negative. In other words, the inner volume of the cavity has a stabilizing influence on the store, in that it eventually falls towards the shear layer irrespective of V_0. Also typically $h_4 > 0$ so that rotational velocity and angle of attack increase monotonically.

If $\hat{\omega}$ terms in force are significant, a similar analysis can be done to find the drop conditions (i.e., $\hat{V}_0$ and $\hat{\omega}_0$) that would ensure that the store falls towards the shear layer. For example, if the store is dropped with very high $\hat{\omega}_0$ and low $\hat{V}_0$, the store may pitch up and move towards the cavity roof instead of the shear layer.

4.1.5 Force and Moment When Store Crosses Shear Layer

When the store crosses the shear layer, a part of the store falls inside the cavity with no flow, another part falls outside the flow facing a uniform flow U_∞ and the remaining part faces both flows. This is illustrated in Figure 4-4.

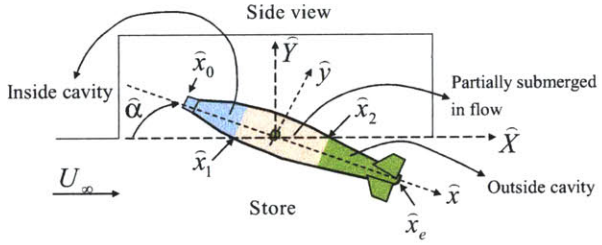

Figure 4-4: Reference frame used when the store crosses the shear layer slip surface.

Because of the linearity property of solutions of the Laplace Equation, the problem of the store crossing the shear layer can be reduced to three unit problems: one is a circle that falls towards the slip surface in an immovable fluid (problem (I)), another one is a circle partially immersed in a flow (problem (II)), and the last one is a circle that falls from a free surface into a uniform stream (problem (III)). Problem (I) has been solved in the previous section and problem (III) is solved in the following section. Problem (II) can be solved using conformal transformation [31] of the store region partially immersed in external cross-flow to an 'equivalent' flat plate in the complex plane $\sigma = \xi + i\eta$ as illustrated in Figure 4-5. The mapping of the store region submerged in the external cross-flow is given by [31]:

$$\zeta = f(\sigma, X, t) = c\frac{R^n + 1}{R^n - 1}, n = \frac{\pi - \beta}{\pi}, R = \frac{\sigma + b}{\sigma - b}, b = \frac{c}{n} \tag{4.26}$$

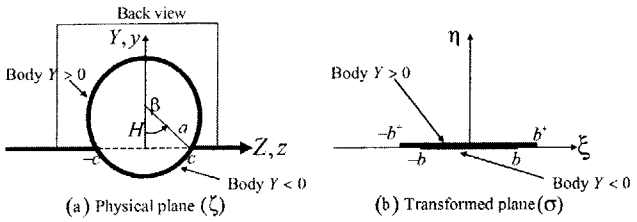

Figure 4-5: Conformal transformation required to solve for the velocity potential associated with the store region partially immersed in the external flow.

while the mapping for the store region inside the cavity is:

$$\zeta^+ = f^+(\sigma, X, t) = c\frac{R_+^m + 1}{R_+^m - 1}, m = \frac{\beta}{\pi}, R_+ = \frac{\sigma + b^+}{\sigma - b^+}, b^+ = \frac{c}{m} \tag{4.27}$$

To verify the transformation of the store cross-section into a flat plate, we solve Eqn. (4.26) to obtain the transformed (Y, Z) from (ξ, η). The result is:

$$Y(\xi)|_{\eta=0} = -2c\frac{Q^n}{D}\sin\pi n,\ Z(\xi)|_{\eta=0} = c\frac{Q^{2n}-1}{D}, D = Q^{2n} - 2Q^n\cos\pi in + 1, Q = \frac{\xi + b}{\xi - b}. \tag{4.28}$$

It can be shown that:

$$\left(Y(\xi)|_{\eta=0} - \frac{c}{\tan\pi(1-n)}\right)^2 + Z(\xi)|_{\eta=0}^2 = \left(\frac{c}{\sin\pi(1-n)}\right)^2 \tag{4.29}$$

thus showing that the transformed (Y, Z) form an arc from the flat plate $(\xi, \eta = 0)$. This type of transformation has been used for the flow over a log given in Milne-Thomson [38] for slip line boundaries. Also for $n > \frac{1}{2}$, the flow velocities have a singularity of type $(\sigma^2 - b^2)^{\frac{1}{2}-n}$ at the points where the free surface intersects the body. Since this singularity is integrable, $\hat{F}$ and $\hat{M}$ are not singular.

After the transformation to a flat plate, $\hat{F}$ and $\hat{M}$ due to the store partially immersed in the external flow are computed. To this, the contributions of the store portion completely inside and completely outside the cavity are added. Before we can predict the force and moment as the store crosses the shear layer, let us study problem (III) when the store is outside the cavity.

4.1.6 Force and Moment for Store Outside Cavity

The problem of store moving outside the cavity reduces to a circle falling in a free stream. If the store is far from cavity, then the stream can be considered unbounded (the no-cavity model – Appendix J). If the cavity depth is small, then the stream can be considered to be bounded by a rigid wall (the zero-depth-cavity model – Appendix K). Also if the store is close to the shear layer, then the stream can be considered to be bounded by a free surface (the near-cavity model – Appendix L). All these cases can be solved using the multipole (Laurent series) expansion technique [31]. Finally the presence of shear layer structures is to be taken into account if the thickness of the shear layer is not small (Appendix M).

The steps for solving the problems for velocity potential and converting the potential to force and moment on the store is given in Ref. [31]. Here we use the same steps to obtain $\hat{F}$ and $\hat{M}$, the expressions of which are further manipulated so that they are represented in a parametric form:

$$\begin{aligned}\hat{F} = \pi\hat{\rho}_\infty\delta\hat{l}_o^3\Bigg(g_0\frac{d\hat{V}_c}{d\hat{t}}\hat{l}_o + g_1\frac{d\hat{\omega}}{d\hat{t}}\hat{l}_o^2 + g_2\hat{\omega}^2\hat{l}_o^2 + U_\infty^2 g_3\hat{\alpha}^2 + g_4\hat{V}_c^2 + U_\infty\delta g_5\hat{\omega}\hat{l}_o + U_\infty^2\delta g_6\hat{\alpha} + \\ U_\infty\delta g_7\hat{V}_c + U_\infty g_8\hat{\alpha}\hat{\omega}\hat{l}_o + g_9\hat{\omega}\hat{l}_o\hat{V}_c + U_\infty g_{10}\hat{\alpha}\hat{V}_c + \delta^2U_\infty^2 g_{11}\Bigg) \\ \hat{M} = \pi\hat{\rho}_\infty\delta\hat{l}_o^4\Bigg(h_0\frac{d\hat{V}_c}{d\hat{t}}\hat{l}_o + h_1\frac{d\hat{\omega}}{d\hat{t}}\hat{l}_o^2 + h_2\hat{\omega}^2\hat{l}_o^2 + U_\infty^2 h_3\hat{\alpha}^2 + h_4\hat{V}_c^2 + U_\infty\delta h_5\hat{\omega}\hat{l}_o + U_\infty^2\delta h_6\hat{\alpha} + \\ U_\infty\delta h_7\hat{V}_c + U_\infty h_8\hat{\alpha}\hat{\omega}\hat{l}_o + h_9\hat{\omega}\hat{l}_o\hat{V}_c + U_\infty h_{10}\hat{\alpha}\hat{V}_c + \delta^2U_\infty^2 h_{11}\Bigg)\end{aligned} \tag{4.30}$$

where $g_0, \cdots, g_{11}, h_0, \cdots, h_{11}$ depend on the model used (i.e., the no-cavity, zero-depth-cavity or near-cavity model or the model with wavy structures) and are given in Appendices J-L. It may be noted that this equation also gives the general expressions for $\hat{F}$ and $\hat{M}$ when the store crosses the shear layer, with the corresponding $g_0, \cdots, g_{11}, h_0, \cdots, h_{11}$ being outlined in Appendix I.

We cannot use the models developed above to obtain an insight into the release trajectory when the store is outside the cavity, due to their complexity. To address this issue, we now outline a simple model that captures the dominant physics of the problem.

Because of the high speed of the external flow and because the store is inclined to the flow, the component of the external flow normal to the store is dominant compared to the store velocity. Hence the dominant terms in $\hat{F}$ and $\hat{M}$, when the store is external to the

cavity, contain $\hat{\alpha}$, and is of the form:

$$\hat{F} = \pi\hat{\rho}_\infty U_\infty^2 \delta \hat{l}_o^3 \left(g_3\hat{\alpha}^2 + \delta g_6 \hat{\alpha}\right),$$
$$\hat{M} = \pi\hat{\rho}_\infty U_\infty^2 \delta \hat{l}_o^4 \left(h_3\hat{\alpha}^2 + \delta h_6 \hat{\alpha}\right). \tag{4.31}$$

The second order dependence of $\hat{F}$ and $\hat{M}$ on $\hat{\alpha}$ makes it difficult to analyze the dominant trend in the store motion outside the cavity. Hence, we linearize Eqn. (4.31) about $\hat{\alpha} = 0$ to get:

$$\hat{F} = \pi\delta^2 \hat{l}_o^3 \beta f(\hat{\alpha}),$$
$$\hat{M} = \pi\delta^2 \hat{l}_o^4 \beta f_m(\hat{\alpha}),$$
$$\beta = \hat{\rho}_\infty U_\infty^2,$$
$$f(\hat{\alpha}) = g_6\hat{\alpha},$$
$$f_m(\hat{\alpha}) = h_6\hat{\alpha}, \tag{4.32}$$

It should be mentioned here that the error incurred in using assumption (M1) to develop the above expression for $\hat{F}$ is less than 10% for $\hat{\alpha} < 40°$. Using Eqn. (4.32) and following Eqn. (4.25), the governing equation for the store trajectory outside the cavity becomes:

$$\hat{m}_s \frac{d\hat{V}_c}{d\hat{t}} = \pi\hat{\rho}_\infty U_\infty^2 \delta^2 \hat{l}_o^3 g_6 \hat{\alpha} - \hat{m}_s \hat{g}, \frac{d\hat{Y}_c}{d\hat{t}} = \hat{V}_c,$$
$$\hat{I}_s \frac{d\hat{\omega}}{d\hat{t}} = \pi\hat{\rho}_\infty U_\infty^2 \delta^2 \hat{l}_o^4 h_6 \hat{\alpha}, \frac{d\hat{\alpha}}{d\hat{t}} = \hat{\omega}. \tag{4.33}$$

After the store exits the shear layer, let its state be denoted by $\left(\hat{Y}_1, \hat{\alpha}_1, \hat{V}_1, \hat{\omega}_1\right)$. When $\hat{\alpha}_1$ is large, since $g_6 > 0$ in Eqn. (4.33), the linear dependence of $f(\hat{\alpha})$ on $\hat{\alpha}$ results in large $\hat{F}$. This increases the likelihood of $\hat{F}$ to overcome gravity and the store to return back towards the cavity. This is further demonstrated from the expression for $\hat{V}_c$ which is obtained by solving Eqn. (4.33) with $\hat{V}_1$ as the initial condition. As a result we get:

$$\hat{V}_c = B\left(-\hat{\omega}_1 \cos\Lambda\hat{t} + \Lambda\hat{\alpha}_1 \sin\Lambda\hat{t}\right) - \hat{g}\hat{t} + B\hat{\omega}_1 + \hat{V}_1 \tag{4.34}$$

where $\Lambda^2 = \frac{\pi\hat{\rho}_\infty U_\infty^2 \delta^2 \hat{l}_o^4 |h_6|}{\hat{I}_s}$, $B = \frac{\hat{I}_s g_6}{\hat{m}_s \hat{l}_o h_6}$. The linear velocity expression consists of a sinusoidal term, a linear term and an offset. From an order of magnitude analysis, it can be shown

that the offset term is the dominant one. For a given $\left(\hat{Y}_1, \hat{\alpha}_1\right)$, if

$$\frac{\hat{\omega}_1}{\hat{V}_1} > -\frac{1}{B}, \tag{4.35}$$

then $\hat{V}_c$ becomes positive when $\frac{1}{\Lambda}\arccos\left(1+\frac{\hat{V}_1}{B\hat{\omega}_1}\right) < \hat{t} < \frac{2\pi}{\Lambda} - \frac{1}{\Lambda}\arccos\left(1+\frac{\hat{V}_1}{B\hat{\omega}_1}\right)$. The implication is that over this time interval, the store returns towards the cavity. The above discussions indicate that the store dynamics outside the cavity can be characterized by a stable region with linear boundary, where a stable region is defined as the set of $\left(\hat{Y}_1, \hat{\alpha}_1, \hat{V}_1, \hat{\omega}_1\right)$ such that the store exhibits a safe drop.

The stability analysis performed so far, particularly Eqn. (4.35), is based on the simplified dynamics of the store in Eqn. (4.33). To compare this stability analysis with the predictions of the more complex models, we evaluate the four models (i.e., the no-cavity, zero-depth-cavity, near-cavity models and the model with wavy structures) and determine the conditions $\left(\hat{V}_1, \hat{\omega}_1\right)$ that result in an unsafe store departure for a particular $\left(\hat{Y}_1, \hat{\alpha}_1\right)$. The safe and unsafe drop conditions for the four models are shown in Figure 4-6, together with the stability boundary predicted by the dominant order model given in Eqn. (4.35). For the dominant order model, the values of g_6 and h_6 are obtained from Eqn. (L.2) (corresponding to the near-cavity model), after taking their mean over the time duration in which the store is present outside the cavity. Figure 4-6 illustrates that all the models predict a stability region with a linear boundary having different slopes. The varying slopes are due to the fact that the models capture the store release mechanism under different resolutions. It should also be noted that the near-cavity model predicts the most conservative stability region. Therefore, out of the five models, the near-cavity one is used for optimizing the control input for successful store release in section 4.3.

4.2 Analysis of the Complete Store Drop

The low order model developed in section 4.1 is now used to analyze the store trajectory as it is dropped from inside the cavity to the point where it has either exhibited successful drop or it starts to return back into the cavity. This analysis is performed for two cases: (I) when microjets are off, and (II) when the microjets are switched on.

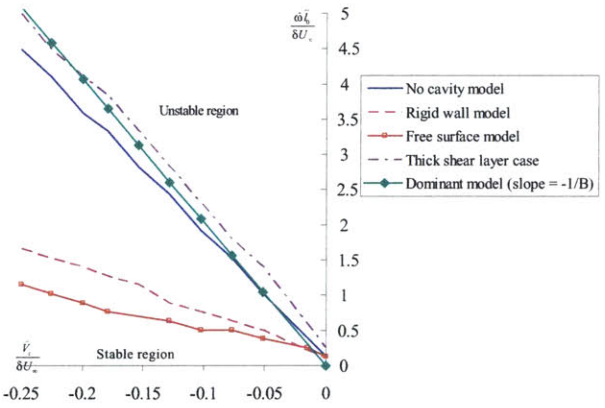

Figure 4-6: Stability region predicted by the five outside-cavity models in the no-control case. The initial conditions for the models are: $Y_1 = \frac{\hat{Y}_1}{\delta \hat{l}_o} = -1.63$ and $\alpha_1 = \frac{\hat{\alpha}_1}{\delta} = 0.01$ with $V_1 = \frac{\hat{V}_1}{\delta U_\infty}$ and $\omega_1 = \frac{\hat{\omega}_1 \hat{l}_o}{\delta U_\infty}$ shown in the above plot. The uncertainty in the stability boundaries are as follows: $\Delta V_1 = \pm 0.005, \Delta \omega_1 = \pm 0.125$. The cross-flow Mach number is 2.46, Reynolds number based on store length is 4.9 million, cavity aspect ratio is 5 and store length is half of cavity length.

4.2.1 No microjets present

Let the store be dropped from inside the cavity with the conditions $\left(\hat{Y}_0, \hat{\alpha}_0, \hat{V}_0, \hat{\omega}_0\right)$, with $\hat{\alpha}_0$ positive and small, $\hat{V}_0 < 0$ and $\hat{\omega}_0 > 0$ but not large enough so that the store hits the cavity roof immediately. It follows from Section 4.1.4 that $\hat{\omega}$, $\hat{\alpha}$ and $\left|\hat{V}_c\right|$ inside the cavity increases monotonically by the time it reaches the shear layer. Also, from Eqns. (4.25) and (4.32), it follows that when the store crosses the shear layer, the portion of the store inside the cavity experiences a normal force proportional to $\hat{V}_c{}^2$ while the portion outside experiences a force proportional to $f(\hat{\alpha})$. The latter is dominant because of the high external flow speed. Now from Eqn. (4.32) (with $h_6 < 0$) and from the fact that the tail side is first exposed to the external stream when the store exits the cavity, it follows that there is an increase in $\hat{M}$ in the nose-down (negative) direction and a consequent decrease in $\hat{\omega}$. Despite this, if the store is released with a large $\hat{\omega}_0$ when compared to $\hat{V}_0$, then $\hat{\omega}_1$ is large when the store exits the cavity and Eqn. (4.35) is satisfied, thus implying an unsuccessful drop. It also follows that if the store is released with a small $\hat{\omega}_0$, then $\hat{\omega}_1$ is small and Eqn. (4.35) is not satisfied. In that case, the store exhibits a clean departure. In summary, if the store is dropped with a small $\hat{\omega}_0$ when compared to $\hat{V}_0$, the store exhibits a safe departure from inside the cavity.

It is instructive to compare the analysis performed here with that done for subsonic and transonic flows [30, 31]. Because of the high speed of supersonic flow, the dominant term in

$\hat{F}$ and $\hat{M}$ are dependent on $\hat{\alpha}$ when the store is external to the cavity. Hence it is relatively easy to analyze its stability. On the other hand, in the subsonic and transonic cases, the terms containing $\hat{V}_c, \hat{\omega}$ and their time derivatives are equally important and hence it is more difficult to analyze the trend in store trajectory outside the cavity. However, it should be noted that unsafe store departure depends on the nature of the drop conditions in all flow cases; in the subsonic and transonic cases, unsafe departure occurs if either $\hat{V}_0$ is small or $\hat{\alpha}_0$ is large whereas in the supersonic case, we note that unsuccessful departure occurs if $\left|\frac{\hat{\omega}_1}{\hat{V}_1}\right|$ is large.

4.2.2 Microjets Present

Next we analyze the store drop phenomenon when microjets are switched on. The following dominant effects are observed due to the introduction of microjets: (i) flow deceleration $\left(\frac{\hat{U}_{\infty,2}}{\hat{U}_{\infty,1}} < 1\right)$, (ii) flow compression $\left(\frac{\hat{\rho}_{\infty,2}}{\hat{\rho}_{\infty,1}} > 1\right)$, (iii) flow turning (away from the cavity by an angle θ), and (iv) introduction of plane shock waves at the cavity leading edge. Figure 4-1 gives a pictorial description of these effects.

Since the store is released in the middle of the cavity, it is not expected to intersect the plane shock line; therefore effect (iv) is not directly considered any further in the discussions below. However, effects (i)-(iii) influence $\hat{F}$ and $\hat{M}$ on the store and their magnitudes are determined by the ratio of microjet-cross-flow momentum ratio C_μ defined below[1]:

$$C_\mu = \frac{\frac{1}{4}\left(\rho A U^2 N\right)_\mu}{\frac{1}{2}\left(\rho U^2\right)_\infty \left(\hat{D}_o \delta_{BL}\right)}. \tag{4.36}$$

The dependence of effects (i)-(iii) on C_μ was experimentally determined in the Florida State University (FSU) setup and is explained in Appendix 1. The main idea is twofold: (a) the flow visualization studies done using the FSU cavity setup established the C_μ-dependence of the shock orientation angle ψ and θ (Figure 4-1), and (b) the effects (i)-(iii) were quantified using results of (a) and plane shock theory [36]. The resulting dependence of (i)-(iii) on C_μ is given in Figure 4-7. It should be noted that all these effects are introduced when the

[1] The subscript μ refers to the mean microjet properties at the microjet nozzle exit, subscript ∞ refers to the mean undisturbed external flow properties, ρ and U are the mean dimensional density and flow speed, A is the microjet cross-section area, N is the number of microjets, $\hat{D}_o$ is the cavity width as shown in Figure N-1 (in Appendix N) and δ_{BL} is the dimensional boundary layer thickness at the cavity leading edge. Also, $\left(\rho U^2\right)_\mu$ depends on the pressure at which the microjets are activated, thereby establishing a direct relationship between the microjet pressure and C_μ.

store exits the cavity, whereas they do not affect the mean flow field inside the cavity.

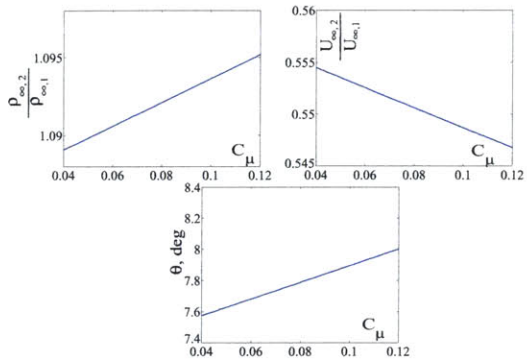

Figure 4-7: Variation of external flow properties with C_μ due to application of microjets.

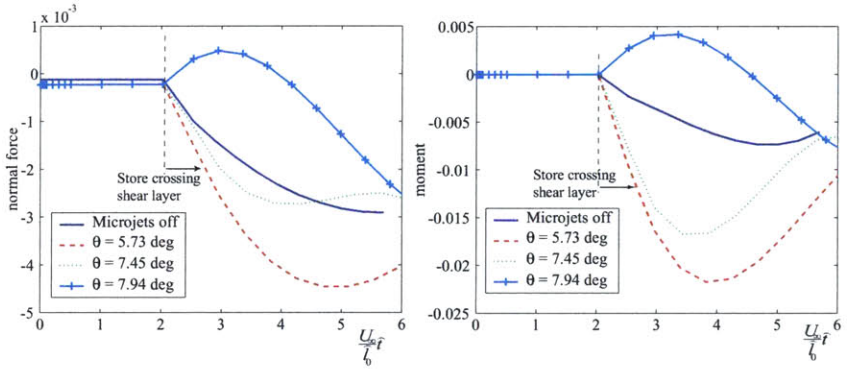

Figure 4-8: Model-predicted $\hat{F}$ and $\hat{M}$ evolution with time for different θ when the store passes through the shear layer. The other external flow parameters used are: $\frac{\hat{\rho}_{\infty,2}}{\hat{\rho}_{\infty,1}} = 1.818$, and $\frac{\hat{U}_{\infty,2}}{\hat{U}_{\infty,1}} = 0.915$. Also, the cross-flow uncontrolled Mach number is 2.46, Reynolds number based on store length is 4.9 million, cavity aspect ratio is 5 and store length is half of cavity length. A smoothing function is used to remove noise in the force and moment predictions of the model.

Now $\hat{F}$ and $\hat{M}$ have been derived and analyzed in Chapter 4 for general values of $\hat{\rho}_\infty$ and U_∞. In order to study the effect of microjets, we vary C_μ, which in turn introduces the changes (i)-(iii). This in turn changes $\hat{F}$ and $\hat{M}$ as outlined in Chapter 4. An important point to note here is the change in $\hat{F}$ and $\hat{M}$ as a function of θ. In Figure 4-8, the responses of $\hat{F}$ and $\hat{M}$ as a function of time and as θ is varied, is illustrated. It is clear from the figure that a dramatic change in the slope of $\hat{M}$ occurs when θ is increased. In particular, $\hat{M}$ becomes negative when θ is below a certain value and positive for higher value of θ, which essentially indicates onset of the store returning towards the cavity, as explained below. A similar trend is observed for $\hat{F}$. It should also be noted that the variations of $\hat{F}$ and $\hat{M}$

with effects (i) and (ii) are more gradual.

To further analyze the dependence of $\hat{M}$ on θ, we consider the general expression for $\hat{M}$ given by Eqn. (4.30) when the store crosses the shear layer. Keeping the dominant terms in the equation and with microjets on, we have:

$$\hat{M} = \pi\hat{\rho}_\infty\delta\hat{l}_o^4\left[\underbrace{h_4\hat{V}_c^2}_{I}+\underbrace{h_9\hat{\omega}\hat{l}_o\hat{V}_c}_{II}+\underbrace{U_\infty^2 h_3\left(\hat{\alpha}-\theta\right)^2}_{III}+\underbrace{U_\infty^2\delta h_6\left(\hat{\alpha}-\theta\right)}_{IV}\right]. \tag{4.37}$$

These terms are plotted in Figure 4-9. It is clear that when the store touches the shear layer

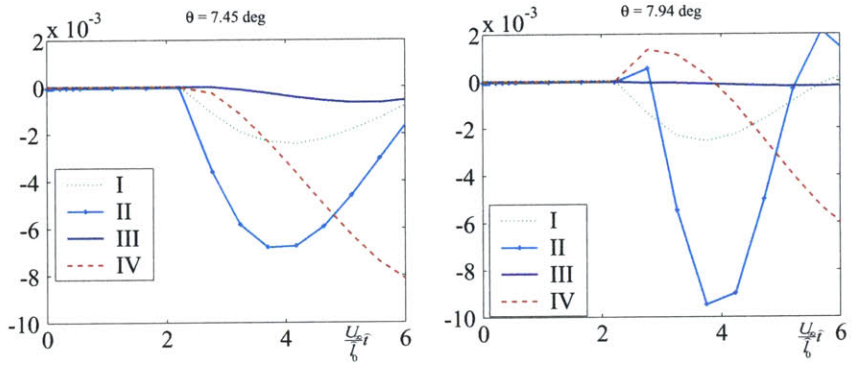

Figure 4-9: Different components of the model-predicted $\hat{M}$ (from Eqn. (4.37)) and their evolution with time for different θ when the store passes through the shear layer. The other external flow parameters used are: $\frac{\hat{\rho}_{\infty,2}}{\hat{\rho}_{\infty,1}} = 1.818$, and $\frac{\hat{U}_{\infty,2}}{\hat{U}_{\infty,1}} = 0.915$. Also, the cross-flow uncontrolled Mach number is 2.46, Reynolds number based on store length is 4.9 million, cavity aspect ratio is 5 and store length is half of cavity length. A smoothing function is used to remove noise in the moment prediction of the model.

from inside the cavity, the dominant effect is the introduction of terms III and IV in $\hat{M}$, both of which depend on $\hat{\alpha}-\theta$. Because of this feature, a drastic change in $\hat{M}$ is observed at the instant when the store hits the shear layer. At this point, if $\hat{\alpha}$ is greater than θ, there is a negative pitching moment because the store tail is exposed to the external flow. However, if θ is increased by introducing higher microjet pressures such that $\hat{\alpha}$ is less than θ at this point, then there is a positive pitching moment.

It follows that when the microjets are switched on such that θ is less than a certain value, $\hat{M}$ increases in the negative direction and causes $\hat{\omega}$ to decrease when the store crosses the shear layer. At this point, Eqn. (4.35) is not satisfied which implies that the store exhibits a safe drop. When microjet pressures are increased, there is a further increase in θ. If θ exceeds the limiting value, $\hat{M}$ increases positively and corresponding $\hat{\omega}$ increases when

the store crosses the shear layer. Increase in $\hat{\omega}_1$ causes Eqn. (4.35) to be satisfied leading to an unsuccessful drop. Also this trend is independent of $\hat{\omega}_0$. The variation of the store state as it crosses the shear layer in the absence and presence of microjets is given in Figure 4-10.

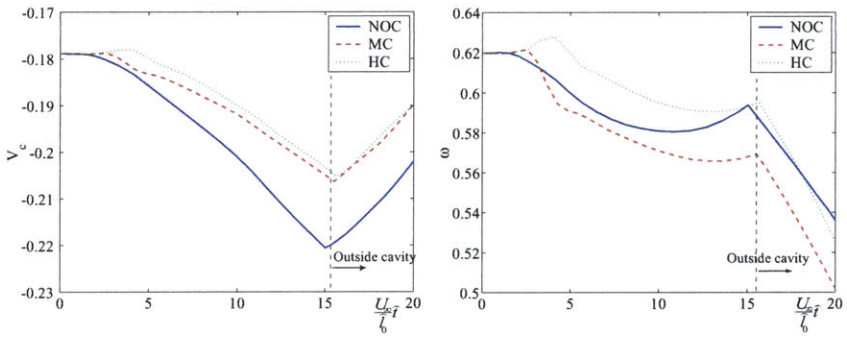

Figure 4-10: $\hat{V}_c$ and $\hat{\omega}$ evolution with time for different control inputs when the store passes through the shear layer. The control inputs are specified in Table 4.1. Also, the cross-flow uncontrolled Mach number is 2.46, Reynolds number based on store length is 4.9 million, cavity aspect ratio is 5 and store length is half of cavity length.

In summary, the introduction of microjets can ensure safe departure for any $\hat{\omega}_0$ as long as θ is less than a certain value. However, for θ greater than this limit, which occurs for large microjet pressures, the store tends to return back to the cavity.

4.3 Experimental Validation of Store Drop Model

In this section, we compare the low order model predictions with results from experiments performed under the DARPA-funded HIFEX Program [2, 3, 4].

4.3.1 Experimental Details

A series of free drops of a slender axi-symmetric store from a generic sub-scale weapons bay cavity was conducted under the HIFEX Program at various supersonic cross-flow Mach numbers [3, 4]. For brevity, this thesis considers the experiments that were performed at two Mach numbers, 2.0 and 2.46. In addition, the bay model has the aspect ratio $\frac{\hat{L}_o}{\hat{H}_o} = 5$ and $\frac{\hat{L}_o}{\hat{D}_o} = 5$, with $\hat{H}_o$ being the depth and $\hat{D}_o$ the width of cavity. The Reynolds number of the flow based on the store length is approximately 4.9 million and the speed of flow at Mach 2.46 is 579 m/s. The store is half the cavity length, its associated δ is 0.0615, the ratio of the free stream density to the store density is 1.1869e-4, and the store geometry is

illustrated in Figure 4-11. Moreover, the flow-injection actuator consists of two rows of sonic

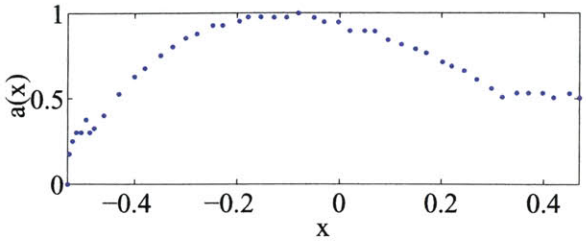

Figure 4-11: Radius profile of the store. Here $x = \frac{\hat{x}}{\hat{l}_o}$ and $a = \frac{\hat{a}}{\delta \hat{l}_o}$. Also $x = 0$ corresponds to the store c. g.

microjets along the leading edge and two rows near the upstream end of the cavity, situated about $L/8$ distance from the leading edge. Here L is the cavity length, the microjets are of 400 μm in diameter and each row consists of 50 microjets.

The store was dropped from $Y_c = \frac{\hat{Y}_c}{\delta \hat{l}_o} = 1.3$ inside the cavity with nearly zero angle of attack and the store trajectory outside the cavity was recorded in high speed video [3, 4]. The drop tests were conducted using three different control inputs: no control (NOC), microjet-control on (MC), and high-microjet-pressure-control(HC). Table 4.1 shows the changes in the external flow for the three control inputs and the store drop results are discussed below.

Item	NOC	MC	HC	MC-NOC, %	HC-MC, %
$\frac{\hat{\rho}_{\infty,2}}{\hat{\rho}_{\infty,1}}$	1.000	1.818	1.826	81.8	0.4
$\frac{\hat{U}_{\infty,2}}{\hat{U}_{\infty,1}}$	1.000	0.915	0.914	-8.5	-0.1
$\frac{\hat{\rho}_{\infty,2}\hat{U}^2_{\infty,2}}{\hat{\rho}_{\infty,1}\hat{U}^2_{\infty,1}}$	1.000	1.523	1.524	52.3	0.1
θ, deg	0	7.827	7.947	–	1.5

Table 4.1: Changes in external flow properties with control. Three control inputs are considered: no control(NOC), microjet-control on(MC) and high-microjet-pressure-control(HC). MC refers to 100-250 psig microjet pressure and HC refers to 200-250 psig microjet pressure. The first number here refers to the rows of microjets closest to the leading edge and the second number to the rows at the upstream end of the cavity. Also, the cross-flow uncontrolled Mach number is 2.46, Reynolds number based on store length is 4.9 million, cavity aspect ratio is 5 and store length is half of cavity length.

4.3.2 Comparison with the Model

As mentioned in Section 4.1.6, we have four models (i.e., the no-cavity, zero-depth-cavity, near-cavity models and the model with wavy structures) to describe the trajectory outside the cavity. To choose the appropriate one, we varied the initial conditions $\left(\hat{V}_1, \hat{\omega}_1\right)$ keeping

$\left(\hat{Y}_1, \hat{\alpha}_1\right)$ fixed as a starting point and performed stability analysis using all the models, as shown in Figure 4-6. MATLAB's *ode45.m* was used to solve for the store governing equations in the simulations. From these studies, we identified that the near-cavity model provided the most conservative stability region for the store, and was the model of choice for subsequent model simulations.

Next we use a combination of the inside-cavity model, the model of the store passing through shear layer, and the near-cavity model to obtain the complete trajectory after the store is released from inside the cavity. Using this tool, we predict the store release trajectory in the NOC case and then consider two specific experiments in the MC and HC cases, where the corresponding flow deceleration, flow compression, and flow turning angle are calculated as outlined in Section 3.2, and the resulting store release trajectory under these flow conditions and the same drop conditions as the NOC case are determined. The model-predicted trajectories are compared with experiments in Figure 4-12. The figure

Item	Inside cavity (Point 0)	While exiting cavity (Point 1)
No control(NOC)		
Y_c	1.30	-1.63
α	0.01	8.96
V_c	-0.18	-0.22
ω	0.62	0.59
Microjet-control on(MC)		
Y_c	1.30	-1.63
α	0.01	9.10
V_c	-0.18	-0.22
ω	0.62	0.57
High-microjet-pressure-control(HC)		
Y_c	1.30	-1.63
α	0.01	9.49
V_c	-0.18	-0.22
ω	0.62	0.60

Table 4.2: Initial conditions for the store trajectory analysis used in Figure 4-12. The cross-flow Mach number is 2.46, Reynolds number based on store length is 4.9 million, cavity aspect ratio is 5 and store length is half of cavity length.

shows unsafe store separation for the no-control and high microjet pressure cases and safe separation for the low microjet pressure case. The figure also indicates that the prediction of the experimental store trajectories by the low order models is somewhat poor. However it should be noted that the models correctly predict the variation of $\dot{\hat{Y}}_c$ as the store drops outside the cavity, which in turn implies that the models accurately foretell whether the

drop is successful or not. This validates the models and indicates that the low-order models are suitable for application in the optimization process to identify the best control input for clean store departure.

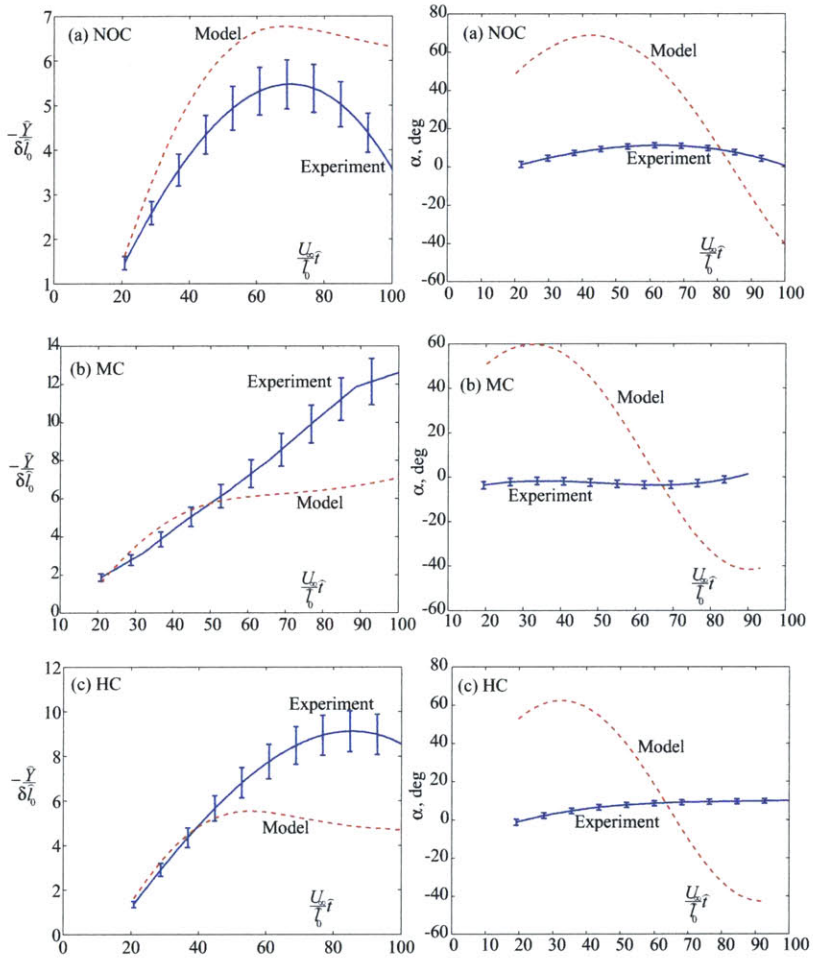

Figure 4-12: Store trajectory prediction (outside the cavity) versus experimental observation for: (a) no control (NOC), (b) microjet-control on (MC) and (c) high-microjet-pressure-control (HC). Also $\left(\hat{t}, \hat{Y}_c\right) = 0$ correspond to the instance when the store just exits the cavity, and increasing $-\hat{Y}_c$ corresponds to the store moving away from the bay. The cross-flow Mach number is 2.46, Reynolds number based on store length is 4.9 million, cavity aspect ratio is 5 and store length is half of cavity length. The model used for trajectory prediction is the near-cavity one, with the initial conditions given in Table 4.2.

To explain the behavior depicted in the figure, we refer to section 3 where we have analyzed the aerodynamic loads on the store for given drop conditions and microjet pressures. The point to note is that the store drop is successful when $\left|\frac{\hat{\omega}_1}{\hat{V}_1}\right|$ is small and unsuccessful otherwise. When microjets are off and the store just exits the cavity, $\hat{\omega}_1$ is large because of

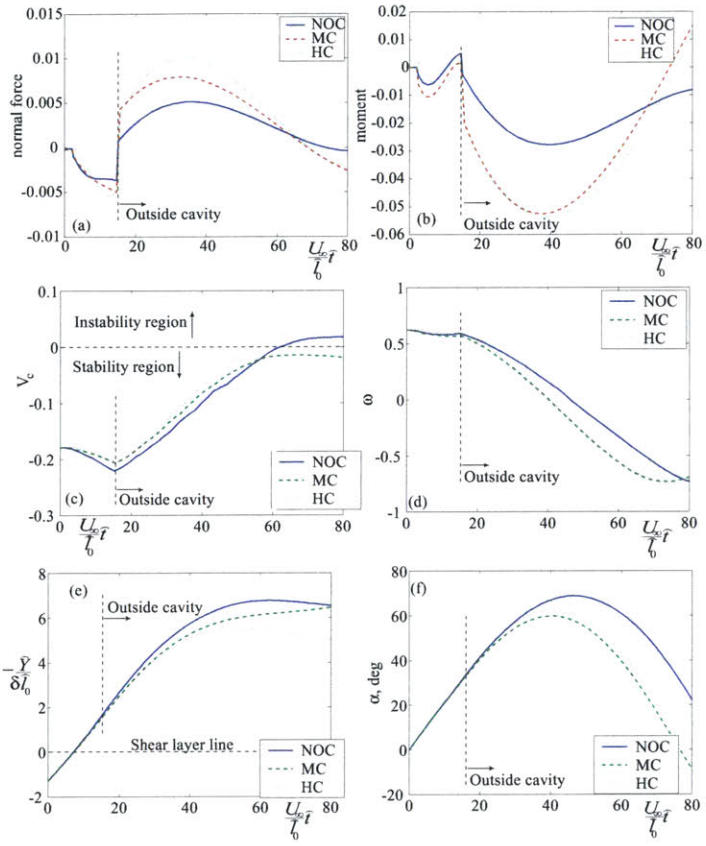

Figure 4-13: Model-predicted normal force, pitching moment and state of the store after being dropped from inside the cavity to when the store either returns back into the cavity or drops successfully in the three control cases: no control(NOC), microjet-control on(MC) and high-microjet-pressure-control(HC). The cross-flow Mach number is 2.46, Reynolds number based on store length is 4.9 million, cavity aspect ratio is 5 and store length is half of cavity length. The model used for outside-cavity trajectory prediction is the near-cavity one, with the initial conditions given in Table 4.2. A smoothing function is used to remove noise from force and moment predictions of the model.

large $\hat{\omega}_0$ at the drop point. The large $\hat{\omega}_1$ in comparison to $\hat{V}_1$ results in the store to exhibit a unsuccessful drop. When microjets are switched on, the external flow is compressed, decelerated and turns away from the cavity with an angle θ. There exists a linear relationship between $\hat{M}$ and $\hat{\alpha}-\theta$ as soon as the store hits the shear layer such that $\hat{M}$ becomes negative when θ is small and positive when θ is large. In the case of MC, θ is small and the result is an increase in $\hat{M}$ in the negative direction and decrease in $\hat{\omega}$, when the store exits the cavity. Low $\hat{\omega}_1$ in comparison to $\hat{V}_1$ results in the store to exhibit a safe drop. When the microjet pressures are increased in the case of HC, θ exceeds the limiting value. The result is that $\hat{M}$ and therefore $\hat{\omega}$ increase positively when the store crosses the shear layer. This

results in large $\hat{\omega}_1$ in comparison to $\hat{V}_1$, thus leading to an unsuccessful drop. Figure 4-13 illustrates the force and moment as well as the state of the store after being dropped from inside the cavity to when the store either returns back into the cavity or drops successfully in the three control cases.

4.4 Optimization of Control Input in Store Drop Setup

Having developed, validated and analyzed models for predicting the store trajectory inside and outside the cavity, the next step is to optimize the control input for a successful store drop. A suitable control parameter that can be optimized is the microjet momentum ratio C_μ as defined in Eqn. (4.36). The optimal input is defined as the minimum value of C_μ which satisfies the user-specified microjet mass flow constraint and which guarantees safe release under a variety of drop conditions. For this purpose, the drop conditions from Table 4.2 were taken as the baseline and a combination of inside-cavity and outside-cavity models were used to determine whether the store exits the cavity successfully for different values of the control input. The procedure was repeated for a different Mach number of external flow that was also tested under the HIFEX Program. The result is shown in Figure 4-14.

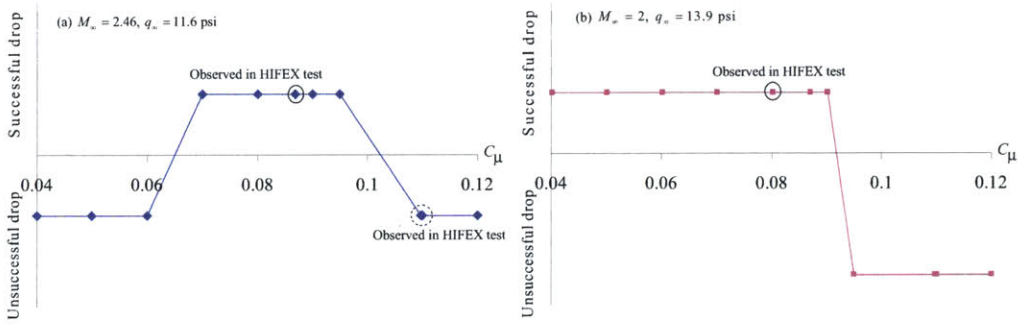

Figure 4-14: Successful/Unsuccessful store drop from cavity versus microjet momentum ratio C_μ. The model used for prediction of the trajectory that lies outside the cavity is the near-cavity one. The cross-flow Mach number is 2.46, Reynolds number based on store length is 4.9 million, cavity aspect ratio is 5 and store length is half of cavity length. The drop conditions for this simulation are: $Y_0 = 1.30, \alpha_0 = 0.01, V_0 = -0.18, \omega_0 = 0.62$ and $Y_1 = -1.63$.

It is clear that a general trend of successful drops at $C_\mu < 0.09$ and failed drops at $C_\mu > 0.09$ are predicted for both the Mach number cases. The successful drop at Mach 2.0 for $C_\mu = 0.08$ is corroborated by a series of store drop experiments performed under the HIFEX Program. It can also be observed that for Mach 2.0, a much smaller value of C_μ

than that used experimentally suffices for ensuring a successful drop whereas for Mach 2.46, failure can occur for small C_μ and the optimal C_μ lies close to where the successful drop experiments were conducted. Once the optimal C_μ is determined, a suitable microjet-based actuator corresponding to this value of C_μ can be designed, which may be based on sonic or converging-diverging nozzles, the latter having the advantage of lower mass flux for the same momentum flux.

Chapter 5

Conclusions

5.1 Cavity Noise Under Supersonic Flow

The supersonic flight community is currently faced with two cavity-under-cross-flow related problems, one being the high noise levels inside the cavity and the other being the return of a store into the cavity after being released from inside. This thesis provides a systematic framework to understand the dominant physics in both problems and to provide solutions for ameliorating the problems. The first portion of this thesis is concerned with high noise in a cavity developed when exposed to an external supersonic cross-flow. The high noise level can potentially be harmful to the structural life of weapon systems inside a weapon bay and to landing gear deployment. The noise is due to a feedback loop between shear layer disturbances at the cavity lip and acoustic waves inside the cavity. A group of researchers under the HIFEX Program[2, 3, 4] has proposed that the most effective mechanism for suppressing noise is by introducing microjets along the cavity leading edge and thereby disrupting the loop. This thesis focuses on the development of a reduced order cavity acoustics model that is used to optimize the control input for cavity noise suppression. The model rigorously explains the role of the microjets in suppressing noise inside the cavity and predicts the amount of noise reduced for a given steady pressure profile under which microjets are fired. The model is developed using an innovative rigorous framework based on the standard aeroacoustic equation with the microjets being introduced through a momentum addition term that acts as an active damper.

The model developed in this thesis was validated by comparing its noise reduction predictions with those obtained from experiments conducted using the FSU cavity at Mach

2.0 flow. The comparison was done at the cavity leading and trailing edges for different microjet pressure profiles and for different numbers of microjets. In all these cases, the model predicted saturation of the noise reduction ability of the actuators at approximately the same microjet pressure as the experiments showed. The reason for the saturation is related to the way the shock structure shape above the microjet nozzle exit changes with increasing microjet pressure. Current knowledge base, however, precludes an explanation for this shock structure behavior. Also the magnitude of noise reduction estimated from the model is a maximum of 2 dB above the observed level at the leading edge, while it is close to the experimental one at the trailing edge within limits of sensor uncertainty for all cases studied in this paper. Finally, the spectral content of the predicted pressure field of the model is not as good as the experimentally observed one, and is not useful for control purposes. So the model can be reliably used to identify the optimal microjet configuration that would be suitable for a given cavity configuration, provided the criteria for optimality is reduction in OASPL and the constraint set is the allowable mass flow of the microjets.

The validated model was then used for deriving an estimate of the optimal control strategy for cavity noise suppression using microjets, both off-line and on-line, with the control input being the spanwise microjet pressure profile. The off-line strategy can be implemented after performing a proper orthogonal decomposition (POD) on the pressure data obtained from a spanwise distribution of sensors present along the cavity walls. For the on-line strategy, a recursive technique of performing POD is required. Since currently available tools preclude the realization of recursive POD, one such technique was invented. This tool is essentially an algorithm for updating the dominant basis of a dynamical system recursively so as to facilitate a on-line control design with bounded projection error. In addition, various simulations have demonstrated that the recursive POD method can be used to compute the dominant basis of a time-invariant system starting from an arbitrary orthonormal basis, potentially resulting in substantial savings in computational resource and time, compared to standard POD techniques.

The model predictions and experiments clearly show that a closed-loop on-line strategy would be unnecessary for the FSU cavity. In fact, an open loop steady uniform control input that satisfies the pre-specified mass flow constraint would suffice. The reason is because the cavity shows early saturation with respect to OASPL reduction with increase in microjet pressure.

5.2 Store Separation from Bay Under Supersonic Flow

Apart from the high cavity noise problem, the problem of unsuccessful store drops from an external bay of an aircraft in flight is another problem of interest for the aircraft industry. Work is currently being done by a group of researchers under the HIFEX Program (see [2, 3, 4] for preliminary results) on eliminating the problem of a slender axi-symmetric body returning back after being dropped from a rectangular cavity under supersonic flow. The proposed solution is an array of microjet-based-transverse-fluid-injection system placed near the leading edge of the cavity. The microjet-based actuator modifies the flow field under the cavity through the associated shock waves and thereby affect the store forces and moments.

The concluding part of this thesis focuses on one aspect of the program, i.e. the development of a low-order model to predict the store trajectory under given drop conditions and control input. The model was used to optimize the control input to ensure a successful store departure using a given setup. The model has three components – one for when the store is inside the cavity, one for when the store passes through the shear layer, and the last one for when the store is completely outside the cavity. The low-order model was developed based on the slender store geometry, thin shear layer at the cavity opening, high Reynolds number external cross-flow, plane shock waves associated with the microjets, no-flow condition inside the cavity and ignorance of cavity acoustic field.

The model was validated using a series of store drop experiments performed under the HIFEX program at Mach 2.0 and 2.46 using a generic sub-scale weapons bay. The trajectory information was obtained from high speed video. Three observations were recorded: (I) the store drop was unsuccessful for microjet-off case, (II) the store dropped safely when microjets were switched on, and (III) the store returned back to the cavity when the microjet pressures were increased. These features were seen in the model as well.

The low-order model developed in this thesis provides the following explanation for the experimental observations. The relevant points to be kept in mind are that: (a) $\hat{F}$ outside the cavity depends linearly on $\hat{\alpha}$ such that the store exits successfully if $\left|\frac{\hat{\omega}}{\hat{V}_c}\right|$ is small at the bay exit, and (b) $\hat{M}$, when the store passes through the shear layer, depends linearly on $\hat{\alpha}$ which changes sign depending on the external flow turning angle θ. The reason for effect (a) is that small $\hat{\omega}$ results in low $\hat{\alpha}$ and therefore $\hat{F}$ does not grow high enough to overcome gravity and the store is ejected from the cavity safely. Because of high speed and no turning

of the external flow in the no-control case, the main effect felt by the store is (a). Thus, if the store is dropped with a large initial $\hat{\omega}$, it leaves the cavity with a large $\hat{\omega}$ in comparison to $\hat{V_c}$. This violates (a) and results in an unsuccessful drop, confirming observation (I). On the other hand, if the drop condition is such that $\hat{\omega}$ is low in comparison to $\hat{V_c}$ when the store exits the cavity, the store will exhibit a safe drop.

With microjets on, the external flow turns away from the cavity. If the turning angle θ is less than a certain value, $\hat{M}$ increases in the negative direction. This results in decrease in $\hat{\omega}$ as the store crosses the shear layer and satisfies effect (a). Thus, the store exhibits a safe drop,confirming observation (II). Higher microjet pressures cause a small increase in θ. If the flow turning angle exceeds the limiting value, $\hat{M}$ and consequently $\hat{\omega}$ increase in the positive direction, when the store crosses the shear layer. This violates (a), leading to an unsuccessful drop and confirming observation (III).

Finally, optimization was performed to identify the best control input that ensures clean store departure for a host of operating conditions. Expressed in terms of the microjet momentum ratio C_μ, the best control input was observed to match that used experimentally for certain flight conditions, and is predicted to be even smaller at other conditions.

5.3 Limitations of the Low Order Models

The low order model developed for the cavity acoustics problem is useful for predicting the overall sound pressure level inside the cavity for a given microjet pressure distribution, although it may not accurately describe the spectral content of the noise inside the cavity. It is also to be noted that the shape of the shock structure at the exit of the microjet nozzle influences the magnitude of the damping term due to the microjets in the governing differential equation for the cavity acoustics. The determination of the shock structure for an arbitrary microjet array of actuators is beyond the scope of this low order model and requires additional work.

The reduced order model developed for the store release problem may not accurately predict the exact drop trajectory of the store, but it reliably foretells the trend in the trajectory (i.e., whether the store drops safely or not) for a given microjet pressure distribution and a given set of drop conditions. However, the model prediction is not reliable when the drop conditions are very close to the stability boundary of the problem. For example, if

the store state is close to the stability boundary depicted in Figure 4-6 within the given uncertainty level, the predictions of the model are not conclusive.

Another point to be noted is that the low order model for store separation is derived under the assumptions (M1)-(M5). Despite this, when assumption (M2) is relaxed, i.e. the shear layer is thick, the model derived in this thesis is valid and it predicts that the stability region for the store release trajectory increases (see Figure 4-6); hence the store trajectory outside the cavity is more stable. In addition, when assumption (M5) is relaxed, i.e. the recirculation region inside the cavity is considered, the model is also valid and it predicts that the store trajectory inside the cavity becomes more stable because of an increase in negative pitching moment that results when the external flow enters the cavity on the side of its trailing edge and hits the store tail. However, the effect of relaxing the assumptions (M1), (M3) and (M4) on the store release trajectory is beyond the scope of this model and needs more work.

Appendix A

Order-of-Magnitude Analysis for the 2-D Uncontrolled Cavity Acoustics Model

In order to realize a reduced-order model for the pressure field inside the uncontrolled cavity, an order-of-magnitude analysis is done to identify the dominant groups in the full governing equation given by (2.4). The different components of Eqn. (2.4) have the following relative orders of magnitude:

$$\begin{aligned}
O\left(\frac{\text{Stiffness1}}{\text{Inertia}}\right) &= \left(\frac{U_\infty}{\omega L}\frac{\bar{c}}{U_\infty}\right)^2\left(1+\frac{L^2}{D^2}\right) \\
O\left(\frac{\text{Damping}}{\text{Inertia}}\right) &= \frac{U_\infty}{\omega L}\left(O\left(\frac{u'}{U_\infty}\right)+O\left(\frac{v'}{U_\infty}\right)\frac{L}{D}\right) \\
O\left(\frac{\text{Stiffness2}}{\text{Inertia}}\right) &= 2\left(\frac{U_\infty}{\omega L}\right)^2\left(O\left(\frac{u'}{U_\infty}\right)+O\left(\frac{v'}{U_\infty}\right)\frac{L}{D}\right)^2 \\
O\left(\frac{\text{Inhomogeneous}}{\text{Inertia}}\right) &= \left(\frac{U_\infty}{\omega L}\right)^3\left(\frac{\bar{c}}{U_\infty}\right)^2 O\left(\frac{U_\infty}{u'}\right)\left(O\left(\frac{u'}{U_\infty}\right)+O\left(\frac{v'}{U_\infty}\right)\frac{L}{D}\right)^2
\end{aligned} \tag{A.1}$$

These expressions are derived under the assumption that the typical acoustic wavelength inside the cavity is of the order of cavity dimension in the desired spatial orientation. The expressions, as derived here, further require the value of ω and the latter can be obtained from Rossiter's modified formula given by Eqn. (1.1). In addition, they require the value of

$\frac{\bar{c}}{U_\infty}$ that can be obtained as follows:

$$\frac{U_\infty}{\bar{c}} = M_\infty \left(1 + \frac{\gamma - 1}{2} M_\infty^2\right)^{-\frac{1}{2}} \tag{A.2}$$

Last but not the least, the non-dimensional groups given in Eqn. (A.1) require an estimate of $O\left(\frac{u'}{U_\infty}\right)$ and $O\left(\frac{v'}{U_\infty}\right)$. The estimations can be obtained from flow visualization experiments.

Having obtained the non-dimensional groups, it is easy to identify the dominant groups among them, the 'dominant' group being defined as having a relative magnitude above 0.1 (or 10%). Eqn. (2.5) and the inequality results given below the equation follow from this definition.

Appendix B

Derivation of Green's Function in 2-D Uncontrolled Cavity Acoustics Model

The Green's function for the pressure field in an uncontrolled cavity can be obtained using polar coordinates as follows. Consider the following separation of variables of the pressure perturbation term:

$$p' \sim R(r)\,\Gamma(\phi)\,P(t) \sim F(x,y)\,P(t) \tag{B.1}$$

The governing equation (2.5) becomes:

$$\frac{1}{\bar{c}^2 P}\frac{d^2P}{dt^2} = \frac{1}{Rr}\frac{d}{dr}\left(r\frac{dR}{dr}\right) + \frac{1}{r^2\Gamma}\frac{d^2\Gamma}{d\phi^2} \tag{B.2}$$

This leads to three set of equations:

$$\begin{aligned} \frac{1}{\bar{c}^2 P}\frac{d^2P}{dt^2} &= -\frac{\omega^2}{\bar{c}^2} \\ \frac{1}{r}\frac{d}{dr}\left(r\frac{dR}{dr}\right) + \left(\frac{\omega^2}{\bar{c}^2} - \frac{m^2}{r^2}\right)R &= 0 \\ \frac{1}{\Gamma}\frac{d^2\Gamma}{d\phi^2} &= -m^2\,(m = 0,1,2,3,\cdots) \end{aligned} \tag{B.3}$$

The solutions of three equations are, respectively:

$$\begin{aligned} \Gamma(\phi) &= \cos(m\phi), \sin(m\phi) \\ R(r) &= \frac{Q}{2\pi} H_m^{(1)}\left(\frac{\omega}{\bar{c}} r\right) \\ P(t) &= e^{-i\omega t}, e^{i\omega t} \end{aligned} \tag{B.4}$$

Choosing the solution that represents outgoing waves propagating uniformly outwards ($m = 0$), we get the Green's function as follows:

$$p'(r,t) = \underbrace{\frac{Q}{2\pi} H_0^{(1)}\left(\frac{\omega}{\bar{c}} r\right)}_{F(x,y)} \exp(i\omega t) + (\cdot)^* \tag{B.5}$$

Appendix C

Relationship Between Microjet Pressure and Associated Leading Edge Shock Geometry

The problem associated with a shock due to jet in cross-flow is traditionally modelled as follows. The jet turns and starts mixing with the external cross-flow and is treated as an 'equivalent' solid body, as illustrated in Figure 2-8. The shock trajectory due to such a blunt body in the presence of a supersonic flow is[27]:

$$\frac{x_{shock}}{r} = \frac{R_b}{r} + \frac{\delta}{R_b}\frac{R_b}{r} - \frac{R_c}{R_b}\frac{R_b}{r}\cot\mu\left\{\sqrt{1+\left(\frac{y_{shock}}{r}\right)^2\left(\frac{r}{R_b}\right)^2\left(\frac{R_b}{R_c}\right)^2\tan^2\mu} - 1\right\} \quad \text{(C.1)}$$

where $\frac{\delta}{R_b} = 0.143\exp\frac{3.24}{M_\infty^2}$, $\frac{R_c}{R_b} = 1.143\exp\frac{0.54}{(M_\infty-1)^{1.2}}$, $\cot\mu = \sqrt{M_\infty^2-1}$ and $\frac{R_b}{2r} = 4.34J^{0.36}$. Following Papamoschou and Hubbard[16], we have:

$$J = \frac{\rho_{jet}U_{jet}^2}{\rho_\infty U_\infty^2}. \quad \text{(C.2)}$$

Here, the subscript '*jet*' refers to the flow conditions at the jet exit into the cross-flow. Also, Eqn. (C.1) is valid for $y_{shock} > 0.5417\frac{R_b}{r} + 0.0205$.

This empirical relationship connects the microjet-cross-flow momentum flux ratio to the shock trajectory. From this, we can estimate the near-field and far-field shock angles for the FSU cavity arrangement. The results are illustrated in Figures C-1 and C-2. The

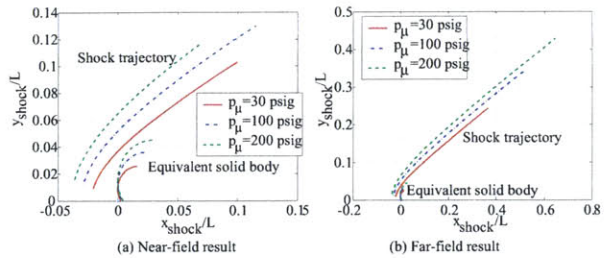

Figure C-1: Predicted shock trajectory based on Schetz[27] and Papamoschou and Hubbard[16]. External flow conditions: $M = 2.0$ and Re = 3 million (based on cavity length).

Figure C-2: Shadowgraph image for the FSU cavity corresponding to 30 psig microjet pressure. The encircled region was used for calculating the shock angle. External flow conditions: $M = 2.0$ and Re = 3 million (based on cavity length). Cavity dimension: $L/D = 5.1$.

shock angles predicted by the model and FSU experiments are shown in Table C.1, and the results of the FSU experiments are taken from Zhuang, et. al.[1]

It is clear that the far-field shock angle predicted by the model corresponds to the Mach angle for a 2.0 Mach flow and that there is a close match of the near-field shock angle between this empirical model and the FSU experiments, thus validating the model. Therefore, this model can be used in applications that require the shape of the shock for any jet-in-cross-flow setup.

Table C.1: Shock angles predicted by model and obtained from experiments done on FSU cavity (under $M = 2.0$ and Re = 3 million flow). Re is based on cavity length.

p_μ, psig	30	100	200
Experiment, deg	37	38	42
Near-field, theory (deg)	36.5	37.8	42.4
Far-field, theory (deg)	29.9	29.9	29.9

Appendix D

Derivation of Forcing Function in 2-D Cavity Acoustics Model

In this section, we derive the forcing function associated with uniform spanwise microjet firing at the cavity leading edge. Retaining the first order terms, the force addition (i.e., rate of change of momentum per unit volume) due to introduction of microjets at the leading edge is given by:

$$\overrightarrow{f}_{\mu} = \frac{\partial \rho U_{\mu}}{\partial t} S(x,y)\,\widehat{j} \tag{D.1}$$

where

$$S(x,y) = \begin{cases} 1 & 0 \le x \le 2r, 0 \le y \le \varepsilon \ll 1 \\ 0 & |x| \gg 2r, |y| \gg \theta \end{cases}$$

such that $O(\nabla S) = 0\ \forall x, y$. Also θ is the transverse mixing length at injection point and is considered to be equal in magnitude to the penetration depth of the microjets in the cross-flow. Last but not the least, U_{μ} is the microjet velocity at the nozzle exit, as shown in Figure 2-8. Then we can write:

$$\nabla \cdot \overrightarrow{f}_{\mu} = \frac{\partial}{\partial y}\frac{\partial}{\partial t}\left(\overline{\rho} + \frac{1}{\overline{c}^2}p'\right) U_{\mu} S(x,y) \tag{D.2}$$

Having obtained an expression for the forcing function, we use Green's function technique and method of images to solve the governing equation given by (2.13). The Green's

function can be obtained as follows. Consider:

$$p' \sim F(x,y)P(t) \tag{D.3}$$

The governing equation (2.13) becomes:

$$\frac{d^2P}{dt^2} - \frac{\bar{c}^2\nabla^2 F}{F}P = -\frac{\partial}{\partial t}\left[\frac{P}{F}\frac{\partial F U_\mu}{\partial y}\right]S(x,y) - \bar{c}^2\overline{\rho}\frac{\partial}{\partial t}\left[\frac{1}{F}\frac{\partial U_\mu}{\partial y}\right]S(x,y) \tag{D.4}$$

It is shown in Eqn. (2.17) that F is the first order first kind Hankel function. So, we have:

$$\bar{c}^2\nabla^2 F = \omega'^2 F \tag{D.5}$$

Also, consider the term $\left[\frac{1}{F}\frac{\partial F}{\partial y}U_\mu + \frac{\partial U_\mu}{\partial y}\right]S(x,y)$ in Eqn. (D.4). Here,

$$O\left(\frac{1}{F}\frac{\partial F}{\partial y}U_\mu\right)S(x,y) = \frac{\omega'}{\bar{c}}\varepsilon U_\mu \tag{D.6}$$

where ε is arbitrarily small. Moreover,

$$\frac{\partial \overline{U}_\mu}{\partial y}S(x,y) = \frac{\xi \overline{U}_\mu}{\theta} \tag{D.7}$$

where $\overline{U}_\mu$ is the mean component of the microjet exit velocity, $\xi < 1$ and can be estimated from flow visualization experiments and is also derived later in Eqn. (D.15). Assuming that the perturbation component of the microjet exit velocity is not dominant over the mean component, we can make the following estimation: $O\frac{\partial U_\mu}{U_\mu \partial y}S(x,y) = \frac{\xi}{\theta}$. Then we have:

$$O\left(\frac{\frac{1}{F}\frac{\partial F}{\partial y}U_\mu S(x,y)}{\frac{\partial U_\mu}{\partial y}S(x,y)}\right) = \frac{\omega'}{\bar{c}}\varepsilon\frac{\theta}{\xi} \ll 1 \tag{D.8}$$

Thus, the term in the numerator can be neglected from Eqn. (D.4) because the microjets are introduced at the leading edge and the Hankel function behaves as in Eqn. (D.6) at that point. Next we consider the following expression in Eqn. (D.4):

$$O\left(\frac{\bar{c}^2\overline{\rho}\frac{\partial}{\partial t}\left[\frac{P}{F}\frac{\partial U_\mu}{\partial y}\right]S(x,y)}{\frac{d^2P}{dt^2}}\right) = \gamma O\left(\frac{\overline{P}}{p'}\frac{U_\mu}{U_\infty}\frac{U_\infty}{\omega' L}\frac{\xi L}{\theta}\right) \tag{D.9}$$

where $O\left(\frac{\overline{P}}{p'}\right) \approx 4$, $O\left(\frac{U_\mu}{U_\infty}\right) \approx 1$, $O\left(\frac{\omega' L}{U_\infty}\right) = 8$ for the dominant Rossiter tone and $O\left(\frac{\theta}{\xi L}\right) \approx 3$ for 100 psig microjet pressure (from flow visualization experiment). Here $\overline{P}$ is the mean static pressure at the leading edge. Thus, because of high frequency of the dominant cavity tone and high transverse microjet velocity gradient at the nozzle exit, the numerator in the above expression can be neglected from Eqn. (D.4), resulting in:

$$\frac{d^2P}{dt^2} + \frac{\partial U_\mu}{\partial y}\frac{dP}{dt} + \left(\omega'^2 + \frac{\partial}{\partial t}\frac{\partial U_\mu}{\partial y}\right)P = 0 \tag{D.10}$$

Finally we consider the expression $\omega'^2 + \frac{\partial}{\partial t}\frac{\partial U_\mu}{\partial y}$. We have:

$$O\left(\frac{\omega'^2}{\frac{\partial}{\partial t}\frac{\partial U_\mu}{\partial y}}\right) = O\left(\frac{\omega'\theta}{\xi U_\mu}\right) = O\left(\frac{\omega' L}{U_\infty}\frac{U_\infty}{U_\mu}\frac{\theta}{L\xi}\right) \gg 1 \tag{D.11}$$

So neglecting $\frac{\partial}{\partial t}\frac{\partial U_\mu}{\partial y}$ again because of high frequency of the dominant cavity tone and high transverse microjet velocity gradient, we get:

$$\frac{d^2P}{dt^2} + \frac{\partial U_\mu}{\partial y}(t)\frac{dP}{dt} + \omega'^2 P = 0 \tag{D.12}$$

Now, we proceed to estimate $\frac{\partial U_\mu}{\partial y}$. Since the microjet diameter versus nozzle length is negligible, we can apply quasi-one-dimensional compressible flow analysis to the microjet. Also because the microjets are spaced along the spanwise direction at the leading edge (interjet distance/jet diameter ~ 3.4 for the 12 400 μm microjets) that precludes them from interacting with each other at the nozzle exit, we can consider the jets individually and later integrate their effect along the spanwise direction in the three-dimensional model. From steady quasi-one-dimensional compressible flow analysis, we have the following influence coefficient[29]:

$$\frac{d\overline{M}(y)}{\overline{M}(y)} = \frac{1 + \frac{\overline{M}^2(y)}{5}}{\overline{M}^2(y) - 1}\frac{dA(y)}{A(y)} \tag{D.13}$$

where $A(y)$ is the cross-section area of the jet and γ is taken as $\frac{7}{5}$. Using the relationship

between mean jet velocity and Mach number, we have:

$$\overline{U}_{\mu}(y) = \sqrt{\frac{7}{5}RT_o}\frac{\overline{M}(y)}{\sqrt{1+\frac{\overline{M}^2(y)}{5}}} \tag{D.14}$$

where R is the gas constant of air and T_o is the stagnation temperature of the microjet. Then using Eqn. (D.7), it can be shown that

$$\frac{\xi}{\theta} = \frac{1}{\overline{M}^2(y)-1}\frac{1}{A(y)}\frac{dA(y)}{dy} \tag{D.15}$$

Since currently the shape of the barrel shock region above the microjet exit is not accurately known, we cannot derive the magnitude of $\frac{\xi}{\theta}$ from Eqn. (D.15) but we can use the flow visualization experiments performed on the FSU cavity to get an estimate of the gradient, as mentioned at the end of this section. However, we use Eqn. (D.15) to derive the forcing function as follows.

We have:

$$U_{\mu}(y,t) = \sqrt{\frac{7}{5}RT_b(y)}M(y,t) \tag{D.16}$$

where $T_b(y)$ is the static temperature and $M(y,t)$ is the Mach number of the jet. The relationship between static and stagnation temperature is:

$$T_b(y) = \frac{T_o}{1+\frac{\overline{M}^2(y)}{5}} \tag{D.17}$$

and that between Mach number and pressure ratio is:

$$M(y,t) = \sqrt{5\left[\left(\frac{p_{\mu}}{p_b(x=0,y,t)}\right)^{\frac{2}{7}-1}\right]} \tag{D.18}$$

where p_{μ} is the steady microjet pressure and $p_b(x,y,t)$ is the static pressure. We now use the fact that the nozzle is sonic so that $\overline{M}^2(0) = 1$. Also using Eqn. (D.15), it can be shown that:

$$\frac{\partial U_{\mu}}{\partial y} = \sqrt{\frac{7RT_o}{30}}\frac{\xi}{\theta}\left\{-p_{sq}+\left(\frac{5}{6}\right)^{\frac{7}{2}}\frac{p_r^{\frac{9}{7}}}{p_{sq}}\right\} - \sqrt{\frac{5RT_o}{42}}\frac{p_r^{\frac{2}{7}}}{p_{sq}}\frac{1}{p_b}\frac{\partial p_b'}{\partial y} \tag{D.19}$$

where we can write: $p_b = \bar{p}_b + p'_b$ = static pressure (mean+perturbation quantity), $p_r = \frac{p_\mu}{p_b}$ and $p_{sq} = \sqrt{p_r^{\frac{2}{7}} - 1}$, all referring to the nozzle exit region. The value of $\bar{p}_b$ can be obtained from experimental conditions while p'_b is the result of solving Eqn. (D.12).

In order to obtain an estimate of the mean transverse microjet velocity gradient $\frac{\partial \overline{U}_\mu}{\partial y}$, as mentioned before, we use the results of laser-based flow visualization experiments on the FSU cavity for different microjet pressures. The details of the experiments are given in Zhuang, et. al.[1] The experiments measured the mean streamwise and transverse velocity field inside and outside the cavity. From this data, the velocity gradients were computed. Now the velocity field data is corrupted by laser reflections from the cavity at the upstream end of the domain, up to about $Y/L = 0.03$ in the transverse direction near the leading edge. So the magnitude of $\frac{\partial \overline{U}_\mu}{\partial y}$ was estimated by averaging the transverse gradient in a small box just adjacent to the corrupted region, near the leading edge as shown in Figure D-1. The size of the square box was sufficient to accommodate the initial part of the microjet trace near the leading edge.

The dependence of $\frac{\partial \overline{U}_\mu}{\partial y}$ on microjet pressure is shown in Figure D-1. It is to be noted that the parameter, microjet-cross-flow momentum ratio as defined in Eqn. (C.2), is directly proportional to microjet pressure. Therefore Figure D-1 also illustrates the variation of $\frac{\partial \overline{U}_\mu}{\partial y}$ with jet momentum ratio. From this figure, $\frac{\partial \overline{U}_\mu}{\partial y}$ can be obtained for any microjet pressure or equivalently any momentum ratio by interpolation.

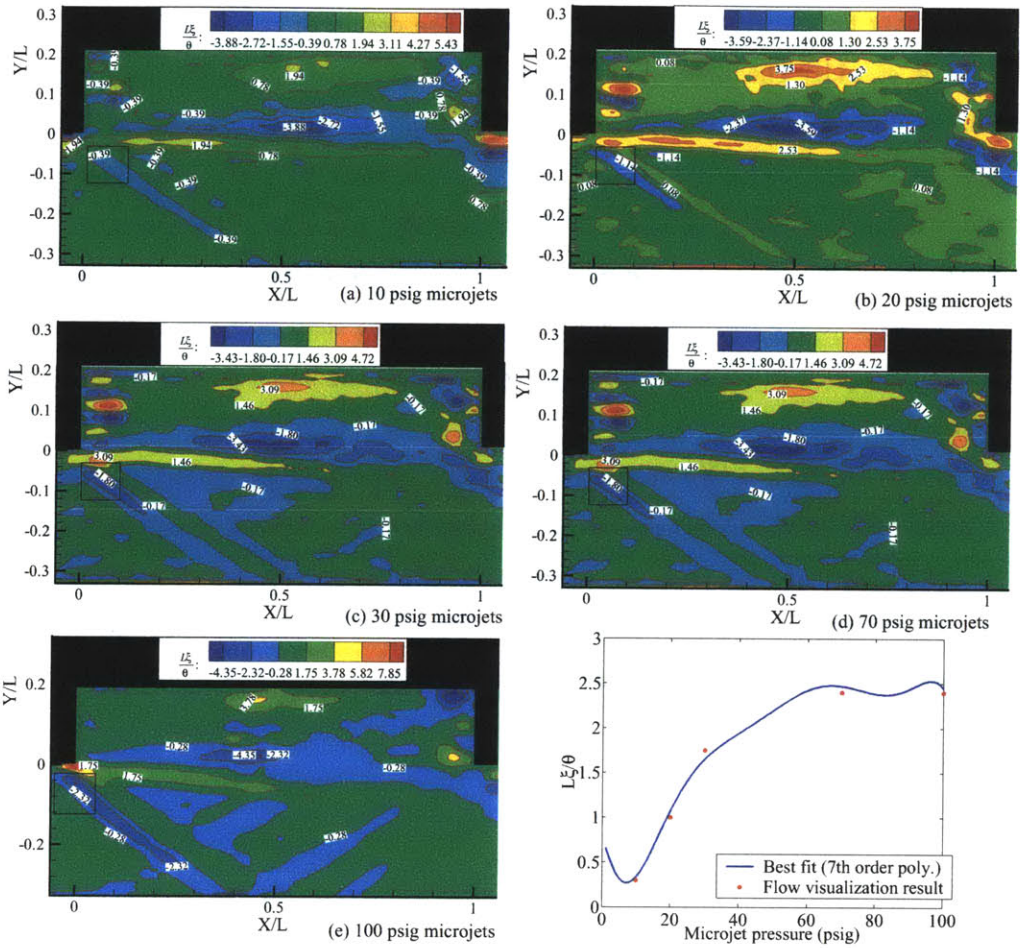

Figure D-1: Flow visualization results for the FSU cavity. Shown here are the mean transverse velocity gradient for different microjet pressures. Notation follows from Eqn. (D.7). The indicated box is the region of averaging for estimating the mean transverse microjet velocity gradient. External flow conditions: $M = 2.0$ and Re = 3 million (based on cavity length). Cavity dimension: $L/D = 5.1$.

Appendix E

Derivation of Forcing Function in 3-D Cavity Acoustics Model

This section shows the derivation of the forcing function in the case when non-uniform spanwise firing of microjets is commenced at the leading edge of the cavity. First, using Eqns. (2.20) and (2.13), we derive the Green's function for the uncontrolled three-dimensional cavity as follows, with the coordinate system for this problem being illustrated in Fig. E-1. Multiply the governing equation (2.13) by $\Phi(z)$ and integrate in the spanwise direction from $z = 0$ to $z = W$ (the cavity width) to get:

$$\frac{1}{\bar{c}^2 P}\frac{d^2 P}{dt^2} = \frac{1}{Rr}\frac{d}{dr}\left(r\frac{dR}{dr}\right) + \frac{1}{r^2\Gamma}\frac{d^2\Gamma}{d\phi^2} + \frac{f_2}{\bar{c}^2},$$

$$f_2 = \frac{\bar{c}^2 \int_0^1 \Phi(z)\frac{d^2\Phi(z)}{dz^2} d\left(\frac{z}{W}\right)}{\int_0^1 \Phi^2(z)\, d\left(\frac{z}{W}\right)} \tag{E.1}$$

This leads to three set of equations:

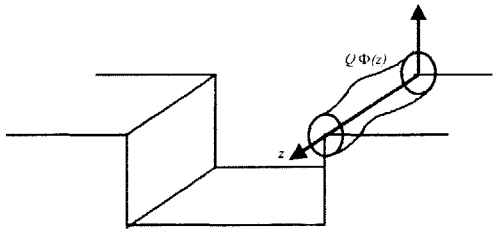

Figure E-1: Coordinate system for the three-dimensional Green's function in the cavity acoustics model.

$$\frac{1}{\bar{c}^2 P}\frac{d^2 P}{dt^2} = -\frac{\omega^2 - f_2}{\bar{c}^2}$$
$$\frac{1}{r}\frac{d}{dr}\left(r\frac{dR}{dr}\right) + \left(\frac{\omega^2}{\bar{c}^2} - \frac{m^2}{r^2}\right) R = 0$$
$$\frac{1}{\Gamma}\frac{d^2\Gamma}{d\phi^2} = -m^2 \tag{E.2}$$

The solutions of three equations are, respectively:

$$\begin{aligned} \Gamma(\phi) &= \cos(m\phi), \sin(m\phi) \\ R(r) &= \frac{Q}{2\pi} H_m^{(1)}\left(\frac{\omega}{\bar{c}} r\right) \\ P(t) &= e^{-it\sqrt{\omega^2 - f_2}}, e^{it\sqrt{\omega^2 - f_2}} \end{aligned} \tag{E.3}$$

Choose the solution that represents outgoing waves propagating uniformly outwards ($m = 0$). Also, we have:

$$O\left(\frac{f_2}{\omega^2}\right) = \frac{\bar{c}^2}{\omega^2 W^2} = \left(\frac{U_\infty}{\omega L}\frac{\bar{c}}{U_\infty}\frac{L}{W}\right)^2 \approx 0.1 \tag{E.4}$$

and so can be neglected because of high frequency of the dominant Rossiter tone. Thus, the Green's function is:

$$p'(r,t) = \frac{Q}{2\pi} H_0^{(1)}\left(\frac{\omega}{\bar{c}} r\right) \Phi(z) \exp(i\omega t) + (\cdot)^* \tag{E.5}$$

The pressure field inside the three-dimensional cavity, given by Eqn. (2.24), follows from the above using the method-of-images.

For the cavity under non-uniform control, following Appendix D, it can be shown that the Green's function satisfies:

$$\frac{d^2 P}{dt^2} + f_1(t)\frac{dP}{dt} + \omega'^2 P = 0 \tag{E.6}$$

where

$$f_1(t) = \frac{1}{\int_0^1 \Phi^2(z)\, d\left(\frac{z}{W}\right)} \left(\int_0^1 \Phi^2(z) \left[\sqrt{\frac{7RT_o}{30}} \frac{\xi}{\theta} \left\{ -p_{sq} + \left(\frac{5}{6}\right)^{\frac{7}{2}} \frac{p_r^{\frac{9}{7}}}{p_{sq}} \right\} - \sqrt{\frac{5RT_o}{42}} \frac{p_r^{\frac{2}{7}}}{p_{sq}} \frac{1}{p_b} \frac{\partial p_b'}{\partial y} \right] d\left(\frac{z}{W}\right) \right) \tag{E.7}$$

Here p_b, p_b', p_r and p_{sq} refer to the leading edge and depend on the spanwise direction z while $\bar{p}_b$ and T_o do not. Also the mean microjet velocity gradient at the jet exit, given by Eqn. (D.7) and obtained from flow visualization experiments, depends on microjet pressure and thus on the spanwise direction.

Eqn. (E.6) was treated similar to (2.15) and (2.16) to estimate the damping factor d_μ. Clearly, this involves estimating pressure field at both the leading and trailing edges. Therefore the model relies on a good coherence between the leading and trailing edge pressure fields. Having obtained the appropriate damping factor, the pressure field inside the controlled cavity given by Eqn. (2.25) can be obtained using the method-of-images.

Appendix F

ARX Model for Leading Edge Pressure Prediction for Cavity Noise Control

Because of lack of space to accommodate pressure sensors at the leading edge due to the presence of microjets, a multivariate system identification analysis package (Auto-Regression with eXogeneous variables (ARX)[26]) can be used to estimate the leading edge pressure readings from the trailing edge ones in the presence of several microjet pressure profiles. The predicted leading edge sensor readings can be used to perform proper orthogonal analysis and thus obtain the dominant spanwise mode $\Phi(z)$. The order of the ARX model is obtained by trial-and-error and is depicted in Figure F-1. This model is validated as follows. The model predicted pressure is compared with the experimental data, derived from a sen-

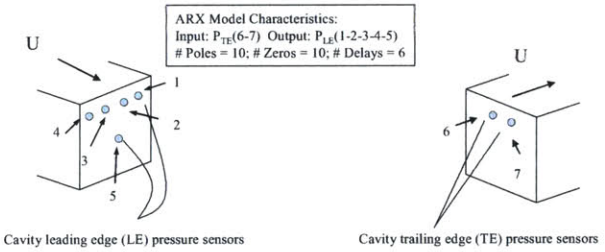

Figure F-1: ARX model used for predicting leading edge pressure data from trailing edge ones in the presence of several microjet pressure profiles. The model was realized using MATLAB's *arx.m* function and the microjet profiles used in this study were: 50-50-50, 200-200-200 and 200-0-200 psig. The microjet pressure naming convention is based on Figure 2-6.

sor located in the middle of the cavity leading edge face. Such a comparison is performed for several control-on situations. One such case is depicted in Figure F-2. Although the ARX model predicts up to 12% of the frequency content of the sensor data (as shown in the figure), the OASPL prediction is close to the experimental one. Since the dominant spanwise mode, obtained from a POD of the leading edge sensors, is mostly influenced by the OASPL, we consider the ARX model to be validated and useful for our purpose of estimating the dominant spanwise mode shape at the leading edge.

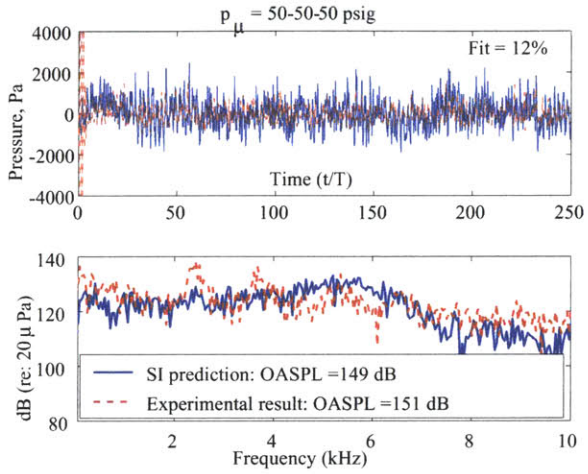

Figure F-2: ARX model output versus experimental sensor reading for 50-50-50 psig microjet pressure. The microjet pressure naming convention is based on Figure 2-6. Location of the pressure sensor: middle of the leading edge face of the cavity. Uncertainty in experimental SPL: $\pm 0.5dB$. Uncertainty in frequency: $\pm 40Hz$. Also, T refers to the time period corresponding to the dominant cavity tone.

Appendix G

Relationship Between Microjet Pressure and Shear Layer Shape, and Plane Shock Strength

The control action consists of the introduction of microjets near the leading edge of the cavity. After being introduced in the transverse direction, microjets turn and start mixing with the external cross-flow, forming a virtual solid body. This obstruction to the cross-flow leads to formation of plane shock waves near the cavity leading edge.

Empirically, the shock strength is governed by the microjet-to-external-flow momentum ratio [Appendix C]. In order to find the empirical relationship for a given microjet pressure profile, flow visualization experiments were conducted on a rectangular cavity of aspect ratio 5.1 under Mach 2.0 flow in the Florida State University (FSU) wind tunnel facility[1]. This setup used 12 microjets of diameter 400 μm at the leading edge. To match the 12 microjet FSU setup with the HIFEX test [3, 4], the momentum ratio parameter C_μ defined in Eqn. (4.36) is used. The numerator in Eqn. (4.36) is the mean momentum flux of all the active microjets while the denominator is the mean momentum flux of the external flow through the cross-section area of the virtual solid body formed by the microjets. The thickness of the body is same as the penetration height of the microjets into the external flow and the latter is of the same order as the boundary layer thickness at the point of injection of microjets into the cross-flow. Also the factor $\frac{1}{4}$ is to take into account the blockage of several microjet holes in the HIFEX setup owing to faulty construction. Additionally, in

Eqn. (4.36), $\delta_{BL} \sim 0.015\hat{L}_o$ for the FSU cavity setup while for the HIFEX setup, $\delta_{BL} \sim 0.017\hat{L}_o$, where $\hat{L}_o$ is the cavity length as shown in Figure N-1.

The shear layer shape for different microjet momentum ratios are given in Figure G-1. From this result, the shear layer shape for any microjet momentum ratio C_μ can be found by interpolation.

The plane shock geometry resulting from the introduction of microjets was also studied for different momentum ratios using flow visualization techniques and the FSU setup. The results are adapted from Zhuang, et. al.[1] and shown in Table G.1. From this table,

Table G.1: Plane shock geometry for different microjet momentum ratios (C_μ) corresponding to the FSU setup. External flow conditions: $M = 2.0$ and Re = 3 million (based on cavity length). Cavity dimension: $L/D = 5.1$.

C_μ	0.119	0.306	0.573
Shock-to-free-stream inclination angle	37	38	42
Angle θ (Figure 4-1)	8	9	12

the shock geometry corresponding to an arbitrary C_μ can be determined by interpolation. Using the shock geometry and plane shock wave theory[36], the external flow properties (density, speed and flow orientation) under the cavity can be determined.

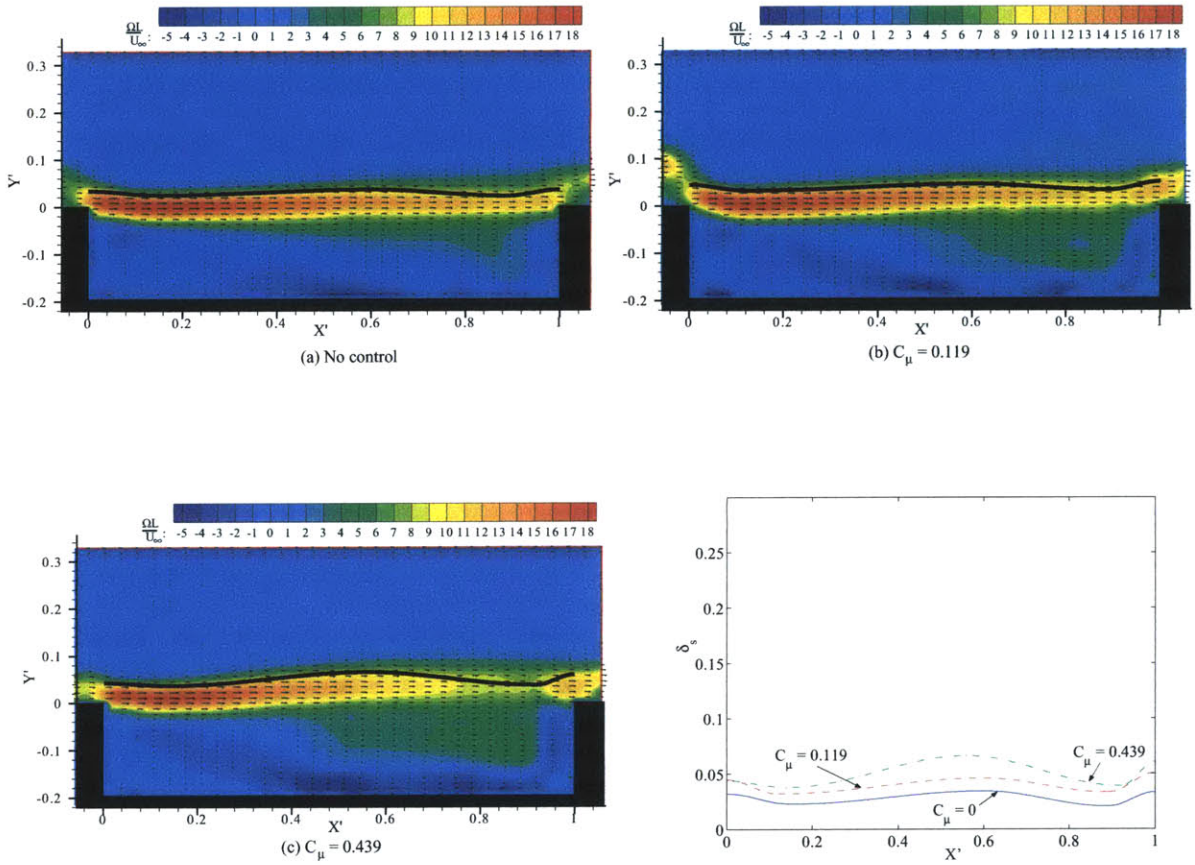

Figure G-1: Flow visualization results for the FSU cavity. Shown here is the shear layer shape for different microjet momentum ratios. The shear layer shape is indicated by a bold line in figures (a), (b) and (c). This line indicates the outer thickness of the shear layer (the side far from the cavity) that have non-negligible vorticity Ω. Here L is the cavity length and U_∞ is the external undisturbed flow speed. The notations X' and Y' are explained in Eqn. (2.10). External flow conditions: $M = 2.0$ and Re = 3 million (based on cavity length). Cavity dimension: $L/D = 5.1$.

Appendix H

Expression for Store Induced Potential and Forces For Inside Cavity

The problem of store drop inside the cavity reduces to a circle falling to the slip surface in an immovable fluid. The solution can be found using the multipole expansion technique (Laurent series)[31]. The resulting potential solution, accurate up to $\pm\frac{1}{256}$, is:

$$\begin{aligned}
\phi &= -(2B - V_e)\, a \sin\theta - aA\cos 2\theta - \frac{2}{3}aC\sin 3\theta, \\
B &= V_e\left[1 - q^2 S_1(q)\right], \\
A &= -2V_e q^3 S_2(q), \\
C &= 3V_e q^4 S_3(q), \\
S_1(q) &= 1 - q^2 - q^4, \\
S_2(q) &= 1 - q^2 - 2q^4, \\
S_3(q) &= 1 - q^2 - 4q^4, \\
V_e &= V_c - \omega x, \\
q &= \frac{a}{2H},
\end{aligned} \tag{H.1}$$

where the non-dimensional scheme given in Appendix N has been followed.

The normal force and moment expressions are given by Eqn. (4.24) with the concerned

parameters, accurate up to $\pm\frac{1}{256}$, are as follows:

$$
\begin{aligned}
g_0 &= -\pi \int_{x_o}^{x_e} a(x)^2 \left(2q^4 + 2q^6 + 1 - 2q^2\right) dx, \\
g_1 &= \pi \int_{x_o}^{x_e} a(x)^2 x \left(2q^4 + 2q^6 + 1 - 2q^2\right) dx, \\
g_2 &= 4\pi \int_{x_o}^{x_e} a(x) x^2 \left(1 + q^2\right) \left(4q^8 + 8q^6 + 3q^2 - 1\right) q^3 dx, \\
g_4 &= \int_{x_o}^{x_e} \left(\frac{3}{16} a(x)^4 + \frac{1}{2} a(x)^2 H^2 - H^4\right) \pi a(x)^4 - 4q^3 \left(3q^2 - 1\right) \left(1 + q^2\right) \pi a(x)\, dx, \\
g_9 &= \int_{x_o}^{x_e} \left(-\frac{3}{16} a(x)^4 - \frac{1}{2} a(x)^2 H^2 + H^4\right) \pi x a(x)^4 + \\
&\quad 32q^9 \left(2q^2 + 1\right) \left(3q^2 - 2\right) \left(1 + q^2\right) \pi x a(x)\, dx, \\
h_0 &= -\pi \int_{x_o}^{x_e} a(x)^2 x \left(2q^4 + 2q^6 + 1 - 2q^2\right) dx, \\
h_1 &= \pi \int_{x_o}^{x_e} x^2 a(x)^2 \left(2q^4 + 2q^6 + 1 - 2q^2\right) dx, \\
h_2 &= 4\pi \int_{x_o}^{x_e} x^3 a(x) \left(1 + q^2\right) \left(4q^8 + 8q^6 + 3q^2 - 1\right) q^3 dx, \\
h_4 &= \int_{x_o}^{x_e} \left(\frac{3}{16} a(x)^4 + \frac{1}{2} a(x)^2 H^2 - H^4\right) \pi x a(x)^4 - \\
&\quad 4xq^3 \left(2q^2 - 1\right) \left(1 + q^2\right) \left(12q^8 + 4q^6 - 2q^4 - q^2 + 1\right) \pi a(x)\, dx, \\
h_9 &= \int_{x_o}^{x_e} \left(-\frac{3}{16} a(x)^4 - \frac{1}{2} a(x)^2 H^2 + H^4\right) \pi x^2 a(x)^4 + \\
&\quad 32q^9 \left(2q^2 + 1\right) \left(3q^2 - 2\right) \left(1 + q^2\right) \pi x^2 a(x)\, dx.
\end{aligned}
\tag{H.2}
$$

Appendix I

Expression for Store Induced Potential and Forces For Store Portion Partially Immersed in External Flow

This problem is solved using conformal transformation[31] of the store region partially immersed in external cross-flow to an 'equivalent' flat plate as shown in Figure 4-5. The corresponding velocity potential is:

$$\begin{aligned}
\phi &= V_e \frac{\sin \pi n}{n} \left(\sqrt{1-\lambda^2} - \frac{2nQ^n}{D} \sin \pi n \right) - \frac{2a}{\pi} \frac{da}{dx} \sqrt{1-\lambda^2} E, \\
D &= Q^{2n} - 2Q^n \cos \pi n + 1, \\
\lambda &= \frac{\xi}{b}, \\
E &= \int_{-1}^{1} \frac{\psi(s)\, ds}{\sqrt{1-s^2}\,(s-\lambda)}, \\
\psi(s) &= \tan^{-1} \left(\frac{Q^n - 1}{Q^n + 1} \cot \frac{\pi n}{2} \right), \\
V_e &= V_c - \alpha - \omega x,
\end{aligned} \tag{I.1}$$

where E refers to the principal value of the integral in the above equation, Q and n are given by Eqn. (4.26), σ, ξ and b are referred to in Figure 4-5 and the non-dimensional scheme given in Appendix N is followed. Based on this potential, the $\hat{F}$ and $\hat{M}$ expressions are

obtained. They are given by:

$$\hat{F} = \pi\hat{\rho}_\infty \delta \hat{l}_o^3 \left(g_0 \frac{d\hat{V}_c}{d\hat{t}} \hat{l}_o + g_1 \frac{d\hat{\omega}}{d\hat{t}} \hat{l}_o^2 + g_2 \hat{\omega}^2 \hat{l}_o^2 + U_\infty^2 g_3 \hat{\alpha}^2 + g_4 \hat{V}_c^2 + U_\infty \delta g_5 \hat{\omega} \hat{l}_o + \right.$$
$$\left. U_\infty^2 \delta g_6 \hat{\alpha} + U_\infty \delta g_7 \hat{V}_c + U_\infty g_8 \hat{\alpha}\hat{\omega} \hat{l}_o + g_9 \hat{\omega} \hat{l}_o \hat{V}_c + U_\infty g_{10} \hat{\alpha} \hat{V}_c + \delta^2 U_\infty^2 g_{11} \right)$$
$$\hat{M} = \pi\hat{\rho}_\infty \delta \hat{l}_o^4 \left(h_0 \frac{d\hat{V}_c}{d\hat{t}} \hat{l}_o + h_1 \frac{d\hat{\omega}}{d\hat{t}} \hat{l}_o^2 + h_2 \hat{\omega}^2 \hat{l}_o^2 + U_\infty^2 h_3 \hat{\alpha}^2 + h_4 \hat{V}_c^2 + U_\infty \delta h_5 \hat{\omega} \hat{l}_o \right.$$
$$\left. + U_\infty^2 \delta h_6 \hat{\alpha} + U_\infty \delta h_7 \hat{V}_c + U_\infty h_8 \hat{\alpha}\hat{\omega} \hat{l}_o + h_9 \hat{\omega} \hat{l}_o \hat{V}_c + U_\infty h_{10} \hat{\alpha} \hat{V}_c + \delta^2 U_\infty^2 h_{11} \right) \qquad \text{(I.2)}$$

with the concerned parameters, accurate up to $\pm\frac{1}{256}$, are as follows:

$$g_0 = -\int_{x_1}^{x_2} a(x)^2 \left[\Phi_1(n) + \Phi_p(m)\right] dx,$$
$$g_1 = \int_{x_1}^{x_2} a(x)^2 x \left[\Phi_1(n) + \Phi_p(m)\right] dx,$$
$$g_2 = \int_{x_1}^{x_2} x^2 \left[a(x) P_1(x,t) - P_p(x,t)\right] + \frac{x^2 a(x)^2 \left[\frac{d}{dm}\Phi_p(m) - \frac{d}{dn}\Phi_1(n)\right]}{\pi\sqrt{a(x)^2 - H^2}} dx,$$
$$g_3 = \int_{x_1}^{x_2} a(x) P_1(x,t)\, dx,$$
$$g_4 = \int_{x_1}^{x_2} a(x) P_1(x,t) - P_p(x,t) + \frac{a(x)^2 \left[\frac{d}{dm}\Phi_p(m) - \frac{d}{dn}\Phi_1(n)\right]}{\pi\sqrt{a(x)^2 - H^2}} dx,$$
$$g_5 = \int_{x_1}^{x_2} a(x) \frac{da}{dx}(x) x \left[\frac{a(x)\frac{d}{dn}\Phi_2(n)}{\pi\sqrt{a(x)^2 - H^2}} - P_{12}(x,t)\right] + \Phi_1(n) a(x)^2\, dx +$$
$$a(x_2)^2 \Phi_1(n_2) x_2 - a(x_1)^2 \Phi_1(n_1) x_1,$$
$$g_6 = -\int_{x_1}^{x_2} a(x) \frac{da}{dx}(x) P_{12}(x,t)\, dx + a(x_2)^2 \Phi_1(n_2) - a(x_1)^2 \Phi_1(n_1),$$
$$g_7 = \int_{x_1}^{x_2} a(x) \frac{da}{dx} \left[P_{12}(x,t) - \frac{a(x)\frac{d}{dn}\Phi_2(n)}{\pi\sqrt{a(x)^2 - H^2}}\right] dx + a(x_1)^2 \Phi_1(n_1) - a(x_2)^2 \Phi_1(n_2),$$
$$g_8 = \int_{x_1}^{x_2} a(x) x \left[2P_1(x,t) - \frac{a(x)\frac{d}{dn}\Phi_1(n)}{\pi\sqrt{a(x)^2 - H^2}}\right] dx,$$
$$g_9 = 2\int_{x_1}^{x_2} x \left[P_p(x,t) - a(x) P_1(x,t)\right] + \frac{a(x)^2 x \left[\frac{d}{dn}\Phi_1(n) - \frac{d}{dm}\Phi_p(m)\right]}{\pi\sqrt{a(x)^2 - H^2}} dx,$$
$$g_{10} = \int_{x_1}^{x_2} a(x) \left[\frac{a(x)\frac{d}{dn}\Phi_1(n)}{\pi\sqrt{a(x)^2 - H^2}} - 2P_1(x,t)\right] dx,$$

$$
\begin{aligned}
g_{11} &= a(x_1)^2 \frac{da}{dx}(x_1)\,\Phi_2(n_1) - \int_{x_1}^{x_2} a(x) \frac{da}{dx}^2 P_2(x,t)\,dx - a(x_2)^2 \frac{da}{dx}(x_2)\,\Phi_2(n_2),\\
h_0 &= -\int_{x_1}^{x_2} a(x)^2 x\,[\Phi_1(n) + \Phi_p(m)]\,dx,\\
h_1 &= \int_{x_1}^{x_2} a(x)^2 x^2\,[\Phi_1(n) + \Phi_p(m)]\,dx,\\
h_2 &= \int_{x_1}^{x_2} x^3\,[a(x) P_1(x,t) - P_p(x,t)] + \frac{x^3 a(x)^2 \left[\frac{d}{dm}\Phi_p(m) - \frac{d}{dn}\Phi_1(n)\right]}{\pi\sqrt{a(x)^2 - H^2}}\,dx,\\
h_3 &= \int_{x_1}^{x_2} x a(x) P_1(x,t)\,dx,\\
h_4 &= \int_{x_1}^{x_2} x\,[a(x) P_1(x,t) - P_p(x,t)] + \frac{a(x)^2 x\left[\frac{d}{dm}\Phi_p(m) - \frac{d}{dn}\Phi_1(n)\right]}{\pi\sqrt{a(x)^2 - H^2}}\,dx,\\
h_5 &= \int_{x_1}^{x_2} x^2 a(x) \frac{da}{dx}(x)\left[\frac{a(x)\frac{d}{dn}\Phi_2(n)}{\pi\sqrt{a(x)^2 - H^2}} - P_{12}(x,t)\right]dx\\
&\quad + x_2{}^2 a(x_2)^2\,\Phi_1(n_2) - x_1{}^2 a(x_1)^2\,\Phi_1(n_1),\\
h_6 &= -a(x_1)^2\,\Phi_1(n_1)\,x_1 + a(x_2)^2\,\Phi_1(n_2)\,x_2 -\\
&\quad \int_{x_1}^{x_2} \Phi_1(n)\,a(x)^2 - x a(x) \frac{da}{dx}(x) P_{12}(x,t)\,dx,\\
h_7 &= \int_{x_1}^{x_2} a(x)\left[a(x)\,\Phi_1(n) + x\frac{da}{dx}(x) P_{12}(x,t)\right] - \frac{a(x)^2 x\frac{da}{dx}(x)\frac{d}{dn}\Phi_2(n)}{\pi\sqrt{a(x)^2 - H^2}}\,dx +\\
&\quad a(x_1)^2\,\Phi_1(n_1)\,x_1 - a(x_2)^2\,\Phi_1(n_2)\,x_2,\\
h_8 &= \int_{x_1}^{x_2} 2x^2 a(x) P_1(x,t) - \frac{a(x)^2 x^2 \frac{d}{dn}\Phi_1(n)}{\pi\sqrt{a(x)^2 - H^2}}\,dx,\\
h_9 &= 2\int_{x_1}^{x_2} x^2\,[P_p(x,t) - a(x) P_1(x,t)] + \frac{a(x)^2 x^2\left[\frac{d}{dn}\Phi_1(n) - \frac{d}{dm}\Phi_p(m)\right]}{\pi\sqrt{a(x)^2 - H^2}}\,dx,\\
h_{10} &= \int_{x_1}^{x_2} -2x a(x) P_1(x,t) + \frac{a(x)^2 x\frac{d}{dn}\Phi_1(n)}{\pi\sqrt{a(x)^2 - H^2}}\,dx,\\
h_{11} &= \int_{x_1}^{x_2} -a(x)\left[\frac{da}{dx}(x)\right]^2 P_2(x,t)\,x + a(x)^2 \frac{da}{dx}(x)\,\Phi_2(n)\,dx +\\
&\quad x_1 a(x_1)^2 \frac{da}{dx}(x_1)\,\Phi_2(n_1) - x_2 a(x_2)^2 \frac{da}{dx}(x_2)\,\Phi_2(n_2),\\
P_1(x,t) &= -2.2n^5 + 8.9n^4 - 7.8n^3 - 2.8n^2 + 3.1n - 0.67,\\
P_2(x,t) &= 46543.4n^3 - 11980.9n^2 + 758.1n + \frac{\pi}{2}\ (n < 0.13),\\
&= -7.8n^3 + 8.8n^2 + 0.91n - 0.35\,(n \geq 0.13),\\
P_{12}(x,t) &= -10n^5 + 38n^4 - 36n^3 + 5n^2 - 0.66n + 0.19,
\end{aligned}
$$

$$
\begin{aligned}
P_p(x,t) &= \sin(\pi m)\left[1-\frac{1+\pi m\left(1+2m^2\right)\cot(\pi m)}{6m^3}\right](n<0.9), \\
&= 501427.6n^2-969470.9n+468042.7\,(n\geq 0.9), \\
\Phi_1(n) &= -23n^7+59n^6-27n^5-30n^4+28n^3-7.8n^2+0.071n+2, \\
\frac{d\Phi_1(n)}{dn} &= -161n^6+354n^5-135n^4-120n^3+84n^2-15.6n+0.071, \\
\Phi_2(n) &= 5.8n^5-28n^4+34n^3-9.6n^2+0.3n-2.4, \\
\frac{d\Phi_2(n)}{dn} &= 29n^4-112n^3+102n^2-19.2n+0.3, \\
\Phi_p(n) &= 23n^7-100n^6+160n^5-100n^4+6.9n^3+13n^2+0.12n-0.0013, \\
\frac{d\Phi_p(n)}{dn} &= 161n^6-600n^5+800n^4-400n^3+20.7n^2+26n+0.12. \qquad \text{(I.3)}
\end{aligned}
$$

Here m, n are defined in Eqn. (4.27). In addition, the expressions for $P_1, \cdots, \Phi_p$ are obtained by the process of polynomial fit, wherever applicable, instead of their exact expression given by Malmuth, et. al.[31] This is done to achieve faster computation and to avoid the problem of singularities associated with the exact expressions.

It is to be noted that Eqn. (I.3) gives the contribution of the store portion partially immersed in external flow to $\hat{F}$ and $\hat{M}$. The contribution of the store portion inside the cavity to $\hat{F}$ and $\hat{M}$ is given in Appendix H, while that of the portion outside the cavity is given in Appendix L (Eqn. (L.2)).

Appendix J

No-cavity Model for Store Outside Cavity

When the store is far from the cavity (i.e., $H \gg a$ in Figure N-1), the cavity walls and the shear layer are not expected to play any role in determining the potential. The problem can be formulated in terms of a slender axi-symmetric body falling in an unbounded free stream with the associated potential satisfying Laplace Equation in every store cross-section. In the store cross-section plane, the problem thus reduces to the vertical motion of a circle of radius $a(x)$ with a velocity V_e under a uniform flow U_∞ perpendicular to the plane, following the non-dimensional scheme given in Appendix N. This problem is further illustrated in Figure J-1(a).

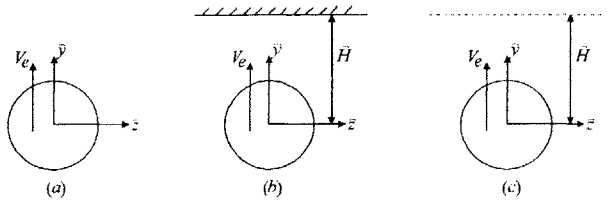

Figure J-1: (a) Motion of a circle falling in an unbounded stream, representing far-from-cavity conditions. (b) Motion of a circle falling from a rigid wall, representing a cavity of zero depth. (c) Motion of a circle falling from a free surface, representing store falling away from the shear layer. In all cases, the free stream is in the $\hat{X}$-direction.

The vertical velocity of the circle that represents the store cross-section $a(x)$ is given by:

$$V_e = V_c - \alpha - \omega x - V_{wavy} - V_{shock} \tag{J.1}$$

where the first term on the right hand side is the vertical store c. g. velocity, the second term is the upwash due to the store angle of attack and the third term is due to the store rotation about its c. g. In addition, V_{wavy} arises from the non-uniformity in the free stream due to the wavy structures and V_{shock} arises from the shock waves due to microjets. Now V_{wavy} is given by:

$$V_{wavy} = -\frac{\delta_s}{2\delta} h'\left(X' + \beta Y'\right)\Big|_{X'=X'_c+\mu x, Y'=Y'_c-\mu\delta\alpha x} \tag{J.2}$$

where the factor 2 takes care of $U_{\infty,r} = 0.5U_\infty$. To estimate V_{wavy}, we assume that the wavy structures consist of piecewise cosine components as in Eqn. (4.18). Then

$$|V_{wavy}| \leq \frac{\delta_s}{2\delta}\beta \max_i \left(W_i\lambda_i\right) \tag{J.3}$$

Now $\frac{\beta}{2} = O(1)$, $(W_i\lambda_i) \leq O(10)$. So if $\frac{\delta_s}{\delta} \leq 0.01$ which implies that the shear layer is much thinner than the store, V_{wavy} is negligible.

The remaining item to analyze is V_{shock}. Basing on assumption (5), we assert that there is negligible non-uniformity in flow (or equivalently, flow is potential) through the region in the front of the shock waves at the cavity leading edge. So V_{shock}, which arises because of this non-uniformity (or non-potential flow), can be neglected. Then, assuming thin shear layer and using assumption (5), we have:

$$V_e = V_c - \alpha - \omega x \tag{J.4}$$

The problem of free fall of a circle in unbounded medium can be solved by choosing the following potential solution:

$$\phi = V_e a \sin\theta \tag{J.5}$$

The complete expressions for the corresponding $\hat{F}$ and $\hat{M}$ in this case are given by:

$$\begin{aligned}
\hat{F} &= \pi\hat{\rho}_\infty\delta\hat{l}_o^3\left(-G_0\frac{d\hat{V}_c}{d\hat{t}}\hat{l}_o + G_1\frac{d\hat{\omega}}{d\hat{t}}\hat{l}_o^2 + U_\infty\delta\left(G_0 + x_e a\left(x_e\right)^2\right)\hat{\omega}\hat{l}_o + \right. \\
&\quad \left. U_\infty^2\delta a\left(x_e\right)^2\hat{\alpha} - U_\infty\delta a\left(x_e\right)^2\hat{V}_c\right) \\
\hat{M} &= \pi\hat{\rho}_\infty\delta\hat{l}_o^4\left(-G_1\frac{d\hat{V}_c}{d\hat{t}}\hat{l}_o + G_2\frac{d\hat{\omega}}{d\hat{t}}\hat{l}_o^2 + U_\infty\delta x_e^2 a\left(x_e\right)^2\hat{\omega}\hat{l}_o\right. \\
&\quad \left. -U_\infty^2\delta\left(G_0 - x_e a\left(x_e\right)^2\right)\hat{\alpha} + U_\infty\delta\left(G_0 - x_e a\left(x_e\right)^2\right)\hat{V}_c\right).
\end{aligned} \tag{J.6}$$

with G_0 and G_2 being store shape dependent parameters that are given in the following list:

$$\begin{aligned}
G_0 &= \int_{x_o}^{x_e} a^2\left(x\right)\,dx, \\
G_1 &= \int_{x_o}^{x_e} a^2\left(x\right)x\,dx, \\
G_2 &= \int_{x_o}^{x_e} a^2\left(x\right)x^2\,dx.
\end{aligned} \tag{J.7}$$

Appendix K

Zero-depth-cavity Model for Store Outside Cavity

When the cavity depth is small or zero (i.e., $H \gg H_o$ in Figure N-1) but the store is close to the cavity (i.e., $O\left(\frac{H}{a}\right) = 1$ in Figure N-1), the problem reduces to a circle falling from a rigid wall, as illustrated in Figure J-1(b).

The problem of free fall of a circle from a rigid wall can be solved using the multipole expansion technique (Laurent series)[31]. The potential solution, accurate up to $\pm\frac{1}{256}$, is:

$$\begin{aligned}
\phi &= -(2B - V_e)\, a \sin\theta - aA\cos 2\theta, \\
B &= V_e\left[1 + q^2 S_1(q)\right] + q\frac{da}{dx} S_2(q), \\
A &= -q^2\left[\frac{da}{dx} S_3(q) + 2V_e q S_4(q)\right], \\
S_1(q) &= 1 + q^2 + 3q^4 + 8q^6, \\
S_2(q) &= 1 + q^2 + 2q^4 + 5q^6, \\
S_3(q) &= 1 + 2q^2 + 5q^4 + 14q^6, \\
S_4(q) &= 1 + q^2 + 4q^4, \\
q &= \frac{a}{2|H|} \leq \frac{1}{2},
\end{aligned} \tag{K.1}$$

with V_e given by Eqn. (J.4) again assuming thin shear layer and using assumption (5). Also the non-dimensional scheme of Appendix N is followed.

The corresponding $\hat{F}$ and $\hat{M}$ expressions are given by Eqn. (I.2) with the concerned

parameters, accurate up to $\pm\frac{1}{256}$, are as follows:

$$
\begin{aligned}
g_0 &= -\int_{x_o}^{x_e} a^2\left(2q^4+6q^6+1+2q^2+16q^8\right)\,dx,\\
g_1 &= \int_{x_o}^{x_e} a^2x\left(2q^4+6q^6+1+2q^2+16q^8\right)\,dx,\\
g_2 &= \int_{x_o}^{x_e} 4ax^2\left(6q^2+72q^6+3+15q^8+24q^4\right)q^3\,dx,\\
g_3 &= \int_{x_o}^{x_e} 4a\left(15q^8+8q^6+1+2q^2+6q^4\right)q^3\,dx,\\
g_4 &= \int_{x_o}^{x_e} 4a\left(6q^2+72q^6+3+15q^8+24q^4\right)q^3\,dx,\\
g_5 &= \int_{x_o}^{x_e}\left(-2q^2\right)\left(35q^4+116q^6+4+12q^2\right)a\frac{da}{dx}x+a^2\left(2q^4+6q^6+1+2q^2+16q^8\right)dx+\\
&\quad \left(2q\left(x_e\right)^4+2q\left(x_e\right)^2+1+6q\left(x_e\right)^6+16q\left(x_e\right)^8\right)a\left(x_e\right)^2x_e,\\
g_6 &= \int_{x_o}^{x_e}\left(-2q^2\right)\left(15q^4+46q^6+6q^2+2\right)a\frac{da}{dx}\,dx\\
&\quad +\left(2q\left(x_e\right)^4+2q\left(x_e\right)^2+1+6q\left(x_e\right)^6+16q\left(x_e\right)^8\right)a\left(x_e\right)^2,\\
g_7 &= \int_{x_o}^{x_e} 2q^2\left(35q^4+116q^6+4+12q^2\right)a\frac{da}{dx}\,dx\\
&\quad +\left(-2q\left(x_e\right)^2-6q\left(x_e\right)^6-1-16q\left(x_e\right)^8-2q\left(x_e\right)^4\right)a\left(x_e\right)^2,\\
g_8 &= \int_{x_o}^{x_e} 8ax\left(2+4q^2+40q^6+15q^4+15q^8\right)q^3\,dx,\\
g_9 &= -\int_{x_o}^{x_e} 8ax\left(6q^2+72q^6+3+15q^8+24q^4\right)q^3\,dx,\\
g_{10} &= -\int_{x_o}^{x_e} 8a\left(2+4q^2+40q^6+15q^4+15q^8\right)q^3\,dx,\\
g_{11} &= \int_{x_o}^{x_e} 2q\left(1+14q^6+2q^2+5q^4\right)a\left(\frac{da}{dx}\right)^2dx+\\
&\quad \left(-10q\left(x_e\right)^7-4q\left(x_e\right)^5-2q\left(x_e\right)-2q\left(x_e\right)^3\right)a\left(x_e\right)^2\left.\frac{da}{dx}\right|_{x_e},\\
h_0 &= -\int_{x_o}^{x_e} a^2x\left(2q^4+6q^6+1+2q^2+16q^8\right)\,dx,\\
h_1 &= \int_{x_o}^{x_e} x^2a^2\left(2q^4+6q^6+1+2q^2+16q^8\right)\,dx,\\
h_2 &= \int_{x_o}^{x_e} 4x^3a\left(6q^2+72q^6+3+15q^8+24q^4\right)q^3\,dx,\\
h_3 &= \int_{x_o}^{x_e} 4ax\left(4q^4+q^2+1\right)\left(8q^8+3q^6+q^4+q^2+1\right)q^3\,dx,\\
h_4 &= \int_{x_o}^{x_e} 4ax\left(6q^2+72q^6+3+15q^8+24q^4\right)q^3\,dx,
\end{aligned}
$$

$$
\begin{aligned}
h_5 &= -\int_{x_o}^{x_e} 2q^2\left(35q^4+116q^6+4+12q^2\right)a\frac{da}{dx}x^2\,dx + \\
&\quad \left(2q\left(x_e\right)^4+2q\left(x_e\right)^2+1+6q\left(x_e\right)^6+16q\left(x_e\right)^8\right)a\left(x_e\right)^2x_e^2, \\
h_6 &= \int_{x_o}^{x_e}\left(-2q^2\right)\left(15q^4+46q^6+6q^2+2\right)a\frac{da}{dx}x+\left(-2q^2-2q^4-6q^6-16q^8-1\right)a^2\,dx \\
&\quad +\left(2q\left(x_e\right)^4+2q\left(x_e\right)^2+1+6q\left(x_e\right)^6+16q\left(x_e\right)^8\right)a\left(x_e\right)^2x_e, \\
h_7 &= \int_{x_o}^{x_e} 2q^2\left(35q^4+116q^6+4+12q^2\right)a\frac{da}{dx}x+a^2\left(2q^4+6q^6+1+2q^2+16q^8\right)\,dx - \\
&\quad \left(2q\left(x_e\right)^4+2q\left(x_e\right)^2+1+6q\left(x_e\right)^6+16q\left(x_e\right)^8\right)a\left(x_e\right)^2x_e, \\
h_8 &= \int_{x_o}^{x_e} 8ax^2\left(q^2+1\right)\left(-12q^8+27q^6+13q^4+2q^2+2\right)q^3\,dx, \\
h_9 &= -\int_{x_o}^{x_e} 8ax^2\left(6q^2+72q^6+3+15q^8+24q^4\right)q^3\,dx, \\
h_{10} &= -\int_{x_o}^{x_e} 8ax\left(q^2+1\right)\left(-12q^8+27q^6+13q^4+2q^2+2\right)q^3\,dx, \\
h_{11} &= \int_{x_o}^{x_e} 2q\left(1+14q^6+2q^2+5q^4\right)a\left(\frac{da}{dx}\right)^2x+2q\left(5q^6+1+q^2+2q^4\right)a^2\frac{da}{dx}\,dx \\
&\quad -2x_eq\left(x_e\right)\left(1+q\left(x_e\right)^2+2q\left(x_e\right)^4+5q\left(x_e\right)^6\right)a\left(x_e\right)^2\left.\frac{da}{dx}\right|_{x_e} \qquad \text{(K.2)}
\end{aligned}
$$

Appendix L

Model for Store Outside But Near Cavity

When the store is outside but near the cavity (i.e., $O\left(\frac{H}{a}\right) = 1$ in Figure N-1), the problem reduces to a circle falling from a free surface (the shear layer slip surface), as illustrated in Figure J-1(c). Again this can be solved using the multipole expansion technique (Laurent series)[31]. The potential solution, accurate up to $\pm\frac{1}{256}$, is:

$$
\begin{aligned}
\phi &= -(2B - V_e)\, a \sin\theta - aA\cos 2\theta \\
&\quad -\frac{2}{3}aC\sin 3\theta - \frac{1}{2}aD\cos 4\theta, \\
B &= V_e\left[1 - q^2 S_1(q)\right] - q\frac{da}{dx}S_2(q), \\
A &= q^2\left[\frac{da}{dx}S_3(q) + 2V_e q S_4(q)\right], \\
C &= q^3\left[\frac{da}{dx}S_5(q) + 3V_e q S_6(q)\right], \\
D &= -q^4\left[\frac{da}{dx}S_7(q) + 4V_e q S_8(q)\right], \\
S_1(q) &= 1 - q^2 - q^4 - 2q^6, \\
S_2(q) &= 1 - q^2 - 3q^6, \\
S_3(q) &= 1 - 2q^2 - q^4 - 4q^6, \\
S_4(q) &= 1 - q^2 + q^4, \\
S_5(q) &= 1 - 3q^2 - 3q^4, \\
S_6(q) &= 1 - q^2 - 3q^4,
\end{aligned}
$$

$$
\begin{aligned}
S_7(q) &= 1 - 4q^2 - 6q^4, \\
S_8(q) &= 1 - q^2, \\
q &= \frac{a}{2|H|} \leq \frac{1}{2},
\end{aligned} \tag{L.1}
$$

with V_e given by Eqn. (J.4) as before. Also the non-dimensional scheme of Appendix N is followed.

Then the $\hat{F}$ and $\hat{M}$ expressions are given by Eqn. (I.2) with the concerned parameters, accurate up to $\pm\frac{1}{256}$, are as follows:

$$
\begin{aligned}
g_0 &= -\int_{x_o}^{x_e} a^2 \left(2q^4 + 6q^6 + 1 + 2q^2 + 16q^8\right) dx, \\
g_1 &= \int_{x_o}^{x_e} a^2 x \left(2q^4 + 6q^6 + 1 + 2q^2 + 16q^8\right) dx, \\
g_2 &= \int_{x_o}^{x_e} 4ax^2 \left(6q^2 + 72q^6 + 3 + 15q^8 + 24q^4\right) q^3 \, dx, \\
g_3 &= \int_{x_o}^{x_e} 4a \left(15q^8 + 8q^6 + 1 + 2q^2 + 6q^4\right) q^3 \, dx, \\
g_4 &= \int_{x_o}^{x_e} 4a \left(6q^2 + 72q^6 + 3 + 15q^8 + 24q^4\right) q^3 \, dx, \\
g_5 &= \int_{x_o}^{x_e} \left(-4q^2\right) \left(-2 + 21q^6 + 6q^2\right) a \frac{da}{dx} x + a^2 \left(4q^8 + 2q^4 - 2q^2 + 2q^6 + 1\right) dx + \\
&\quad \left(-2q(x_e)^2 + 4q(x_e)^8 + 2q(x_e)^6 + 1 + 2q(x_e)^4\right) a(x_e)^2 x_e, \\
g_6 &= \int_{x_o}^{x_e} \left(-4q^2\right) \left(-1 + 3q^2\right) a \frac{da}{dx} \, dx \\
&\quad + \left(-2q(x_e)^2 + 4q(x_e)^8 + 2q(x_e)^6 + 1 + 2q(x_e)^4\right) a(x_e)^2, \\
g_7 &= \int_{x_o}^{x_e} 4q^2 \left(-2 + 21q^6 + 6q^2\right) a \frac{da}{dx} \, dx \\
&\quad + \left(2q(x_e)^2 - 2q(x_e)^6 - 2q(x_e)^4 - 1 - 4q(x_e)^8\right) a(x_e)^2, \\
g_8 &= \int_{x_o}^{x_e} 8ax \left(3q^4 - 2 + 4q^2 + 9q^6 - 17q^8\right) q^3 \, dx, \\
g_9 &= -\int_{x_o}^{x_e} 8ax \left(-3 + 6q^4 - 17q^8 + 17q^6 + 6q^2\right) q^3 \, dx, \\
g_{10} &= -\int_{x_o}^{x_e} 8a \left(3q^4 - 2 + 4q^2 + 9q^6 - 17q^8\right) q^3 \, dx, \\
g_{11} &= -\int_{x_o}^{x_e} 2q \left(1 + 2q^4 - 2q^2\right) a \left(\frac{da}{dx}\right)^2 dx - \\
&\quad 2q(x_e) \left(-1 + 3q(x_e)^6 + q(x_e)^2\right) a(x_e)^2 \left.\frac{da}{dx}\right|_{x_e},
\end{aligned}
$$

$$
\begin{aligned}
h_0 &= -\int_{x_o}^{x_e} a^2 x \left(4q^8 + 2q^4 - 2q^2 + 2q^6 + 1\right) dx, \\
h_1 &= \int_{x_o}^{x_e} x^2 a^2 \left(4q^8 + 2q^4 - 2q^2 + 2q^6 + 1\right) dx, \\
h_2 &= \int_{x_o}^{x_e} 4x^3 a \left(-3 + 6q^4 - 17q^8 + 17q^6 + 6q^2\right) q^3 \, dx, \\
h_3 &= \int_{x_o}^{x_e} 4ax \left(2q^2 - 1 - 17q^8 + q^6\right) q^3 \, dx, \\
h_4 &= \int_{x_o}^{x_e} 4ax \left(-3 + 6q^4 - 17q^8 + 17q^6 + 6q^2\right) q^3 \, dx, \\
h_5 &= -\int_{x_o}^{x_e} 4q^2 \left(-2 + 21q^6 + 6q^2\right) a \frac{da}{dx} x^2 \, dx + \\
&\quad \left(-2q\left(x_e\right)^2 + 4q\left(x_e\right)^8 + 2q\left(x_e\right)^6 + 1 + 2q\left(x_e\right)^4\right) a\left(x_e\right)^2 x_e^2, \\
h_6 &= \int_{x_o}^{x_e} \left(-4q^2\right) \left(-1 + 3q^2\right) a \frac{da}{dx} x + \left(-1 + 2q^2 - 2q^4 - 2q^6 - 4q^8\right) a^2 \, dx \\
&\quad + \left(-2q\left(x_e\right)^2 + 2q\left(x_e\right)^4 + 2q\left(x_e\right)^6 + 4q\left(x_e\right)^8 + 1\right) a\left(x_e\right)^2 x_e, \\
h_7 &= \int_{x_o}^{x_e} 4q^2 \left(-2 + 21q^6 + 6q^2\right) a \frac{da}{dx} x + a^2 \left(4q^8 + 2q^4 - 2q^2 + 2q^6 + 1\right) dx - \\
&\quad \left(2q\left(x_e\right)^2 - 2q\left(x_e\right)^6 - 2q\left(x_e\right)^4 - 1 - 4q\left(x_e\right)^8\right) a\left(x_e\right)^2 x_e, \\
h_8 &= \int_{x_o}^{x_e} 8ax^2 \left(3q^4 - 2 + 4q^2 + 9q^6 - 17q^8\right) q^3 \, dx, \\
h_9 &= -\int_{x_o}^{x_e} 8ax^2 \left(-3 + 6q^4 - 17q^8 + 17q^6 + 6q^2\right) q^3 \, dx, \\
h_{10} &= -\int_{x_o}^{x_e} 8ax \left(3q^4 - 2 + 4q^2 + 9q^6 - 17q^8\right) q^3 \, dx, \\
h_{11} &= \int_{x_o}^{x_e} (-2q) \left(1 + 2q^4 - 2q^2\right) a \left(\frac{da}{dx}\right)^2 x + 2q \left(q^2 - 1 + 3q^6\right) a^2 \frac{da}{dx} \, dx, \\
&\quad + 2x_e q\left(x_e\right) \left(-q\left(x_e\right)^2 - 3q\left(x_e\right)^6 + 1\right) a\left(x_e\right)^2 \left.\frac{da}{dx}\right|_{x_e}.
\end{aligned} \tag{L.2}
$$

Appendix M

Model for Store Outside Cavity With Thick Shear Layer

When $\frac{\delta_s}{\delta} > 0.01$ in Eqn. (J.3), we cannot discount the effect of the wavy shear layer structures on the velocity V_e. In this case, again assuming piecewise cosine components for the wavy structures as in Eqn. (4.18), we get the different parameters of $\hat{F}$ and $\hat{M}$ expressions (given in Eqn. (I.2)) as follows:

$$
\begin{aligned}
g_7 &= -\frac{\beta\delta_s}{2\delta}\sum_i W_i\lambda_i^2\left[\cos\left(\lambda_i\left\{X_c^* + \beta Y_c^*\right\} + \zeta_i\right)k_{c,i} + \sin\left(\lambda_i\left\{X_c^* + \beta Y_c^*\right\} + \zeta_i\right)k_{s,i}\right], \\
h_7 &= -\frac{\beta\delta_s}{2\delta}\sum_i W_i\lambda_i^2\left[\cos\left(\lambda_i\left\{X_c^* + \beta Y_c^*\right\} + \zeta_i\right)k_{cx,i} + \sin\left(\lambda_i\left\{X_c^* + \beta Y_c^*\right\} + \zeta_i\right)k_{sx,i}\right], \\
g_{11} &= -\frac{a\left(x_e\right)^2\delta_s}{2\delta}W_j\lambda_j\left\{\sin\left(\lambda_j\left\{X_c^* + \beta Y_c^*\right\} + \zeta_j\right)\cos\left(\lambda_j\mu x_e\right) + \right. \\
&\quad \left.\cos\left(\lambda_j\left\{X_c^* + \beta Y_c^*\right\} + \zeta_j\right)\sin\left(\lambda_j\mu x_e\right)\right\}, \\
h_{11} &= -\frac{x_e a\left(x_e\right)^2\delta_s}{2\delta}W_j\lambda_j\left\{\sin\left(\lambda_j\left\{X_c^* + \beta Y_c^*\right\} + \zeta_j\right)\cos\left(\lambda_j\mu x_e\right) + \right. \\
&\quad \left.\cos\left(\lambda_j\left\{X_c^* + \beta Y_c^*\right\} + \zeta_j\right)\sin\left(\lambda_j\mu x_e\right)\right\}. \qquad \text{(M.1)}
\end{aligned}
$$

The rest of the parameters are zero. It is to be noted that this contribution of the wavy structures is added to Eqn. (J.6) to get the complete expressions for normal force and

moment in the thick shear case. Also, the index j in Eqn. (M.1) corresponds to x_e and

$$\begin{aligned}
k_{c,i} &= \int_x \cos(\lambda_i \mu x)\, a(x)^2\, dx, \\
k_{s,i} &= \int_x \sin(\lambda_i \mu x)\, a(x)^2\, dx, \\
k_{cx,i} &= \int_x \cos(\lambda_i \mu x)\, a(x)^2\, x\, dx, \\
k_{sx,i} &= \int_x \sin(\lambda_i \mu x)\, a(x)^2\, x\, dx, \\
k_{cxx,i} &= \int_x \cos(\lambda_i \mu x)\, a(x)^2\, x^2\, dx, \\
k_{sxx,i} &= \int_x \sin(\lambda_i \mu x)\, a(x)^2\, x^2\, dx.
\end{aligned} \tag{M.2}$$

Here the integrations are carried over that portion of the store which corresponds to the piecewise cosine component represented by the index i of the wavy structure. This is illustrated in Figure M-1.

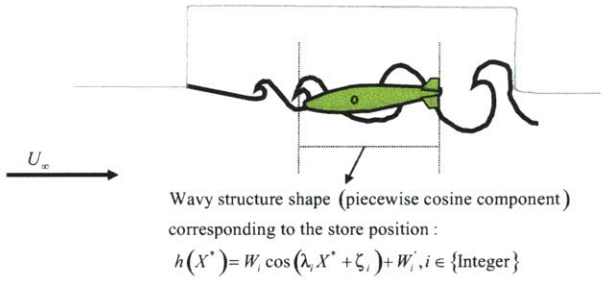

Figure M-1: Piecewise cosine wavy structure for the shear layer. The cosine component chosen here corresponds to the X' coordinate of a point on the store surface, with $X' = X'_c + \mu x$ and the non-dimensionalization scheme is same as Eqn. (4.9).

Appendix N

Non-dimensional Scheme Used in Different Store Drop Models

The complete set of non-dimensional parameters involved in computing $\hat{F}$ and $\hat{M}$ on the store is outlined below:

$$X = \frac{\hat{X}}{\hat{l}_o}, Y = \frac{\hat{Y}}{\delta \hat{l}_o}, Z = \frac{\hat{Z}}{\delta \hat{l}_o}, t = \frac{U_\infty \hat{t}}{\hat{l}_o}, x = \frac{\hat{x}}{\hat{l}_o}, y = \frac{\hat{y}}{\delta \hat{l}_o}, z = \frac{\hat{z}}{\delta \hat{l}_o}, a = \frac{\hat{a}}{\delta \hat{l}_o},$$
$$H_o = \frac{\hat{H}_o}{\delta \hat{l}_o}, D_o = \frac{\hat{D}_o}{\delta \hat{l}_o}, \alpha = \frac{\hat{\alpha}}{\delta}, H = \frac{\hat{H}}{\delta \hat{l}_o} = Y_c - \alpha x, V_c = \frac{\hat{V}_c}{\delta U_\infty}, \omega = \frac{\hat{\omega} \hat{l}_o}{\delta U_\infty}, \tag{N.1}$$

where Y_c, V_c and ω are the vertical coordinate, vertical linear velocity and angular velocity of the store c. g. respectively. The reference frame for integration is attached to the store axis and is illustrated in Figure N-1.

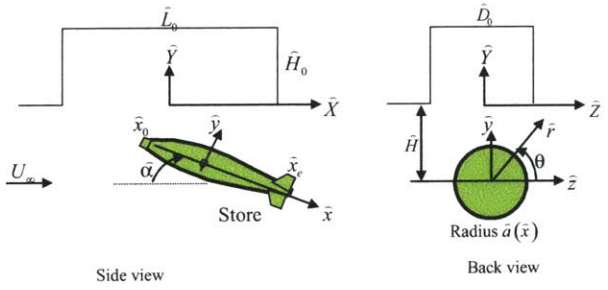

Figure N-1: Reference frames (both fixed to the store and inertial) for computing $\hat{F}$ and $\hat{M}$ on store.

Bibliography

[1] Zhuang, N., Alvi, F. S., Alkislar, M. B., Shih, C., Sahoo, D., and Annaswamy, A. M., "Aeroacoustic Properties of Supersonic Cavity Flows and Their Control," *AIAA 2003-3101*, 2003.

[2] Kibens, V., Alvi, F., Annaswamy, A., Raman, G., and Bower, W. W., "High-Frequency Excitation (HIFEX) Active Flow Control for Supersonic Weapon Release," *presented at 1st AIAA Flow Control Conference*, June, 2002.

[3] Bower, W. W., Kibens, V., Cary, A. W., Alvi, F., Raman, G., Annaswamy, A., and Malmuth, N., "High-Frequency Excitation Active Flow Control for High-Speed Weapon Release (HIFEX)," *AIAA-2004-2513, presented at 2nd AIAA Flow Control Conference*, June 2004.

[4] Alvi, F., Annaswamy, A., Bower, W., Cain, A., Kibens, V., Krothapalli, A., Lourenco, L., and Raman, G., "Active Control of Store Trajectory in a Supersonic Cavity," *Presented by A. Annaswamy, Reactive Gas Dynamics Laboratory Seminar Series, Massachusetts Institute of Technology*, March 2004.

[5] Rockwell, D. and Naudascher, E., "Review – Self sustaining Oscillations of Flow Past Cavities," *ASME J. Fluid Engr.*, Vol. 100, 1978.

[6] Rossiter, J. E., *Wind-Tunnel Experiments on the Flow over Rectangular Cavities at Subsonic and Transonic Speeds*, Aeronautical Research Council Reports and Memoranda No. 3438, Oct 1964.

[7] Heller, H. H., Holmes, G., and Covert, E. E., "Flow Induced Pressure Oscillations in Shallow Cavities," *AFFDL-TR-70-104 (AD-880496)*, Dec 1970.

[8] Tam, C. K. W. and Block, P. J. W., "On the tones and pressure oscillations induced by flow over rectangular cavities," *J. Fluid Mech.*, Vol. 89, No. 2, 1978.

[9] Bilanin, A. J. and Covert, E. E., "Estimation of Possible Excitation Frequencies for Shallow Rectangular Cavities," *AIAA Journal*, Vol. 11, No. 3, 1973.

[10] Gharib, M. and Roshko, A., "The effect of flow oscillations on cavity drag," *J. Fluid Mech.*, Vol. 177, 1987.

[11] Arfken, G., *Mathematical Methods for Physicists, 3rd ed.*, Academic Press, Orlando, Florida, 1985.

[12] Cattafesta, L. N., Garg, S., Choudhari, M., and Li, F., "Active Flow Control of Flow-Induced Cavity Resonance," *AIAA 1997-1804*, 1997.

[13] Sarno, R. L. and Franke, M. E., "Suppression of Flow-Induced Pressure Oscillations in Cavities," *Journal of Aircraft*, Vol. 31, No. 1, 1994.

[14] Stanek, M. J., Raman, G., Kibens, V., Ross, J. A., Odedra, J., and Peto, J. W., "Control of Cavity Resonance Through Very High Frequency Forcing," *AIAA 2000-1905*, 2000.

[15] Cattafesta, L., Williams, D., Rowley, C., and Alvi, F., "Review of Active Control of Flow-Induced Cavity Resonance," *AIAA 2003-3567*, 2003.

[16] Papamoschou, D. and Hubbard, D. G., "Visual Observations of Supersonic Transverse Jets," *Experiments in Fluids*, Vol. 14, No. 6, 1993.

[17] Volkwein, S., ""Proper Orthogonal Decomposition and Singular Value Decomposition"," *Technical Report, SFB-Preprint No. 153*, 1999.

[18] Friedland, B., *Control System Design: An Introduction to State-Space Methods*, McGraw-Hill, Inc., 1986.

[19] Athans, M. and Falb, P. L., *Optimal Control: An Introduction to the Theory and Its Applications*, McGraw-Hill Book Company, 1966.

[20] A. E. Bryson, J. and Ho, Y.-C., *Applied Optimal Control: Optimization, Estimation, and Control*, Blaisdell Publishing Company, 1969.

[21] Slotine, J.-J. E. and Li, W., *Applied Nonlinear Control*, Prentice Hall, 1991.

[22] Bertsekas, D. P., *Dynamic Programming and Optimal Control*, Athena Scientific, 2000.

[23] Newman, A., ""Model reduction via the Karhunen-Loeve Expansion"," *Technical Research Report, T. R. 96-32 and 96-33*, Institute for Systems Research, University of Maryland, Maryland, USA, 1996.

[24] Tang, D., Kholodar, D., Juang, J.-N., and Dowell, E. H., ""System Identification and Proper Orthogonal Decomposition Method Applied to Unsteady Aerodynamics"," *AIAA Journal*, Vol. 39, 2001.

[25] Sahoo, D., Park, S., Wee, D., Annaswamy, A., and Ghoniem, A. F., "A Recursive Proper Orthogonal Decomposition Algorithm for Flow Control Problems," *Technical report 0208, Adaptive Control Laboratory, MIT*, 2002.

[26] Ljung, L., *System Identification Theory for the User*, Prentice Hall PTR, Upper Saddle River, New Jersey, 1999.

[27] Schetz, J. A., "Interaction Shock Shape for Tranverse Injection in Supersonic Flow," *J. of Spacecraft*, Vol. 7, No. 2, 1970.

[28] Sahoo, D., *Control of Acoustics and Store Separation in a Cavity in Supersonic Flow*, Ph.D. thesis, Massachusetts Institute of Technology, Cambridge, Massachusetts, 2005.

[29] Shapiro, A. H., *The Dynamics and Thermodynamics of Compressible Fluid Flow*, Vol. 1, The Ronald Press Company, New York, 1958.

[30] Shalaev, V. I., Fedorov, A. V., and Malmuth, N. D., "Dynamics of Slender Bodies Separating from Rectangular Cavities," *AIAA Journal*, Vol. 40, No. 3, 2002.

[31] Shalaev, V., Malmuth, N., and Fedorov, A., "Analytical Modeling of Transonic Store Separation from a Cavity," *AIAA Paper No. 0004*, 2003.

[32] Sahoo, D., Annaswamy, A. M., Zhuang, N., and Alvi, F. S., "Control of Cavity Tones in Supersonic Flow," *AIAA 2005-0793*, to be presented at the 43rd AIAA Aerospace Meeting and Exihibit, Reno, Nevada, 10-13 January, 2005.

[33] Malmuth, N. and Shalaev, V., "Theoretical Modeling Of Interaction of Mulitple Slender Bodies In Supersonic Flows," *AIAA Paper No. 1127*, 2004.

[34] Davids, S. and Cenko, A., "Grid Based Approach to Store Separation," *AIAA Paper No. 2418*, 2001.

[35] Wei, F.-S. J. and Gjestvang, J. A., "Store Separation Analysis of Penguin Missile From the SH-2G Helicopter," *AIAA Paper No. 0992*, 2001.

[36] Liepmann, H. W. and Roshko, A., *Elements of Gasdynamics*, Dover Publications, Inc., New York, 2001.

[37] Ashley, H. and Landahl, M., *Aerodynamics of Wings and Bodies*, Dover Publications, Inc., New York, 1985.

[38] Milne-Thomson, L. M., *Theoretical Hydrodynamics*, The McMillan Company, New York, fifth edition, 1968.